DISSERTATION

# Investigation of particle mixing in dual fluidized bed gasification systems by means of cold flow modelling and computational methods

ausgeführt zum Zwecke der Erlangung des akademischen Grades eines
Doktors der technischen Wissenschaften
unter der Leitung von

Univ. Prof. Dipl.-Ing. Dr. techn. Hermann Hofbauer
E166 – Institut für Verfahrenstechnik,
Umwelttechnik und Technische Biowissenschaften

eingereicht an der Technischen Universität Wien,
Fakultät für Maschinenwesen und Betriebswissenschaften

von

Stephan Kraft
Matrikelnummer 0525167
Kübeckgasse 12/9
1030 Wien

Wien, 1. Juni 2017          Stephan Kraft

# Danksagung

Da ich selbst die meiste Arbeit für dieses Schriftstück hatte, danke ich mir an erster Stelle für mein Durchhaltevermögen :-).

Weiterhin gebührt großer Dank an Hermann Hofbauer, der mich den weiten Forschungsweg begleitet hat und mir im Bereich der Wirbelschichttechnik ein großer Mentor war.

Meinen Eltern danke ich dafür, dass sie mich immer auf meinem Weg unterstützt haben. Sie sind der Grund, warum ich nun diese Zeilen hier schreiben kann.

Zu guter Letzt danke ich noch meinen lieben Arbeitskollegen (Männer und Frauen). Sie haben immer eine nette und produktive Atmosphäre geschaffen, in der das Forschen stets ein großes Vergnügen war.

<div align="center">

D A N K E

</div>

Wer dem Erfolg auf den Grund geht, findet Beharrlichkeit.

*Sprichwort*

# Abstract

The dual fluidized bed (DFB) steam gasification principle can be used to convert biomass in a valuable product gas. However, in such systems various particle species are present: fresh fuel, converted fuel or bed material particles and additives. These particle species show large differences in size and density and, therefore, potential for segregation processes arise. Segregation can have a negative impact on the operation behavior of DFB reactors and thus, the particle movement has to be known.

Between the two fluidized beds, the gasification and combustion reactor, of a DFB system a bed material recirculation stream is circulating. It determines on the one hand how much converted fuel is transported to the combustion reactor for bed material heat-up. On the other hand it transports this energy back to the gasification reactor.

The first issue is addressed by how much converted fuel is transported to the combustion reactor and how it is mixed in the gasification reactor. The second issue depends on the mixing of the hot stream into the bed of the gasification reactor.

In this work two approaches were used to investigate particle mixing inside of a dual fluidized bed reactor: computational fluid dynamics simulations and cold flow modeling. In the cold flow model the influence of various operation parameters on the char concentration in the recirculating stream between the two fluidized beds of the DFB system was investigated.

Computer simulations were used to investigate the mixing of hot bed material and of the fuel in the bed as well as to investigate the influence of the design of the reactor on mixing. For the simulations the commercial code CPFD Barracuda was chosen. The cold flow model of the commercial plant as well as the commercial plant itself were simulated.

It was shown that the char concentration in the recirculating stream is strongly dependent on various operation parameters like fluidization velocity, recirculation rate, char concentration in the system or bed height. Mixing gets better with increasing fluidization velocity and recirculation rate. However, increasing char concentration in the system and bed height can worsen the mixing behavior.

The choice of the drag law has a massive influence on the predicted bed material

recirculation rate. From the simulations of the Güssing cold flow model and commercial plant no general recommendation can be given which drag law to chose in general. In the present study the EMMS drag model was able to best predict the recirculation rate and pressures inside the system for the commercial plant but also showed some limitations for predicting the behavior of the cold flow model of the commercial plant.

A simulation model was built which was able to predict the bed material recirculation rate, pressures, temperatures and gas compositions inside the hot system with good accuracy. The simulations showed that the hot bed material coming from the combustion reactor is not ideally mixed. Furthermore, for a plant of the size of Güssing one fuel feed point is enough according to the simulations.

Plants larger than the size of Güssing the design could benefit from optimization. It was shown with cold flow model experiments that poorly fluidized zones could occur in large DFB plants and that implementing an additional fluidization for these zones could significantly enhance particle mixing.

The experimental and simulation results were able to broaden the knowledge about the mixing and segregation processes inside DFB systems. Furthermore, the results indicate that for larger DFB plants further scale effects concerning mixing could occur due to the larger dimensions. Therefore, adaptations regarding the design or the number of fuel feeding points could be necessary.

# Contents

# 1 Introduction

## 1.1 Motivation and research questions

Fluidized bed reactors have been used in industry applications for many decades. One main field of application is the use of fluidized beds in thermal processes like gasification and combustion. Coal gasification with $O_2$ is carried out since the early 20th century. More recently also gasification of biomass with $O_2$ and/or steam has become more attention. Fluidized bed combustors are built for the combustion of coal, waste or biomass for generation of steam to provide heat or electricity.

Drying of wet solids can be carried out in fluidized beds since the entire surface of the drying material is suspended and exposed to the gas stream passing through the bed. In the pharmaceutical industry fluidized beds are also used for coating or granulation processes.

Fluidized beds can also be applied for the adsorption of various materials. One possible field of application is the separation of $CO_2$ from a flue gas stream. Fluid catalytic cracking processes to crack large and heavy hydrocarbons are applied in presence of a fluidized catalyst. Furthermore, fluidized beds can be used for coal beneficiation.

Fluidized beds show several advantages for these processes. The fluid passing upwards through the bed a fluid-like behavior similar to a boiling liquid occurs. Thus, an excellent mixing and gas/solid contact is obtained. However, this only holds for beds which consist only of one particle species. If particle species which differ in size and/or density are present, segregation processes can occur.

Recently, biomass gasification got greater attention since it is the only renewable source which contains carbon. For chemicals or fuels, carbon is essential. One promising implementation for biomass gasification is the dual fluidized bed (DFB) steam gasification system. The development from the process at TU Wien went from laboratory and pilot scale finally to industrial scale. The first demonstration plant of industrial scale was the power plant in Güssing, Austria. Up to now, additional DFB plants have been built (Oberwart and Villach in Austria, Senden in Germany or Gothenburg in Sweden).

In a DFB system two fluidized beds are connected with a bed material circulating in between. A gasification reactor which is operated in a bubbling bed mode and fluidized with steam is connected to a combustion reactor where the solid residue after devolatilization ("wood char") is burnt. More information on the process can be found in section 2.2.1.
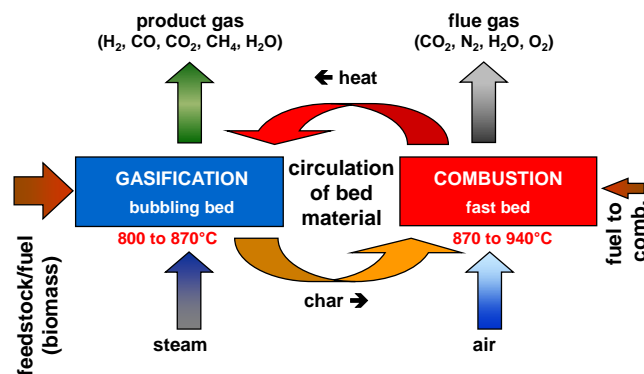


**Figure 1.1:** *Schematic principle of the dual fluidized bed (DFB) process for biomass steam gasification (based on Schmid et al. [1]).*

By using biomass in a DFB steam gasification system a valuable product gas is obtained which consists of CO, $CO_2$, $H_2$, $CH_4$, and steam [2]. A characteristic of the process is the separation of the processes for generating the product gas and the heat necessary for drying and devolatilization of the fuel. Therefore, no $O_2$ is used for the gasification process and a product gas free of $N_2$ is obtained. One possible usage of the gas is its conversion into electricity via a gas engine [3, 4, 5, 6, 7]. More promising is the usage of the product gas for various gas conditioning and synthesis applications like bio-hydrogen generation [8, 9], the production of synthetic natural gas [10] or synthetic fuels like alcohols [11] or Fischer–Tropsch diesel [12]. Compared to the heat and electricity generation these fuels can be either stored and transported more easily or can be used in chemical industry for synthesis processes e.g. of base chemicals.

To further investigate, optimize and scale-up the process information is necessary about the particle movement and mixing processes inside such reactors. Looking at the particle level one finds that various particle species are present in a DFB system: bed material, fresh biomass, partly converted biomass, fully converted biomass and additives. The fully converted biomass is also referred to as "wood char" or simply "char", which is used in this work.

The particle diameters and densities vary over a large range. In Table 1.1 possible ranges of bed material, biomass and char are shown. It can be seen that the sizes differ

up to two magnitudes in size and density. The bed material particles are small and heavy compared to the biomass and char particles which are large and light.

**Table 1.1:** *Typical diameters and densities of particle species present in a DFB system.*

|  | bed material | fresh biomass | wood char |
|---|---|---|---|
| $d_p$ [m] | $(1\text{–}5)\times10^{-4}$ | $(0.1\text{–}5)\times10^{-2}$ | $(0.1\text{–}5)\times10^{-2}$ |
| $\rho_p$ [kg/m$^3$] | 2800 | 600–800 | 150–300 |

Fluidized beds consisting of particles of different size and density are likely to show segregation behavior [13]. Many negative consequences can arise like higher loads of tars or poor distribution of fuel particles across the bed cross section area. More tar is generated if the fuel is not well mixed and has sufficient contact with the hot bed material. The advantage of good particle contact and even temperature distribution within the bed are not guaranteed any more.

Therefore, the larger and lighter particles tend to move upwards in the bed and float on the bed surface which is also called a flotsam behavior according to the definition by Rowe et al. [13]. The small and heavy particles on the other hand show the opposite behavior: They tend to accumulate at the bottom of the bed and are only transported upwards in the wakes of the rising bubbles. This behavior is called jetsam. In the case of a bed in the DFB system the biomass and wood char show flotsam behavior whereas the bed material behaves jetsam.

During operation of a DFB system a sufficient large amount of wood char has to move to the combustion reactor that enough heat can be generated to heat up the bed material by oxidizing the char. The bed material stream (including char) leaves the gasification reactor at the bottom and the char tends to move upwards in the bed. Therefore, the segregation of char has an influence on the operation of the system. Especially, the dependence of char mixing on operating parameters like the fluidization velocity, char concentration and bed height, is of interest for process optimization.

Up to now it is not known which char concentration in the bed material recirculation stream occurs. Its measurement is troublesome due to high temperatures and rough conditions due to bed material movement and high recirculation rates. Furthermore, the char hold-up in the gasification reactor is not known. Some authors give estimates like Singh et al. [14] or Werther and Ogada [15] who consider the mass fraction of char for a hot fluidized bed combustor to be around 1–5 wt.-%. Due to the lower char reactivity in a steam environment as it is inside a DFB gasification reactor, higher hold-ups are likely to occur [16].

Via energy balances it is possible to calculate the amount of char which is burnt in the combustion reactor, as e.g. carried out by Wilk and Hofbauer [17]. Doing so, it cannot be determined if the whole amount of char is burnt in the combustion reactor or if a certain amount leaves the combustion reactor unburnt and moves to the cyclone and loop seal. The latter case or a transportation of char also to the loop seal is likely since temperatures in the cyclone and loop seal are higher than at the top of the riser which leads to the conclusion that combustion processes are still ongoing.

Not only is the mixing of the biomass and bed material particles are of interest but also the mixing of the hot bed material inside of the gasification reactor. Since the hot bed material provides the energy necessary for drying and devolatilization reactions of the fuel particles it has to be mixed well in the gasification reactor to distribute the energy evenly. If this is not the case local zones with higher and lower temperature occur. Negative consequences could be a higher tar load in the product gas which could cause problems in downstream processes.

Therefore, the following research questions arise and are treated within this work:

**Q1**  How do the char particles mix in the system and how is this mixing behavior dependent on various operating parameters?

**Q2**  How does the hot bed material in the gasification reactor mix?

**Q3**  Is there a need for more feed points for the biomass in the commercial plant?

**Q4**  Is there any potential for poorly fluidized zones in the hot reactor?

**Q5**  In the view of scale-up, is the conical shape of the gasification reactor optimal also for larger DFB systems?

## 1.2 Approach in this work

The investigation of the hydrodynamics and particle mixing is difficult inside DFB reactors due to high temperatures and rough movements of the bed material. Two approaches exist to gain information about the ongoing processes on particle level in a DFB reactor:

- cold flow modeling,

- computational fluid dynamics.

Cold flow modeling is used to establish a physical model which is smaller and can be operated at ambient conditions. Therefore, no heat-up is necessary which makes

operation more flexible and increases the number of experiments which can be carried out in the same time. Furthermore, the fluidization behavior can be investigated visually, experiments are easy to conduct and alterations of the design can be easily made.

However, in cold flow models no heat transfer and thermal particle conversion processes can be considered. In the case of biomass combustion or gasification the release of the volatiles can influence bed hydrodynamics and particle movement [18, 19]. This issue can be overcome by additionally introducing air which simulates the fuel drying and devolatilization as e.g. done by Bosch [20] in a cold flow model of the Güssing DFB system.

To ensure hydrodynamic similarity between commercial plant and the cold flow model scaling criteria are applied. They keep constant various dimensionless numbers. However, they have to be considered as sufficiently suitable to show the claimed similar behavior. At TU Wien cold flow modeling of the DFB system has been carried out by various authors [21, 1], a recent review gave an overview about many conducted experiments [22].

Computational fluid dynamics simulations of gas/solid flows have been made great progress in the last decades. The accuracy of the predictions has increased by implementing more effects occurring between particles or between particles and the gas phase. Existing models were extended. However, due to the complex momentum transfer between gas and particles as well as the particles itself such methods are still under development [14]. The computational cost is still high for some methods which consider interactions on particle level. A trade-off between accuracy and calculation time has to be found in many cases.

The high particle numbers of the order of $10^{10}$ in real DFB systems are challenging for computational codes since the amount of particles determines the calculation time. A promising implementation is the so-called MP-PIC or multi-phase particle-in-cell code. In the present work the commercial code CPFD (computational particle fluid dynamics) Barracuda is used in which the MP-PIC approach is implemented.

In the Barracuda framework the particles are grouped into computational particles which have the same properties. As a result, the particle count can be reduced to a magnitude of $10^5$ to $10^6$ which results in a significantly lower computational cost.

The great advantage of this code is, that the real DFB system can be implemented with all boundary conditions that also occur in reality. Therefore, one has not to rely on simulations of segments of the reactor and all occurring processes in the reactor can be simulated and considered. Furthermore, also the particle conversion processes and

volatile release can be implemented and their influence on the bubbling behavior can be considered. However, the chemical kinetics which are necessary for the conversion processes rely on empirical measurements and often show large deviations which can be in the order of magnitudes [16]. Also the gas/particle momentum transfer is influenced by many parameters, especially by the drag law which has a large influence to the momentum exchange term [23].

For the investigation of DFB system a combination of both approaches, cold flow modeling and CPFD simulations, is the most useful since the advantages of both approaches can be used and each tool can be used for the applications for which it is best suited. This is also indicated in Figure 1.2. So evidence gained from one of the two tools can be used in the other as either validation or starting point for further investigations.
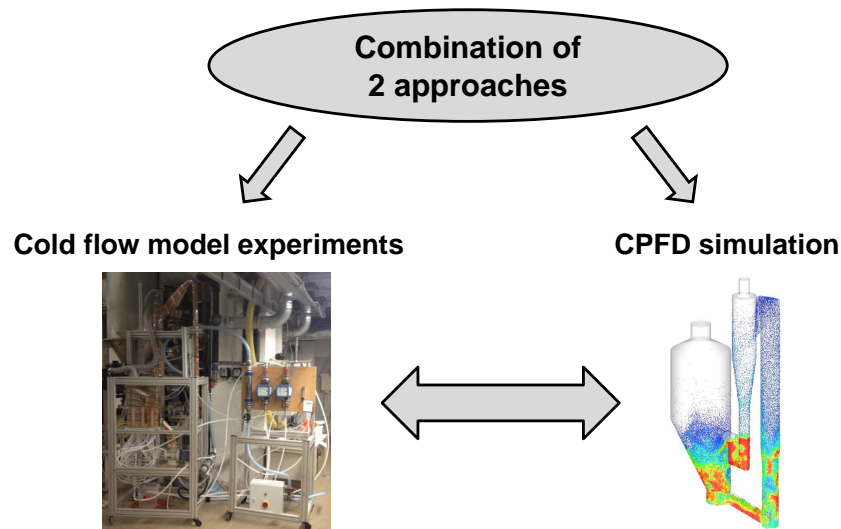


**Figure 1.2:** *Approach used in this work as a combination of cold flow modeling and computational fluid dynamics simulations.*

Since mixing processes of binary beds inside of DFB systems are difficult to simulate due to the complexity of the mixing and particle interaction phenomena this question is best answered with cold flow model experiments. Therefore, a cold flow model which has a similar design as the Güssing plant has been set up to investigate the mixing behavior of char inside the DFB system. Because of the recirculating bed material stream in the commercial DFB system also the cold flow model should be constructed with bed material recirculation. To deal with research question **Q1** the following specifications were used for the cold flow model:

- Fluidization reactor with a bubbling fluidized bed where the same fluidization

conditions in the gasification reactor in Güssing can be simulated and where the same particle mixing processes can be established.

- Possibility of controlling the bed material recirculation stream independently of the fluidization rate of the combustion reactor.

- Possibility of sampling during operation of the cold flow model for investigation of the char concentration in the bed material recirculation stream. Therefore, shutdowns are avoided and a large number of experiments can be conducted to get meaningful mean values.

The research questions **Q2** to **Q4** are best answered with CFD simulations. For that purpose first a complete validated model of the hot plant has to be set up with the following specifications:

- exact geometry based on plans of the real hot reactor

- all relevant particle species inside the system including their PSDs have to be considered

- the most relevant chemistry processes have to be considered as drying and de-volatilization of the wood, combustion of the char and further homogeneous gas phase reactions

- all inlet flows of the commercial plant have to be considered

- heat transfer processes (heat loss, heat transfer between gas and particle as well as particles itself) have to be accounted for.

For the Güssing plant a cold flow model was available. Therefore, first the cold flow model is investigated with the Barracuda code to test its usability. The influence of the drag law on the simulation results and especially its impact on the bed material recirculation rate was investigated since this is a very important quantity for the commercial plant.

In a following step a model of the commercial plant was set up and validated with operational data like pressures, temperatures, bed material recirculation rate and gas compositions of the product and flue gas. With this model simulations can be conducted to answer the research questions **Q2** to **Q4**.

Research question **Q5** was investigated with both the Barracuda model and the cold flow model. The main interest was the investigation of occurring poorly fluidized zones above the conical region in the gasification reactor.

First the Barracuda model was used to investigated if such zones could occur in the commercial plan in Güssing. In a second step the cold flow model was altered to investigated possible influences in larger DFB plants like the HGA Senden which is of the double size as Güssing. A slope was implemented in the cold flow model to account for the conical design of the gasification reactor. Furthermore, the slope was equipped with nozzles to be able to study the influence of the fluidization of the slope on the overall mixing processes.

## 1.3 Papers arising from this work

The present work is based on the following research papers which have already been submitted for publication or published. Parts of these publications have been used in this work as shown in Table 1.2.

In all the following publications the author is responsible for experimental, simulation and research work, data evaluation and writing.

**Table 1.2:** *Contribution of the papers to the Chapters in this work.*

| Paper | Contribution to Chapter |
|-------|------------------------|
| I     | 3                      |
| II    | 4                      |
| III   | 4, 6                   |
| IV    | 5                      |

**Paper I**

S. Kraft and H. Hofbauer. Fluidization of binary mixtures of dissimilar solids: A review. *Powder Technology*, submitted, 2017

**Paper II**

S. Kraft, F. Kirnbauer, and H. Hofbauer. Influence of drag laws on pressure and bed material recirculation rate in a cold flow model of an 8 MW dual fluidized bed system by means of CPFD. *Particuology*, accepted for publication, 2017

**Paper III**

S. Kraft, F. Kirnbauer, and H. Hofbauer. CPFD simulations of an industrial-sized dual fluidized bed steam gasification system of biomass with 8 MW fuel input. *Applied Energy*, 190:408–420, 2017

**Paper IV**

S. Kraft, F. Kirnbauer, and H. Hofbauer. Investigations using a cold flow model of char mixing in the gasification reactor of a dual fluidized bed gasification plant. *Powder Technology*, in press, 2016

# 2 Fundamentals of fluidization

In this chapter fundamentals necessary for this work are described. This includes aspects about hydrodynamics of fluidized beds for one particle species. Binary beds of dissimilar solids are dealt with in Chapter 3 in greater detail.

Since this work deals with the DFB process in Güssing, basic concepts of the process are described. Furthermore, relevant aspects for modeling of the DFB system like thermal conversion of biomass and occurring homogeneous and heterogeneous gas-phase reactions are described. Also the modeling of these processes is described in the way necessary for the presented simulations in Chapter 4.

Cold flow modeling is based on dimensional analysis. A short introduction into this field is also given, especially with a focus on the used concepts of Glicksman's full and simplified set and regime diagrams for fluidized beds since these concepts are also often used in this work.

This chapter ends with a short introduction into computational models for the simulation of gas/solid flows. The basic equations of the implementation of the MP-PIC code in Barracuda is given.

## 2.1 Fundamentals of fluidized beds

### 2.1.1 Characterization of particles

The characterization of particles is fundamental for the further calculations. Particles in a system can be characterized by

- density (mass per volume of particle), $\rho_p$,

- diameter (size of particle), $d_p$,

- sphericity (shape of particle), $\phi_p$,

- particle size distribution (PSD), since in reality particles are generally not of one distinct size.

For the gas flow through a fixed or a fluidized bed the pressure drop is an interesting quantity. Therefore, for calculations a particle diameter is needed which gives, once inserted into the equations for the pressure drop, the same pressure drop as the bed of the non-spherical particles. Doing so, a bed of irregular shaped should be modeled with a bed of spheres. If the *Sauter diameter*, $d_{sv}$, is used this can be obtained. It is defined as:

$$d_{sv} = \frac{\text{surface of the particle}}{\text{volume of the particle}} = \frac{S_p}{V_p} = \frac{d_{sv}^2 \pi}{\frac{d_{sv}^3 \pi}{6}} \rightarrow d_{sv} = \frac{6V_p}{S_p} \; . \tag{2.1}$$

The sphericity, $\phi_p$, is a measure for the deviation from the ideal spherical shape. It is defined as:

$$\phi_p = \frac{\text{surface of a sphere with same volume}}{\text{surface of the particle}} \; . \tag{2.2}$$

For spheres it is $\phi_p = 1$ and for irregular shaped particles it is $0 < \phi_p < 1$. Values of sphericities of various materials can be found in [28].

Since in reality the particles are never of the same size they occur always with a particle size distribution (PSD). PSDs can be obtained e.g. by sieve analysis or laser diffraction analysis. For a bed with a particle size distribution also a mean diameter for calculations is needed. To calculate the Sauter mean diameter the following equation can be used [29]

$$d_{sv} = \left[ \sum_i^n \left( \frac{V_{p,i}}{V} \frac{1}{d_{p,i}} \right) \right]^{-1} , \tag{2.3}$$

for $n$ intervals of particles sizes. $V_{p,i}$ is the volume and $d_{p,i}$ is the diameter of the $i$-th particle size interval.

If particles are combined to an aggregate the following characterizations are introduced:

- porosity or volume fraction of the gas and particle phase, $\varepsilon_g$ and $\varepsilon_p$

- bulk density of the bed, $\rho_{p,bulk}$

The porosity or gas phase volume fraction is defined as

$$\varepsilon_g = \frac{V_g}{V_g + V_p} \; . \tag{2.4}$$

where $V_g$ and $V_p$ mean the volume of the gas and the particles in the bed, respectively. The particle volume fraction can be calculated in a similar way as in Eq. (2.4) by

$$\varepsilon_p = \frac{V_p}{V_g + V_p} = 1 - \varepsilon_g \; . \tag{2.5}$$

With the density of the particles, $\rho_p$ and the bulk density $\rho_{p,bulk}$ the gas volume fraction can also be calculated:

$$\varepsilon_g = 1 - \frac{\rho_{p,bulk}}{\rho_p} \; . \tag{2.6}$$

## 2.1.2 Fluid mechanic behavior of fluidized beds

### States of fluidization

If a gas stream flows through a bed of particles various states of fluidization occur. The particles show then the fluid-like character which led to the naming. In Figure 2.1, (a), the fixed bed state is depicted. The fluid passes through the voids of the bed and therefore a pressure drop occurs in the gas flow.

If the superficial velocity through a fixed bed is increased over a certain point the bed behavior changes from a fixed to a *fluidized* bed – the particles leave their initial positions and start to move, Figure 2.1, (b), $\varepsilon_g = \varepsilon_{mf}$. This point is also called the *minimum fluidization condition*.

Increasing the superficial velocity over the minimum fluidization condition the bubbling fluidization state follows (except for particles of Geldart's group A [30]) – the bed expands further and the bed height increases, Figure 2.1 (c), $\varepsilon_g > \varepsilon_{mf}$. In contrast to the fixed bed for fluidized beds the bed porosity, $\varepsilon_g$, and the superficial velocity, $u_0$, are not independent from each other.

A further increase of the superficial velocity leads then to *turbulent* fluidization where particles are entrained from the system, Figure 2.1 (d). Finally, if the velocity is increased over the terminal velocity of the particles the *pneumatic conveying* occurs, Figure 2.1 (e). For that case $\varepsilon_g \rightarrow 1$ when a single particle is in a large gas volume.

The fluidization states can also be expressed by the profile of the particle volume fraction, $\varepsilon_p$, along the reactor height, Figure 2.2. In the case of a bubbling bed $\varepsilon_p$ is nearly constant over the bed height and then decreases sharply in the splash zone of the fluidized bed to about $\varepsilon_p = 0$ in the freeboard.

In the turbulent fluidized bed regime the bed expands more than the bubbling bed and more gas volume is present. Therefore, $\varepsilon_p$ is lower in the bottom of the reactor than for a bubbling bed but a distinct splash zone occurs over the bed and large bubbles
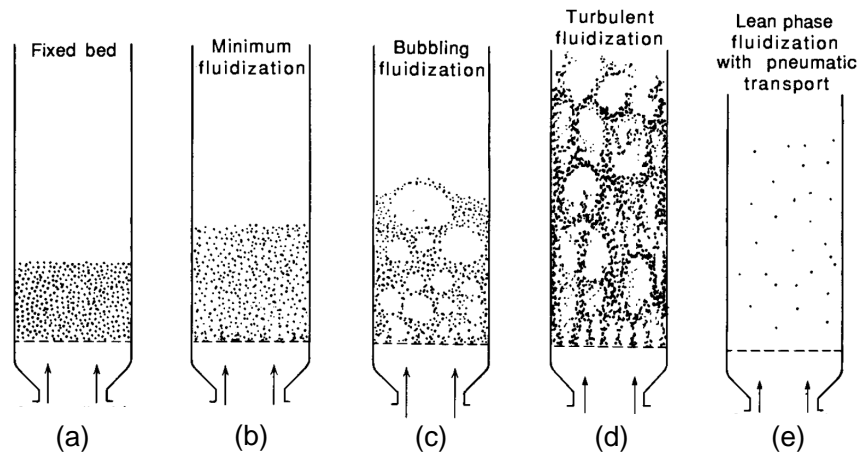
**Figure 2.1:** *Different states of fluidization (according to Kunii and Levenspiel [28]).*

form. The particles are shifted to greater heights by the bubbles.

High particle entrainment occurs for the fast fluidized bed where the particle volume fractions gets more constant over the reactor height. If the superficial velocity is even more increased and all particles are entrained and no denser regions occur any more the state of pneumatic conveying is reached.

**Pressure drop over a fixed bed**

If a fluid passes through a fixed bed a pressure drop occurs. For its calculation the well-known Ergun equation [31] is often used. The Ergun equation is based on the assumption that a fixed bed can be replaced by ducts (with changing directions and cross sections) and that the pressure drop calculation can so be reduced to the calculation of the pressure drop in a tube flow. Ergun got the following equation [31]:

$$\frac{\Delta p_{bed}}{\Delta h_{bed}} = 150 \frac{(1 - \varepsilon_g)^2}{\varepsilon_g^3} \frac{\mu_g u_0}{d_{sv}^2} + 1.75 \frac{1 - \varepsilon_g}{\varepsilon_g^3} \frac{\rho_g u_0^2}{d_{sv}} \ . \tag{2.7}$$

For fixed beds the bed porosity, $\varepsilon_g$ and the superficial velocity $u_0$ are independent from each other.

**Pressure drop over a fluidized bed**

The distinction between the three states fixed and fluidized bed as well as pneumatic conveying can also be done by means of the pressure drop over the bed, Figure 2.3. For the fixed bed the pressure drop over the bed increases until the minimum fluidization, $u_{mf}$. From there on an increase of the superficial velocity does not lead to an increase
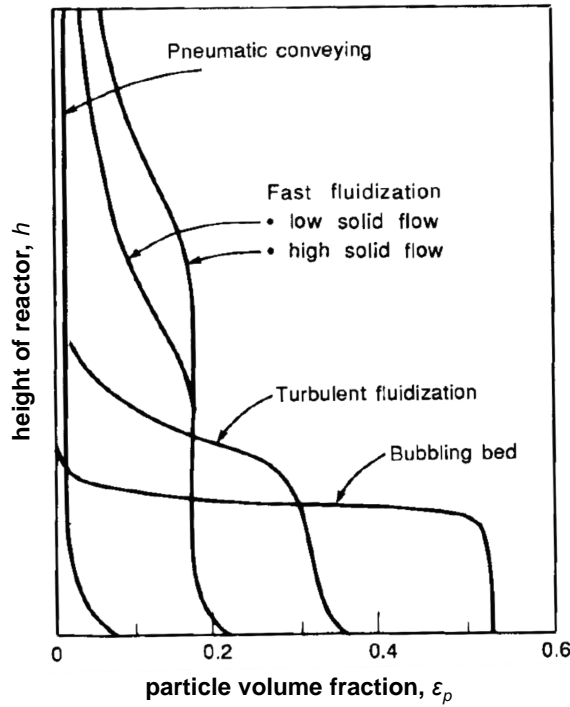
**Figure 2.2:** *Particle volume fraction over the height of fluidized beds (according to Kunii and Levenspiel [28]).*

in pressure drop any more. The pressure drop remains constant over the whole fluidized bed state. If the superficial velocity exceeds slightly the terminal velocity, $u_t$ the pressure drop increases again and pneumatic transport occurs. Equations for the calculation of $u_{mf}$ and $u_t$ are derived in section 2.1.3.

The calculation of the pressure drop over a fluidized bed is done in the following way with a balance of forces. The pressure drop of the fluid over a certain length $\Delta h_{bed}$ has to be in the balance with the weight of the solids and the weight of the fluid.:

$$\Delta p_{bed} A_{bed} = |\mathbf{F}_{g,p}| + |\mathbf{F}_{g,g}| , \tag{2.8}$$

with

$$|\mathbf{F}_{g,p}| = \rho_p (1 - \varepsilon_g) g A_{bed} \Delta h_{bed} , \tag{2.9}$$

$$|\mathbf{F}_{g,g}| = \rho_g \varepsilon_g g A_{bed} \Delta h_{bed} \tag{2.10}$$

Combining equations (2.8) to (2.10) gives:
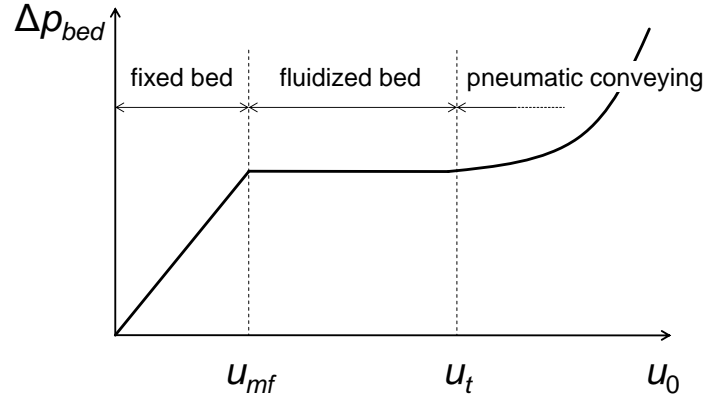
**Figure 2.3:** *Pressure profile for the different fluidization regimes.*

$$\Delta p_{bed} = (\rho_p - \rho_g)(1 - \varepsilon_g)g\Delta h_{bed} + \rho_g g\Delta h_{bed} \; . \tag{2.11}$$

The first term on the right side of Equation (2.11) is the pressure of the gas due to surface friction through the lifting of the particles. The second term is the pressure drop that is caused through the lifting of the fluid against gravity. No pressure drop is caused because the potential energy of the fluid is then higher and could be reversibly recovered. For further considerations in this work only the first term is relevant and therefore used.

**Drag force**

Any solid particle which moves through a fluid experiences a force opposite to the direction of movement. This force, called *drag force*, is due to the shear forces which act on the surface of the particle. The drag force is the dominating force acting on the particles.

The drag force, $\mathbf{F}_d$, can be expressed as

$$\mathbf{F}_d = \frac{\rho_g}{2}C_d(\mathbf{u}_g - \mathbf{u}_p)|\mathbf{u}_g - \mathbf{u}_p|A_p \; , \tag{2.12}$$

where $C_d$ is the drag coefficient which is a function of the particle Reynolds number, $Re_p$, $C_d = C_d(Re_p)$. $C_d$ can be experimentally determined. $A_p$ is the cross sectional area of the particle normal to the flow direction. Table 2.1 shows correlations depending on $Re_p$ to calculate the drag coefficient $C_d$. $Re_{p,crit}$ is the critical Reynolds number and is about $Re_{p,crit} \approx 2.5 \cdot 10^5$ [29].

**Table 2.1:** *Correlation to calculate $C_d = C_d(Re_p)$ [29]*

| | |
|---|---|
| $Re_p < 0.5$ | $C_d = \frac{24}{Re_p}$ |
| $0.5 < Re_p < 1000$ | $C_d = \frac{24}{Re_p}\left(1 + 0.15Re_p^{0.687}\right)$ |
| $1000 < Re_p < Re_{p,crit}$ | $C_d \approx 0.44$ |

### 2.1.3 Calculation of characteristic velocities of fluidized beds

**Minimum fluidization velocity**

With the given equations in the previous sections the minimum fluidization velocity $u_{mf}$ can be calculated. For the derivation the fact is used that at the point of $u_{mf}$ in Figure 2.3 the pressure drop over the fixed bed, Eq. (2.7), equals the pressure drop over the fluidized bed, Eq. (2.11). So, these two equations can be combined and the following equation is obtained:

$$\frac{\rho_g d_{sv}^3 (\rho_p - \rho_g)g}{\mu_g^2} = \frac{150(1 - \varepsilon_{mf})}{\varepsilon_{mf}^3}\frac{\rho_g d_{sv} u_{mf}}{\mu_g} + \frac{1.75}{\varepsilon_{mf}^3}\frac{\rho_g^2 d_{sv}^2 u_{mf}^2}{\mu_g^2} \ . \tag{2.13}$$

Observing Eq. (2.13) shows that all the terms are dimensionless. The left side of the equation is called the Archimedes number:

$$Ar = \frac{\rho_g d_{sv}^3 (\rho_p - \rho_g)g}{\mu_g^2} \ . \tag{2.14}$$

In both terms on the right side the particle Reynolds number, formed with $u_{mf}$, occurs:

$$Re_{p,mf} = \frac{\rho_g d_{sv} u_{mf}}{\mu_g} \ . \tag{2.15}$$

Since the particle Reynolds number is formed with the minimum fluidization velocity this is indicated by the subscript $mf$.

With $Ar$ and $Re_p$ Eq. (2.13) can also be written in the following form:

$$Ar = C_1 Re_{p,mf} + C_2 Re_{p,mf}^2 \ . \tag{2.16}$$

For the coefficients $C_1$ and $C_2$ several authors published coefficients, e.g. Wen and Yu [32] or Grace [33].

As shown in Eq. (2.16) $u_{mf}$ can be calculated then from the quadratic equation from

$Re_{p,mf}$. Therefore, if the equation is rearranged, the following relationship exists

$$\frac{u_{mf} d_p \rho_g}{\mu_g} = Re_{p,mf} = Re_{p,mf}(Ar) \,. \tag{2.17}$$

**Terminal velocity**

If the superficial velocity is increased a point is reached where the particles are carried out of the bed. This is the case when the forces that the fluid exerts on the particles (drag and buoyancy) equal the gravity force. Figure 2.4 shows the forces acting on a particle which is on steady flow. $\mathbf{F}_g$ means the gravitational force, $\mathbf{F}_b$ is the force due to buoyancy and $\mathbf{F}_d$ is the drag force. For steady flow a force balance with the three forces can be written:

$$\mathbf{F}_g = \mathbf{F}_b + \mathbf{F}_d \,. \tag{2.18}$$

Expressing all the forces leads to

$$(\rho_p - \rho_g)\frac{\pi}{6} d_{sv}^3 g = \frac{\rho_g}{2} u_t^2 \frac{\pi}{4} d_{sv}^2 C_d(Re_p) \,. \tag{2.19}$$

Rearranging gives the terminal velocity, $u_t$

$$u_t = \sqrt{\frac{4}{3} \frac{\rho_p - \rho_g}{\rho_g} \frac{g d_{sv}}{C_d(Re_p)}} \,, \tag{2.20}$$

where $C_d$ is the drag coefficient.
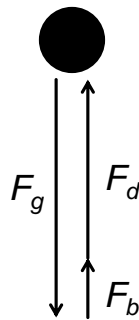


**Figure 2.4:** *Forces acting on a spherical particle moving through a fluid.*

## 2.1.4 Heat transfer in fluidized beds

Regarding the heat transfer three mechanisms can be distinguished:

- heat transfer between gas and particles,

- heat transfer between particles and wall or heat exchanger surfaces,

- heat transfer between gas and wall or heat exchanger surfaces.

The heat transfer coefficient $\alpha$ is in general defined as

$$\alpha = \frac{\dot{q}}{\Delta T} \, , \tag{2.21}$$

where $\dot{q}$ means the heat flux density and $\Delta T$ a characteristic temperature difference. The dimensionless form of the heat transfer coefficient is the particle Nußelt number:

$$Nu_p = \frac{\alpha d_p}{\lambda_g} \, , \tag{2.22}$$

where $d_p$ means the particle diameter for the problem and $\lambda_g$ means the heat conductivity of the gas phase. For heat transfer problems also the Prandtl number, $Pr$, is relevant – it is the ratio of the transport of momentum due to friction and heat transfer due to conduction:

$$Pr = \frac{\mu_g c_{p,g}}{\lambda_g} \, . \tag{2.23}$$

Generally, heat transfer correlations are of the form $Nu = Nu(Re_p, Pr)$.

**Heat transfer between gas and particles**

In a fluidized bed the heat transfer coefficient between the gas and particles has to be between the fixed bed and the single sphere, since $\varepsilon_{g,\text{fixed bed}} < \varepsilon_{g,\text{fluidized bed}} < 1$. Starting in a fixed bed and the Reynolds number, $Re_p$, is increased also the heat transfer coefficient increases. This corresponds to the left curve in Figure 2.5 which depicts the Nußelt correlation for a fixed bed. If the superficial velocity or $Re_p$ is increased, $Nu_p$ can increase on that left curve until the minimum fluidization point, marked as point a in Figure 2.5. There is the onset of a fluidized bed. If $u_0$ or $Re_p$ is further increased the heat transfer coefficient remains nearly constant with a slight maximum between points a and b [34]. Point b means the terminal velocity where the pneumatic conveying starts and particles are assumed in a very large volume which corresponds to the flow around a single particle ($\varepsilon_g \rightarrow 1$). Because of that in ref. [29] it is recommended to use the following approximation:

$$Nu_{\text{fluidized bed}} \approx Nu_{\text{single sphere}}(Re_{p,mf}, Pr) . \tag{2.24}$$

For the calculation of the heat transfer coefficient of the single sphere there are many correlations available in [29].
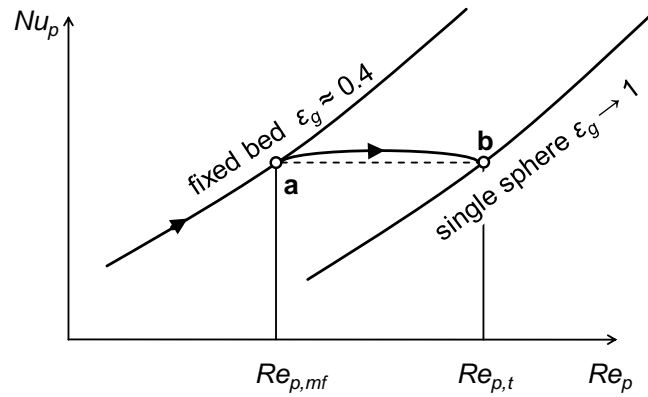


**Figure 2.5:** *Nußelt number dependent on Reynolds number for fixed bed and for a single sphere. The Nußelt number in a fluidized bed lies between that range (according to Baehr and Stephan [34])*

For low Nußelt numbers the equations of Kothary fits best the experimental results [28]

$$Nu_p = 0.033 Re_p^{1.3} \qquad 0.1 < Re_p < 100 . \tag{2.25}$$

For single spheres the equation by Ranz and Marshall [35, 36] can be used

$$Nu_p = 2 + 0.6 Re_p^{1/2} Pr^{1/3} . \tag{2.26}$$

The default correlation in Barracuda is taken from McAdams [37] which is for single spheres:

$$Nu_p = 0.37 Re_p^{0.6} \qquad 17 < Re_p < 70,000 . \tag{2.27}$$

Chen [38] also gives a correlation

$$Nu_p = 0.0282 Re_p^{1.4} Pr^{0.33} \qquad 0.1 < Re_p < 50 . \tag{2.28}$$

Figure 2.6 shows these correlations with the validity ranges stated above drawn for $Pr = 0.7$.

For simulations of the Güssing power plant the Nußelt number determines how much
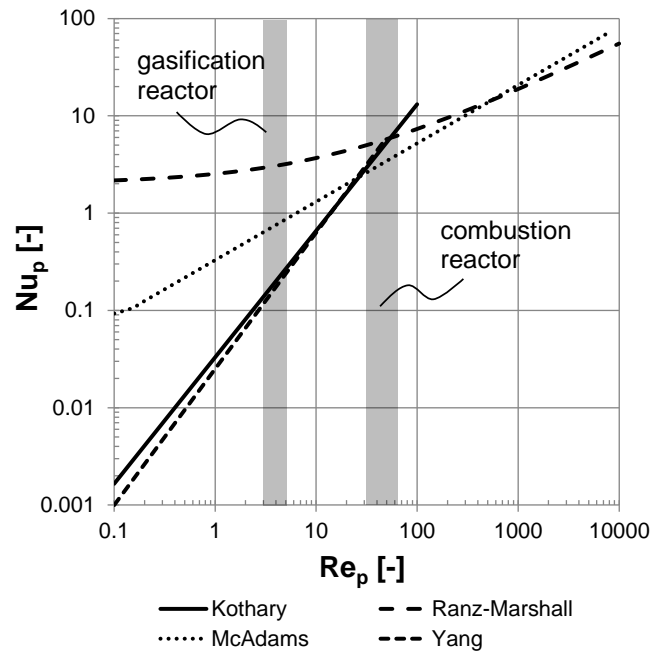
**Figure 2.6:** *Heat transfer correlations for fluidized beds.*

heat is transferred from the gas phase to the particles in the combustion reactor and how much heat is transferred from the particle to the gas phase in the gasification reactor. The function principle of the commercial plant in Güssing is explained in greater detail in section 2.2.1.

In Figure 2.6 also the range of $Re_p$ for the gasification reactor and the combustion reactor is depicted based on the superficial velocities. It can be seen that for the riser the predicted Nußelt numbers for all the correlations are in the same magnitude. However, for the gasification reactor the difference is over one magnitude.

**Heat transfer to the wall**

For the bubbling bed the heat transfer coefficient consists of three parts [39]:

- heat transfer caused by conduction through the particles, $\alpha_{cond}$

- heat transfer caused by the gas convection, $\alpha_{conv}$

- heat transfer due to radiation, $\alpha_{rad}$

These three parts sum up to the overall heat transfer coefficient, $\alpha_o$:

$$\alpha_o = \alpha_{cond} + \alpha_{conv} + \alpha_{rad} \tag{2.29}$$

The calculation of the heat transfer coefficient in the bubbling bed is much more difficult since the wall is alternately touched by particles and gas. For that purpose the *packet model* was developed to calculate the heat transfer coefficient. The model is based on the assumption that particles are swept to an immersed surface where they remain a certain time and are cooled down or heated up. The heat transfer is not mainly influenced by the contact points of the particles at the surface but more by the thin gas layer through which the heat of the particles has to be transferred to the wall or back. More details of this model can be found in the literature [28, 40]. It is not further discussed since it is not used in Barracuda and therefore not used in this work.

To calculate the heat transfer coefficient for the conductive part, $\alpha_{cond}$, the correlation by Leva can be used [41]:

$$Nu_{cond} = \frac{\alpha_{cond}d_p}{\lambda_g} = 0.525Re_p^{0.75} . \tag{2.30}$$

To calculate the gas convective part, $\alpha_{conv}$, the correlation by Baskakov [42] can be used

$$Nu_{conv} = \frac{\alpha_{conv}d_p}{\lambda_g} = 0.009Ar^{1/2}Pr^{1/3} \qquad 0.16\,\text{mm} < d_p < 4\,\text{mm} . \tag{2.31}$$

The calculation of the radiative component, $\alpha_{rad}$ , can be calculated from [39]:

$$Nu_{rad} = \frac{\alpha_{rad}d_p}{\lambda_g} = \left(\frac{e_b e_w}{e_b + e_w - e_b e_w}\right)\frac{\sigma\left(T_b^4 - T_w^4\right)}{(T_b - T_w)} , \tag{2.32}$$

where $e_b$ and $e_w$ are the emissivities of the bed particles and the wall, respectively. $\sigma$ is the Stefan-Boltzman constant, $T_b$ and $T_w$ are the temperatures of the bed and wall, respectively.

## 2.2 Biomass gasification in the dual fluidized bed system

In this section an overview about the ongoing chemical processes inside of a dual fluidized bed (DFB) steam gasification system is given. First, a short description of the DFB gasification plant in Güssing, Austria, is given. It is also modeled in this work. Afterwards, the ongoing processes on particle level are discussed. Furthermore, chemical reactions typical for DFB gasifiers are shortly presented. Also the modeling

of these processes is discussed in general since this is the basis for the modeling of the particle chemistry in Barracuda.

## 2.2.1  The dual fluidized bed gasification system

In a dual fluidized bed (DFB) system two fluidized beds are connected:

- gasification reactor

- combustion reactor.

In the following a detailed function principle of the DFB system is given. In Figure 2.7 a flowsheet of a typical DFB process located in Güssing, Austria, is depicted. Its thermal and electrical power is 8 $MW_{th}$ and 2 $MW_{el}$, respectively [6].
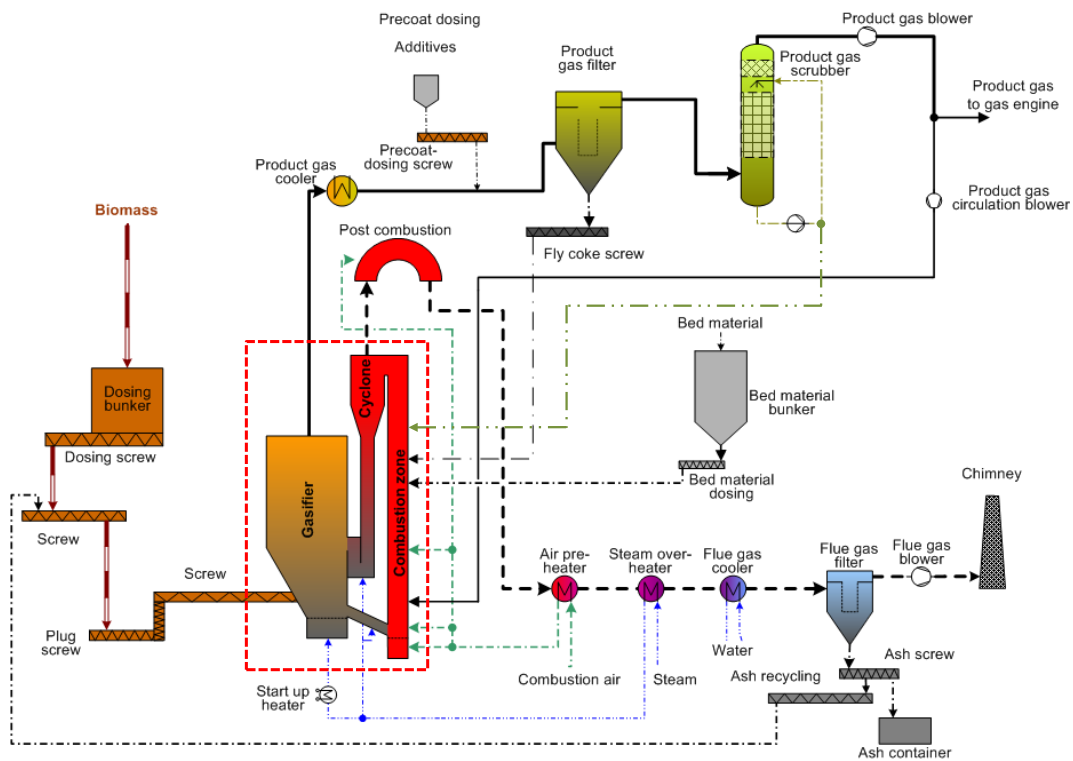


**Figure 2.7:** *Flowsheet of the CHP plant in Güssing according to Kirnbauer et al. [5]. The dashed red line shows the simulated DFB reactor system in the present work,*

The DFB system is marked with a dashed red line and also shows the part of the process which is modeled in this work. The system consists of a gasification reactor, chute, combustion reactor, cyclone, and loop seal.

Figure 2.8 shows the geometry of the Güssing DFB system. Furthermore, a scale was added for illustration of the size of the reactor system. The total height of the

system is about 9 m. The diameter of the freeboard in the gasification reactor is about 2.1 m.
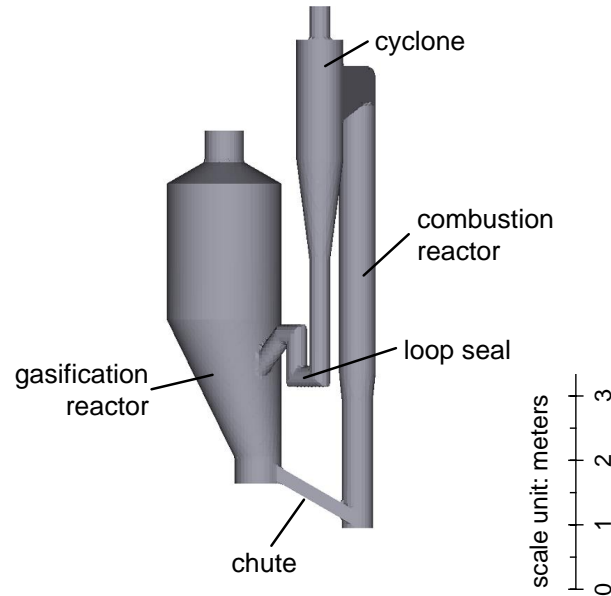


**Figure 2.8:** *Geometry of the DFB reactor of the Güssing power plant. The scale indicates the dimensions of the reactor.*

The biomass feedstock is fed into the gasification reactor which is operated as a bubbling bed. The fluidization agent is steam to produce a nitrogen-free product gas. Due to the high temperature the biomass decomposes. The product gas consists of the main components $H_2$, CO, $CO_2$, $CH_4$, and steam [2]. Furthermore, the raw product gas is loaded with a certain amount of tar. Wilk and Hofbauer [17] give for dry product gas in the Oberwart plant tar values of 1.8 g/Nm$^3$ (gravimetric) and 7.6 g/Nm$^3$ (GC-MS). The drying and devolatilization reactions which occur in the gasification reactor are endothermic [43]. Thermal energy is required to keep the temperature constant.

Between the gasification and the combustion reactor a bed material is circulating. In commercial DFB plants mostly olivine is used. The bed material transports the char to the combustion reactor which is fluidized with air and serves as transporting device for the bed material. There, the fluidization state is a fast fluidized bed. In the oxidizing atmosphere char is burnt and the bed material is heated up. For temperature control in the combustion reactor also product gas is recirculated. Recycled streams like fly char and RME emulsion are fed into the combustion reactor.

After leaving the combustion reactor the bed material is transported to the cyclone where it is separated from the flue gas. The cyclone and the gasification reactor are connected with a loop seal which is also operated in a bubbling bed regime and flu-

idized with steam.

After the gasification reactor the product gas is cooled down in a product gas cooler and fly char is separated in a product gas filter. In a scrubber the product gas is further cooled down and the tars are removed using rapeseed methyl ester (RME). The dry and clean product gas is then transported to the gas engines where it is burnt and electricity is generated.

The flue gas is transported to a post combustion chamber to ensure total combustion. After several cooling steps the flue gas is filtered and transported to the chimney.

## 2.2.2  Thermal conversion of biomass particles

Wood particles always contain a certain amount of water which is also called moisture. In this work the moisture content is defined as

$$x_{moisture} = \frac{m_{moisture}}{m_{wood}} \tag{2.33}$$

If a biomass particle is heated up the particle dries first. At about 100 °C the drying processes start and occur approximately until 150 °C [44]. The drying process is strongly endothermic because of the high enthalpy of evaporation of water, $\Delta h_{evap}$. Because of that the temperature of the particle remains constant since the energy is consumed by the drying processes. The moisture then leaves the biomass particle as steam.

If the temperature is further increased the devolatilization processes start. The released volatiles sum up to about 85% of the total mass of the dry biomass. At this point the large biomass molecules start to decompose because of the temperature and are irreversibly destroyed. The released gas consists mainly of $CO$, $CO_2$, $H_2$, $CH_4$ on dry basis.

Additionally, larger tar molecules are formed which are not fully degraded to the smaller components as mentioned previously. This first step can be also called primary pyrolysis since the molecules origin primarily from the biomass. The further conversion of the primary tars in the gas phase is then referred to as secondary pyrolysis. At about 500 °C the devolatilization processes are mostly finished [44]. The decomposition of tars is very complex due to a large amount of different tar species [45].

After all the volatiles are released a solid residue remains which is called "char". The composition of the char can be further divided into an organic part which consists mainly of carbon. Klose and Wölki [46] measured 89 wt.-% of carbon content for beech wood. The rest of the organic part is hydrogen and oxygen. The other part

is called ash and consists of inorganic components like potassium, sulfur or chlorine. Ash plays an important role regarding catalytic effects of the bed material in terms of tar decomposition [47].

The complete conversion process of biomass can then be summarized in the following reaction equation

$$\text{biomass} \rightarrow \text{moisture} + \text{wood gas} + \text{tar} + \text{char}$$
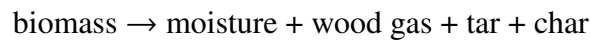
So, three major groups of products after the conversion process can be distinguished:

- non-condensable gases which are referred to as *wood gas*: $CO$, $CO_2$, $H_2$, $CH_4$ including water,

- condensable "gases" which are lumped together and are called *tars*: longer molecules like naphthalene or benzene,

- the solid residue which is referred to as *char*.

Di Blasi [48] showed that the yields of gas, tar and char that origin from the biomass change with temperature.

## 2.2.3 Other chemical reactions in a DFB system

Apart from the biomass conversion processes there are further important reactions which occur in a DFB system. In this work these are divided into two groups:

- homogeneous reactions which occur only in the gas phase between two or more gas species,

- heterogeneous reactions where at least one solid reaction partner is present.

The most important homogeneous reactions occurring in a DFB system are shown in Table 2.2. These are the water-gas-shift reaction which strongly influences the product gas composition in the gasification reactor. The heavier tar components can react with water via the steam reforming reaction to carbon monoxide and hydrogen. The strongly exothermic oxidation reactions of carbon monoxide, hydrogen and methane occur mostly in the combustion reactor since it is fluidized with air and recirculated product gas is burnt there for temperature control.

The second category are the heterogeneous reactions which are shown in Table 2.3. These are the gasification reactions of carbon or char with steam, carbon dioxide and hydrogen. More relevant for the combustion reactor is the strongly exothermic oxidation reaction of char which provides also heat for bed material heat-up.

**Table 2.2:** *Homogeneous reactions occurring in a DFB system. Values for the heat of reaction are taken from [44].*

| reaction | name | $\Delta h_R^0$ [kJ/mol] |
|---|---|---|
| $CO + H_2O \leftrightarrow CO_2 + H_2$ | water gas shift | $-40.9$ |
| $C_mH_n + m\,H_2O \leftrightarrow m\,CO + (m + \frac{n}{2})\,H_2$ | steam reforming | |
| $2CO + O_2 \rightarrow 2CO_2$ | carbon monoxide oxidation | $-283$ |
| $2H_2 + O_2 \rightarrow 2\,H_2O$ | hydrogen oxidation | $-242$ |
| $CH_4 + 2O_2 \rightarrow CO_2 + 2H_2O$ | methane oxidation | $-283$ |

**Table 2.3:** *Heterogeneous reactions occurring in a DFB system. Values for the heat of reaction are taken from [44].*

| reaction | name | $\Delta h_R^0$ [kJ/mol] |
|---|---|---|
| $C + H_2O \rightarrow CO + H_2$ | steam gasification | $+131.3$ |
| $C + CO_2 \rightarrow 2\,CO$ | Boudouard reaction | $+172.4$ |
| $C + 2H_2 \rightarrow CH_4$ | hydrogen gasification | $-74.9$ |
| $C + O_2 \rightarrow CO_2$ | oxidation | $-393.4$ |

## 2.2.4 Modeling of the chemical processes inside a DFB system

### Drying

Drying of biomass particles is the first step that has to be modeled. A very simple and also often used method is to use an Arrhenius approach:

$$\dot{r}_{drying} = k_0 e^{-\frac{E_a}{R_m T_p}} m_{moisture}\,. \tag{2.34}$$

Its simplicity is a great advantage and also the temperature dependence of the drying process can be taken into account. However, the extrapolation is difficult to conditions different from which the kinetic parameters were derived.

Some authors [49, 50] used an approach which correlates the evaporation rate as follows: $\dot{r}_{drying} \sim T_p - T_{evap}$ for $T_p \geq T_{evap}$ and 0 for $T_p < T_{evap}$. Barracuda only allows implementations according to Eq. (2.34) therefore, these are used in the further parts of the this work.

**Devolatilization**

Modeling of devolatilization of biomass particles is a very challenging task. Since biomass consists of very large molecules the various reaction products resulting from its conversion is broad. This is also reflected in the fact that up to now it is not possible to model the wood gas composition after primary and secondary pyrolysis without performing measurements to calibrate the model [16].

For already dried biomass particles very basic models divide the conversion into solely two componente: gas and char. No tar reactions are considered. Figure 2.9 shows the graphical implementation of such an approach. Liu et al. [51] use such an implementation in their CPFD study of an 1 $MW_{th}$ DFB unit, see section 4.1.
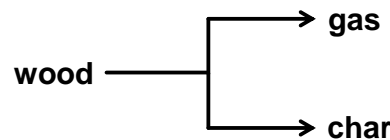


**Figure 2.9:** *Schematic drawing of a simple 1-step mechanism for modeling of pyrolysis.*

The aforementioned division into wood gas, tar and char can also be reflected in the modeling of the conversion process, Figure 2.10. This is very common in literature and used in many studies [52, 53, 54, 55, 56, 57, 58, 59, 60, 61, 62]. The wood particle decomposes via three parallel reactions into gas, tar and char. If secondary pyrolysis reactions should also be considered the conversion of tar can be implemented.
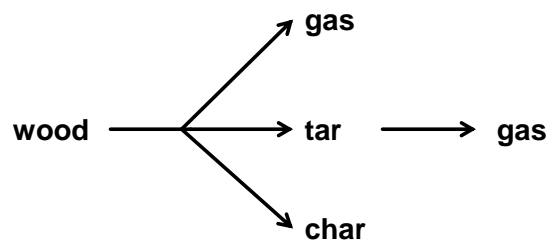


**Figure 2.10:** *Schematic drawing of a mechanism which also takes into account the formation of tar and a secondary pyrolysis step.*

Implementation of the kinetics is commonly done with a simple Arrhenius approach:

$$\dot{r}_{pyrolysis} = k_0 e^{-\frac{E_a}{R_m T_p}} m_{biomass} \tag{2.35}$$

However, these models only consider the three pseudo-components and the actual composition of the gas species either after the primary and/or the secondary pyrolysis

step has to be specified. In most cases the composition of the gas species is then fixed with mass fractions of the relevant components, CO, $CO_2$, $H_2$, $CH_4$ and water.

Furthermore, there exist even more advanced reaction mechanisms for the conversion of biomass which are more complex than the one presented in Figure 2.10. The mechanism of Ranzi et al. [63] includes conversion mechanisms of the three main components of biomass: cellulose, hemicellulose and lignin. Each of these three components has a separate conversion mechanism in the model. However, due to its complexity it was not used in the Barracuda model in this work and is not discussed further here.

## 2.3 Dimensional analysis

### 2.3.1 Basics

Dimensional analysis is a powerful tool since it allows finding relationships where small or easier to handle models can be built and the results can then be transferred to the real version. Furthermore, dimensional analysis gives a way to reduce the relevant quantities by forming non-dimensional numbers. By this the number of necessary measurements can be reduced significantly. It allows deriving a correlation of various parameters without knowing the exact formula that describes the problem.

Dimensional analysis has a broad range of application and also in fluidized bed engineering as discussed below. It provides the necessary information so that cold flow models can be built which show the same hydrodynamic behavior as the commercial plant which is the basis for fluid mechanic observations. Cold flow models can be operated at ambient conditions, e.g. air can be used as fluidization agent, which allows easy handling. Transparent materials, like e.g. acrylic glass, can be used for construction so additionally visual observations of the behavior of the fluidized bed are possible.

Dimensional analysis deals with similarity concepts. But this has nothing to do with similarity from the everyday talking since although models called "similar", the cold flow model should show – at least theoretically – the same hydrodynamic behavior as the commercial plant.

Dimensional analysis states that every physical formula $f(\chi_1, \chi_2, ...) = 0$ can be transformed into a dimensionless form. The $\chi_i$ are the physical variables. The basic concept of the dimensional analysis is the Buckingham Pi theorem. It states that every physical formula can be written in the following form [64]:

$$f(\Pi_1, \Pi_2, ...) = 0 \tag{2.36}$$

The $\Pi_i$ are dimensionless products of some or all of the physical variables $\chi_i$.

According to the Buckingham theorem one can form $p = n - r$ linearly independent Pi groups, where $p$ is the number of dimensionless terms that can be formed, $n$ is the number of physical variables and $r$ is the number of dimensions for a given problem.

There are two ways to find the Pi groups:

1. Find the governing or describing equation of a problem and nondimensionalize it, as done by Glicksman [65, 66].

2. Look for the influencing variables for a problem and form dimensionless numbers, as done by Reh [67] or Grace [68].

## 2.3.2  Nondimensionalizing the governing equations: Glicksmans full and simplified set

Glicksman [65] nondimensionalized the governing equations for two-phase flow. In his derivation no energy balance is considered and isothermal flow is assumed. The mass transfer between the two phases is neglected. Drag is assumed to be the dominant exchange source of momentum between the two phases, all the other forces on particles (like virtual mass and history effects) are omitted. For the gas momentum equation the gas-phase shear stress is neglected. Defining a momentum conservation equation for solids phase is difficult due to the necessary solid-phase stress tensor. Glicksman omitted the solids stress tensor in his derivation.

The continuity equations of the gas and solids phase are as follows:

$$\frac{\partial}{\partial t}(\varepsilon_g \rho_g) + \nabla \cdot (\varepsilon_g \rho_g \mathbf{u}_g) = 0, \tag{2.37}$$

$$\frac{\partial}{\partial t}(\varepsilon_p \rho_p) + \nabla \cdot (\varepsilon_p \rho_p \mathbf{u}_p) = 0. \tag{2.38}$$

The momentum balances are:

$$\frac{\partial}{\partial t}(\varepsilon_g \rho_g \mathbf{u}_g) + \nabla \cdot (\varepsilon_g \rho_g \mathbf{u}_g \mathbf{u}_g) = -\nabla(\varepsilon_g p) + \varepsilon_g \rho_g \mathbf{g} - \beta_d(\mathbf{u}_g - \mathbf{u}_p), \tag{2.39}$$

$$\frac{\partial}{\partial t}(\varepsilon_p \rho_p \mathbf{u}_p) + \nabla \cdot (\varepsilon_p \rho_p \mathbf{u}_p \mathbf{u}_p) = \varepsilon_p \rho_p \mathbf{g} + \beta_d (\mathbf{u}_g - \mathbf{u}_p) . \tag{2.40}$$

Nondimensionalizing of these equations including the boundary conditions and the drag correlation gives the Pi groups of the *full set*:

$$\frac{u_0^2}{gL}, \frac{\rho_p}{\rho_g}, \frac{\rho_p u_0 d_p}{\mu_g}, \frac{\rho_g u_0 L}{\mu_g}, \frac{G_s}{\rho_p u_0}, \frac{L}{D}, \text{bed geometry}, \phi_p, \text{PSD} . \tag{2.41}$$

To apply the full set all the dimensionless groups must be equal between cold flow model and commercial plant. Using ambient air sets fluid density and viscosity to fixed values and only one unique set of values results which matches the full set. This can often lead to large cold flow models.

To provide more freedom in choosing the dimensions and to allow for smaller sizes of the cold flow models Glicksman simplified his full set [66]. He aimed for a reduction of the scaling parameters.

The idea is to consider the drag term in the limits of large and small Reynolds numbers. If the simplified set is valid in both limits, so Glicksman's assumption, it should be a good approach for simplification and should be valid for bubbling as well as for fast fluidized beds. Glicksman also argued that if the simplified set holds in both limits with high and low Reynolds numbers, it should hold, at least approximately, also in the intermediate Reynolds regions. Results show that both limits give the same set of scaling parameters. The simplified set gives more flexibility, e.g. the length ratio could be chosen and the size of the cold flow model can be adapted. It is as follows:

$$\frac{u_0^2}{gL}, \frac{\rho_p}{\rho_g}, \frac{u_0}{u_{mf}}, \frac{L_1}{L_2}, \frac{G_s}{\rho_p u_0}, \text{bed geometry}, \phi_p, \text{PSD} . \tag{2.42}$$

### 2.3.3 The diagrams of Reh and Grace

Reh deals with the dynamic similarity of particles in fixed beds, fluidized beds and pneumatic conveying [67]. If geometric similarity is ensured similarity for these three conditions is only achievable if the viscous, gravity and inertia forces or their ratios, respectively, are kept constant. So, to ensure similarity he states that the four parameters should remain constant:

- geometrical similarity

- $Re_p = \frac{d_p u_0}{\nu_g}$

- $Fr_p^2 = \frac{u_0^2}{d_p g}$

- $\frac{\rho_g}{\rho_p - \rho_g} = const.$

The first point ensures geometrical similarity. All dimensions of the cold flow model and the commercial plant have to be in the same ratio. Additionally, also the viscous forces, the gravitational forces and the inertia forces have to be considered – their ratios have to be equal to obtain similarity. $Re_p = \frac{inertia}{viscous}$ and $Fr_p = \frac{inertia}{gravitational}$ are kept constant. Reh aimed to describe the porosity $\varepsilon_g$ with $Re_p$, $Fr_p^2$ and $\frac{\rho_g}{\rho_p - \rho_g}$ which then leads to the diagram. It should be noted that the term $\frac{u_0^2}{d_p g}$ is also often only defined as $Fr_p$. Reh used the quadratic definition, therefore it is defined in the previous list as such.

Reh's argumentation is valid if all the particles are spherical and of the same size (no particle size distribution). Furthermore, the viscosity and density of the gas as well as the density of the solid should be constant. In general Reh finds for the three conditions fixed bed, fluidized bed and pneumatic conveying the following relationship:

$$\varepsilon_g = f\left(Re_p, Fr_p^2, \frac{\rho_g}{\rho_p - \rho_g}\right) . \tag{2.43}$$

Grace also introduced considerations to depict the fluidization state in a diagram [68]. He suggested that the porosity $\varepsilon_g$ depends on the following variables:

$$\varepsilon_g = f(\rho_g, g, \Delta\rho, \mu_g, d_p, u_0) , \tag{2.44}$$

where $\Delta\rho = \rho_p - \rho_g$.

Compared to Reh these are the same quantities. Grace leaves out the geometric similarity and only focuses on the bed behavior and suggests that this can be described only by the voidage $\varepsilon_g$.

In Eq. (2.44) there are seven quantities in three dimensions (mass, time, length). Therefore, a correlation of four dimensionless quantities, $\varepsilon_g$, $d_p^*$, $U^*$ and $\Delta\rho/\rho_g$ can be formed:

$$\varepsilon_g = g(d_p^*, U^*, \Delta\rho/\rho_g) , \tag{2.45}$$

where

$$d_p^* = d_p \left(\frac{\rho_g g \Delta\rho}{\mu^2}\right)^{1/3} = Ar^{1/3} , \tag{2.46}$$

and

$$U^* = u_0 \left( \frac{\rho_g^2}{\mu_g g \Delta\rho} \right)^{1/3} = \frac{Re_p}{Ar^{1/3}} .$$

(2.47)

The two parameters $d_p^*$ and $U^*$ are useful because each involves only the particle diameter or the superficial velocity. That is an advantage compared to Reh's diagram because there in both dimensionless variables occurs the velocity. In Figure 2.11 the extended version by Schmid et al. [1] is shown. It also contains the particle classification after Geldart [30].
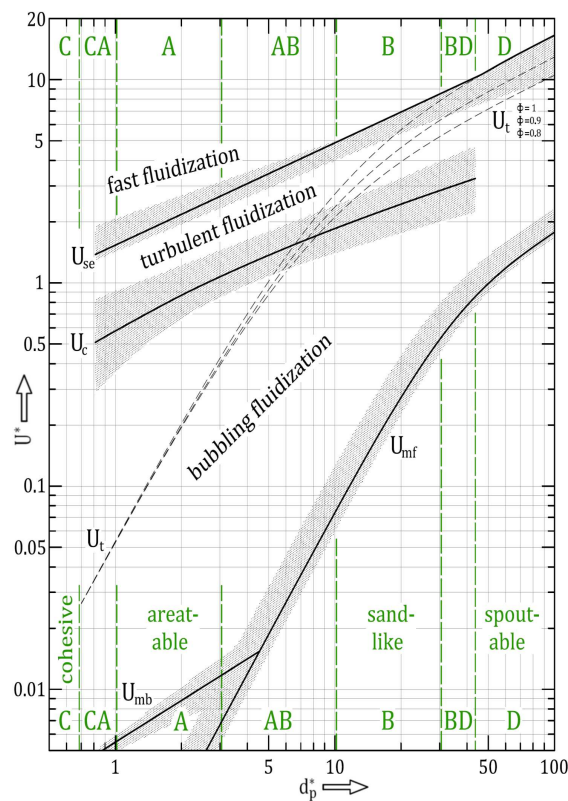


**Figure 2.11:** *Regime diagram by Grace [68] extended by Schmid et al. [1].*

# 2.4 Computational methods to model fluidized beds

## 2.4.1 Overview over available methods

Computational power has been increasing in the last decades coming along with more powerful resources for computational simulation of gas/solid flows in greater detail. Computer simulations are an addition to experiments which can greatly enhance and complete the understanding of the ongoing processes on particle level inside fluidized beds.

Gas/solid simulations can be carried out in various levels of detail with different accuracy and computational cost. Computational cost is also related to the number of particles in the system. Whereas for small laboratory plants the number of particles is in the order of $10^8$ it increases to $10^{11}$ to $10^{12}$ for large industrial systems.

The available methods are shown in Figure 2.12 with decreasing level of detail in modeling the gas and particle phase, respectively.
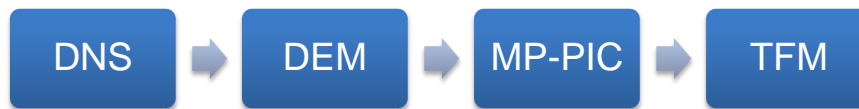
**Figure 2.12:** *Available computational methods for the calculation of gas/solid flows.*

The most detailed way of simulating gas/solid flows is the direct numerical simulation (DNS). The Navier-Stokes equations are solved without any turbulence model and all the spatial and time scales need to be calculated. The exchange of momentum between gas and solid phase is solely determined by the interaction of the gas with the particle surface. The movement of the particles is calculated with Newton's equations of motion for translation and rotation. Due to the small grid sizes and therefore large computational cost only small numbers of particles can be used. Because of this such methods are only of interest in research and cannot yet be applied to larger scales. Van der Hoef et al. [69] calculated the drag law caused by slow fluid flow around arrays of spheres.

The level of detail can be reduced in the description of the gas phase by averaging procedures. The averaging leads to an additional closure term, in that case an exchange term between gas and solid phase. The individual elements or particles are still calculated and their collisions are resolved [70]. Such approaches are called *discrete element method* or DEM. A first implementation was carried out by Cundall and Strack [71]. Deen et al. [72] provided a review of such methods and the governing equations of

gas the equations of motions of the particle phase. However, due to the resolution of the individual particles the computational cost is still very high and not applicable for large industrial plants [14].

If also the particle phase is averaged and the single particles are not resolved any more the gas and particle phase both are described as interpenetrating continua. Such approaches are called *two fluid models* or TFM, since also the particle phase is simulated with an fluid-like behavior. TFMs are widely used for modeling of fluidized beds and first implementations were carried out by Anderson and Jackson [73]. Therefore, for gas and solid phase continuity and momentum equations have to be solved [74]. Besides the term for momentum exchange between the gas and the particle phase also a closure is required for the solid phase. For that purpose a separate solid stress is added. An advantage is the low computational costs for such methods. However, in real plants the particles occur in particle size distributions and Hjertager et al. [75] reported a quadratic increase of computational effort with the number of phases.

An implementation located somewhere between the DEM and the TFM is the MP-PIC approach or multi-phase particle-in-cell approach. It overcomes the high computational cost of the DEM by grouping particles with same properties like diameters, densities or velocities into computational particles or clouds. These clouds are tracked with the Newton's equations but the collisions are not resolved and calculated with a continuum approach similar as it is done in the TFM. The gas phase is calculated in the same way as in DEM and TFM, therefore also the momentum exchange term between gas phase and particle phase is used. The governing equations are described by Andrews and O'Rourke [76] and Snider [77]. One implementation of the MP-PIC approach is the commercial code Barracuda by CPFD Software, LLC, and is used in this work. A more comprehensive description of the governing equations is given in the following section.

### 2.4.2 Governing equations of Barracuda

As already mentioned, Barracuda works with the Multi-Phase Particle-in-Cell (MP-PIC) approach. The following derivation is based on the work of Andrews and O'Rourke [76], Snider [77] and Snider et al. [78]. The continuity and momentum transfer equations for the gas phase are as follows:

$$\frac{\partial \left( \varepsilon_g \rho_g \right)}{\partial t} + \nabla \cdot \left( \varepsilon_g \rho_g \mathbf{u}_g \right) = \delta \dot{m}_p \,, \tag{2.48}$$

$$\frac{\partial \left( \varepsilon_g \rho_g \mathbf{u}_g \right)}{\partial t} + \nabla \cdot \left( \varepsilon_g \rho_g \mathbf{u}_g \mathbf{u}_g \right) = -\nabla p + \mathbf{F} + \varepsilon_g \rho_g \mathbf{g} + \nabla \cdot \left( \varepsilon_g \tau_g \right) \ . \qquad (2.49)$$

In Barracuda the description of the particle phase is carried out by using a probability density function $f(\mathbf{x}, \mathbf{u}_p, \rho_p, V_p, t)$, where $\mathbf{x}$ is the location in space, $\mathbf{u}_p$ is the particle velocity, $\rho_p$ is the particle density, $V_p$ is the particle volume, and $t$ is the time. The particles are then conserved by using a Liouville equation for $f$ which is of the form:

$$\frac{\partial f}{\partial t} + \nabla \cdot \left( f \mathbf{u}_p \right) + \nabla_{\mathbf{u}_p} \cdot \left( f \mathbf{a}_p \right) = 0 \,, \qquad (2.50)$$

with $\nabla_{\mathbf{u}_p}$ as the nabla operator with respect to particle velocity.

The mass source term $\delta \dot{m}_p$ in Eq. (2.48) can be formulated with:

$$\delta \dot{m}_p = - \iiint f \, \frac{dm_p}{dt} \, dm_p \, d\mathbf{u}_p \, dT_p \ . \qquad (2.51)$$

The particle acceleration $\mathbf{a}_p$ is described in the following way

$$\mathbf{a}_p = D_p \left( \mathbf{u}_g - \mathbf{u}_p \right) - \frac{1}{\rho_p} \nabla p + \mathbf{g} - \frac{1}{\varepsilon_p \rho_p} \nabla \tau_p + \frac{\bar{\mathbf{u}}_p - \mathbf{u}_p}{\tau_D} \ . \qquad (2.52)$$

Eq. (2.52) is valid for small particle volume fractions. In Barracuda's newer versions (from Version 16 on) a blend function for the acceleration is implemented. Additionally to Eq. (2.52) a velocity is used near the close pack state as described by O'Rourke and Snider [79].

The drag function $D_p$ is linked with the drag coefficient, $C_d$, via

$$D_p = \frac{3}{4} C_d \frac{\rho_g}{\rho_p} \frac{|\mathbf{u}_g - \mathbf{u}_p|}{d_p} \ . \qquad (2.53)$$

The interparticle stress $\tau_p$ is expressed in the following way:

$$\tau_p \left( \varepsilon_p \right) = \frac{P_s \varepsilon_p^\beta}{\max \left[ \varepsilon_{cp} - \varepsilon_p, \alpha \left( 1 - \varepsilon_p \right) \right]} \,, \qquad (2.54)$$

with $\alpha$ and $\beta$ as dimensionless coefficients.

The particle volume fraction $\varepsilon_p$ and the momentum exchange rate between the gas and the solid phase $\mathbf{F}$ are related with $f$:

$$\varepsilon_p = \iiint f \, \frac{m_p}{\rho_p} \, dm_p \, d\mathbf{u}_p \, dT_p \,, \qquad (2.55)$$

$$\mathbf{F} = - \iiint f \left\{ m_p \left[ D_p \left( \mathbf{u}_g - \mathbf{u}_p \right) - \frac{1}{\rho_p} \nabla p \right] + \mathbf{u}_p \frac{dm_p}{dt} \right\} dm_p \, d\mathbf{u}_p \, dT_p \ . \qquad (2.56)$$

## 2.4.3 Implementation of drag laws

In a fluidized bed the gas flow exerts a force on the particles. The drag force acts in the direction of the gas flow. If the drag force equals or is larger than the gravity force acting on the particle the particle leaves its static position and starts to act in that typical fluid-like motion which is characteristic for fluidized beds.

Van Wachem et al. [23] reported that based on their simulations the drag and gravity force have the most influence on the particle behavior.

In the present work the impact of four drag laws on the simulation results is investigated. Therefore, they are shortly presented here. The used drag laws are:

- EMMS [39]

- Ganser [80]

- Turton-Levenspiel [81]

- Wen-Yu/Ergun [82]

The drag coefficient is a function of the particle Reynolds-number, $C_d = f(Re_p)$ and a widely used form is of the following type [83]:

$$C_d = \frac{24}{Re_p} \left( 1 + aRe_p^b \right) + \frac{c}{1 + dRe_p^e}, \qquad (2.57)$$

In Eq. (2.57) the coefficients $a$, $b$, $c$, $d$ and $e$ depend on the drag law. The drag laws by Ganser, Turton-Levenspiel and Wen-Yu/Ergun follow the previous form.

The EMMS drag model is based on an energy-minimization multiscale approach. The drag model uses structure parameters from gas–solid interactions. More information can be found in in Yang et al. [39].

The Wen-Yu/Ergun drag law was introduced by Gidaspow [82]. It combines the drag law proposed by Wen and Yu [32] with the Ergun equation [31]. In between a blend function is used which interpolates between the two cases. According to Gidaspow [82] the Wen-Yu equation should be used for $\varepsilon_g > 0.8$ and the Ergun equation for $\varepsilon_g < 0.8$.

In Appendix A the formulas for the drag laws implemented in Barracuda are given in greater detail.

# 3 Fluidization of binary mixtures of dissimilar solids

In this chapter fluidization of beds, consisting of two particle species which are of different size and density, are discussed. First, fluid mechanical aspects of such *binary mixtures of dissimilar solids* are presented. This includes characteristic velocities, mixing mechanisms, times for separation, pressure profiles and bed expansion. Afterwards, the influence of various parameters such as density, diameter and shape of the particles as well as composition of the mixture, superficial velocity and bed geometry. Finally, mixing processes in circulating devices are presented.

---

**Parts of this chapter have been submitted for publication as:**

S. Kraft, H. Hofbauer. Fluidization of binary mixtures of dissimilar solids: A review. *Powder Technology*, submitted, 2017

---

## 3.1 Terminology

In this review the terms binary fluidized bed or binary bed means the use of a bed consisting of two particle species. Binary fluidization means the process of the fluidization of a binary bed. The two particle species are of different size and density which is referred to as dissimilar solids or also as a dissimilar mixture.

Generally, in a binary fluidized bed the particles can differ in three ways:

- equal-density mixtures → differ only in size

- equal-size mixtures → differ only in density

- dissimilar mixtures → differ in density and size

In the present review only the last case is considered.

Some definitions are introduced which are somewhat vague but should serve as a way to distinguish the particle species. These are chosen according to Rowe et al. [13], Table 3.1. HEAVY and LIGHT refer to the density of the particles: HEAVY are the denser particles. SMALL and BIG refer to the size of the particles. FLUID means the component with the lower and PACKED means the component with the higher minimum fluidization velocity. This definition can only hold for particle species where the minimum fluidization velocity can be defined.

**Table 3.1:** *Summary of the terminology according to Rowe and Nienow [84].*

| property | greater | smaller |
|---|---|---|
| density | HEAVY | LIGHT |
| size | BIG | SMALL |
| minimum fluidization velocity | PACKED | FLUID |

Rowe et al. [13] state six different binary combinations which are as follows:

1. HEAVY, BIG, PACKED / LIGHT, SMALL, FLUID (HBP/LSF)

2. HEAVY, SMALL, PACKED / LIGHT, BIG, FLUID (HSP/LBF)

3. HEAVY, SMALL, FLUID / LIGHT, BIG, PACKED (HSF/LBP)

4. BIG, PACKED / SMALL, FLUID (BP/SF)

5. HEAVY, PACKED / LIGHT, FLUID (HP/LF)

6. HEAVY, SMALL / LIGHT, BIG (HS/LB)

For the last three examples one property is missing, which means that it is constant for both. Therefore, since in this review dissimilar are discussed the combinations 1, 2, 3 and 6 are of relevance, since for combination 4 the density is equal and for combination 5 the size is equal.

Additionally, two more terms can be used to characterize the behavior of the system [13]. The particles which have a tendency to move to the surface of the bed are called FLOTSAM, the ones which tend to sink are called JETSAM.

The concept of FLOTSAM and JETSAM is useful to characterize the fluidization behavior of the system but is not unique for each system. It is a characteristic of the mixture. As shown by some authors [85, 86, 87] also the former JETSAM component can act FLOTSAM if the mixture has a certain composition.

Therefore, the characterization of the mixture is only carried out with the classification according to Rowe et al. [13] since there only material properties are used. However, for very LARGE particles, like biomass, where no distinct minimum fluidization velocity can be obtained, the concept is not used. The terms FLOTSAM and JETSAM are only used to characterize the fluidization behavior of the mixture.

## 3.2 Fluid mechanics of fluidized beds with dissimilar solids

The ideal case obtaining a perfectly mixed bed is one, where all the particles have the same diameter and the same density. For such a system no segregation would occur and it would follow the same behavior as a system with only one particle species with the same diameter and density.

In case of dissimilar solids, it is discussed in this chapter, the aforementioned behavior is unlikely to occur. There will be a broad varity in possible fluidization behavior, either complete or perfect mixing or a broad range in between these extremes.

Principally, three main mixing states can be distinguished:

- complete mixing

- complete segregation

- partly mixing

In the *complete mixed* state, Figure 3.1 (a), no concentration gradients over the bed height occur. In a *complete segregated* bed two distinct layers form, where the FLOTSAM layer is at the top and the JETSAM layer is at the bottom. Between these two layers a sharp transition occurs. The third case is the *partly mixed* bed. A jetsam-rich layer forms at the bottom and a flotsam-rich at the top. In between there exists a mixed layer, where also flotsam and jetsam particles are present.

### 3.2.1 Characteristic velocities in binary fluidized beds

The minimum fluidization velocity $u_{mf}$ is a characteristic value for fluidized beds. It is part of the fluidization number $FN = u_0/u_{mf}$ which characterizes by how many times the minimum fluidization velocity is exceeded. $FN$ is an important number to characterize the fluidization state and intensity of fluidization. Furthermore, $u_{mf}$ is
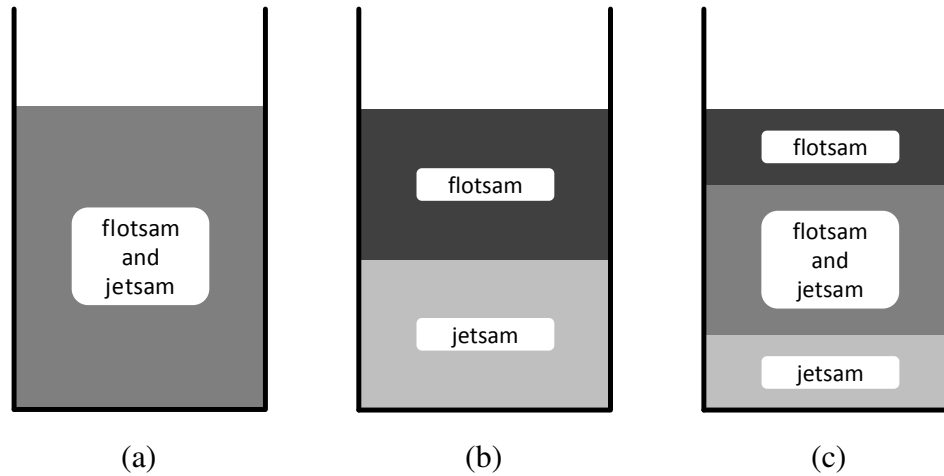
**Figure 3.1:** *Mixing states according to Chiba et al. [88]. (a) ... complete mixing, (b) ... complete segregation, (c) ... partly mixing.*

a parameter in scaling relationships as e.g. in Glicksman's simplified set [66]. For practical consideration e.g. in commercial fluidized bed boilers the knowledge or the ability of predicting $u_{mf}$ of the mixture is of relevance. *FN* determines the necessary amount of fluidization agent.

Even the shape of the particles has an influence on the minimum fluidization voidage, $\varepsilon_{mf}$, as shown by Leva et al. [89]. They found that round sand has a much lower minimum fluidization voidage than sharp sand. This is especially important for the considerations in this chapter, since the minimum fluidization characteristics of the bed material have significant influence on the minimum fluidization velocity of a mixture.

Also the question of how to define a minimum fluidization velocity for a binary mixture which consists of dissimilar solids arises. The minimum fluidization velocity of a mixture lies between the minimum fluidization velocity of the components, as shown later. Its meaningfulness can be questioned [90], since it depends strongly upon the measurement method.

The experiments and attempts to define a correct $u_{mf}$ for a mixture has brought many insights into the dark field of fluidization of dissimilar solids.

**Perfectly mixed and complete segregated beds**

For a mono-component bed which is in a fixed bed condition and an air flow is applied from the bottom then the pressure drop over the bed will increase linearly with the gas velocity: $\Delta p \sim u_0$. This is also reflected in the first term, linear in the velocity, of Ergun's pressure drop equation [31] which determines the pressure drop for particle

Reynolds numbers below 1, $Re_p < 1$. The direct proportionality of $\Delta p$ and $u_0$ increases until a point, where the minimum fluidization velocity, $u_{mf}$ is reached. This is indicated with curve (a) in Figure 3.2. From that point on the curve of the pressure drop remains constant. Therefore, for complete mixed beds $u_{mf}$ is easy to measure. When $FN > 1$ and no Geldart A particles are present, the bed is in bubbling fluidized bed condition.

Generally, in the case of the fluidization of dissimilar solids, a perfect mixing situation can hardly be obtained since the particles have by definition not the same density and size. Since the fluidization behavior of dissimilar solids is discussed perfectly mixed beds are of minor relevance but are mentioned because they are an important limiting case for further sections in this chapter.
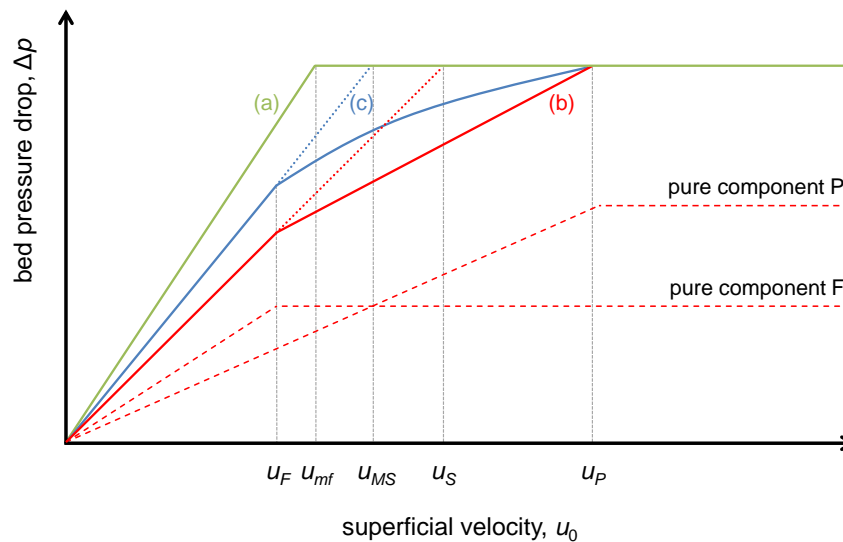


**Figure 3.2:** *Schematic $u_0,\Delta p$-diagram for a bed of a binary mixture after Chiba et al. [88]. (a) ... perfectly mixed bed, (b) ... complete segregated bed, (c) ... partial mixed bed.*

The second limiting case is the *complete segregated* bed. Under fluidization there will be two distinct layers, the upper consists only of the FLOTSAM particles the lower consists only of the JETSAM particles. If each of the two particle species has a minimum fluidization velocity, the minimum fluidization velocity of the FLUID component is called $u_F$ and the minimum fluidization velocity of the PACKED component is called $u_P$.

For a complete segregating bed which consists of two species with the minimum fluidization velocities of $u_F$ and $u_P$ the overall $u_0,\Delta p$-diagram is formed by simply adding the two curves of the pure species. This is done for curve (b) in Figure 3.2. In the region $u_0 < u_F$ the whole bed is in the fixed bed condition and $\Delta p$ over the bed increases linearly with $u_0$. When $u_F$ is reached a knee of the curve occurs and a second

linear section occurs in the region $u_F < u_0 < u_P$ with a lower slope. In this region not the whole bed is fluidized [88]. After reaching $u_P$ the bed is fully fluidized and the pressure drop remains constant.

For this case also a minimum fluidization velocity can be defined when extending the linear curve in the region $u_0 < u_F$ to the horizontal line where $\Delta p$ has reached its final value. The minimum fluidization for the complete segregated bed is then defined as $u_S$.

Complete segregating beds are investigated by Chiba et al. [88] and Yang and Keairns [91]. Chiba et al. investigated a mixture consisting of HSP/LBF particles. In another study Yang and Keairns [91] investigated a mixture which was also of the HBP/LSF type.

**Partly mixed systems**

The minimum fluidization velocity can be quite easily defined for ideal mixing or complete segregating beds. The third case is the more complicated and the one of the most practical relevance. It is unsurprisingly in between these two limiting cases and is called a *partly segregated bed*.

A minimum fluidization velocity can be defined according to the complete segregated bed: By extending the line of the flow through the fixed bed and intersect it with the horizontal line of the constant pressure. Then the minimum fluidization velocity of the mixture is obtained and is called $u_{MS}$, 3.2 (c). As it was the case in the previous section, at that velocity the coarse particles can remain not fluidized which makes this velocity more of theoretical nature and not of large importance for practical use.

The concept of the *beginning* and *complete fluidization*, $u_{bf}$ and $u_{cf}$, has been introduced. As analog to liquid/vapor equilibrium Gel'perin et al. [92] were one of the first to introduce this analogy and since then it has been used by several authors [93, 94, 90, 95, 96, 97, 98, 91, 99].

The velocity where the bed starts to fluidize is called beginning fluidization velocity, $u_{bf}$. In the pressure diagram it is the point where the linear form of the curve is left for the first time [90]. If the complete fluidization velocity is exceeded, $u_{cf}$, the bed is fully fluidized. Then the pressure drop over the bed is at its final value. Therefore, the interval $u_{bf} < u_0 < u_{cf}$ can be considered as an intermediate interval where the fluidization has started but is not full yet. This concept can also be applied to mixtures where one of the particle species has no distinct minimum fluidization velocity, as it is the case e.g. for sand/biomass mixtures.
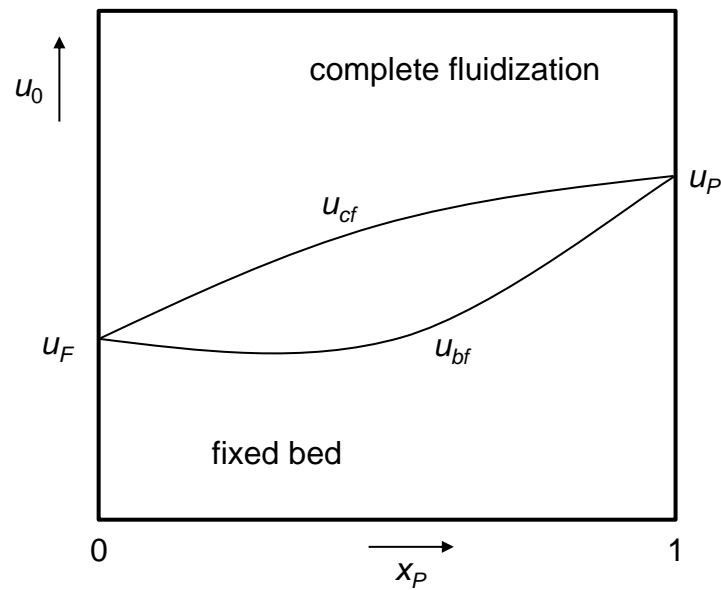
**Figure 3.3:** *Schematic diagram for the two states of beginning and complete fluidization.*

Figure 3.3 shows a schematic drawing of that concept. Without loss of generality the abscissa is the concentration of the PACKED component, $x_P$, and the ordinate is the superficial velocity, $u_0$. Therefore, at $x_P = 0$ the minimum fluidization velocity of the pure FLUID component is drawn. At $x_P = 1$ analog the minimum fluidization velocity of the PACKED component is shown.

For the case of $x_P \neq 0$ and $x_P \neq 1$ two curves are present and divide the diagram into a fixed bed region and a complete fluidization region. If $u_0 < u_{bf}$ the bed is in the fixed state. However, the diagram as shown in Figure 3.3 is only relevant for mixtures with distinct values for $u_F$ and $u_P$.

Fotovat et al. [100] introduced for a bubbling bed with large biomass spheres and cylinders the initial bubbling velocity, $u_{ib}$, which occurs between $u_{bf}$ and $u_{cf}$, $u_{bf} < u_{ib} < u_{cf}$ . This can also be obtained from pressure fluctuations measurements since the bubble size is correlated with pressure fluctuations [101]. Therefore, a sudden change of the frequency of the pressure measurement indicates the beginning of a bubbling state.

However, which velocity ($u_{MS}$, $u_{bf}$, $u_{ib}$, $u_{cf}$) to use e.g. for design calculations remains open for discussion. For industrial application the velocity $u_{cf}$ might be the most usable since the whole bed is fluidized from there on.

## 3.2.2 Mixing phenomena in beds consisting of dissimilar solids

### Influence of bubbles on mixing

Bubbles are the reason for solids mixing in fluidized beds. For this chapter relevant aspects for the further discussion are presented. A schematic drawing of a bubble moving through a bottom layer of particles is shown in Figure 3.4. When the fluidization agent enters the bed, small bubbles form at the distributor plate. Once inserted into the bed the bubbles move upwards. On their way to the top of the bed coalescence of bubbles occurs and they grow in size. Therefore, over the height the bubble size increases and the bubble frequency decreases [102]. On their way to the top the bubbles displace the particles which is the basic mechanism behind particle mixing in fluidized beds.

The region beneath the bubble is called the wake region. If a bubble passes by the particles have to fill up the former solid free region of the bubble. Because of this mechanism the bubble is dragging solids behind. The wake region of the bubble is the driving force of mixing processes in fluidized beds [28].
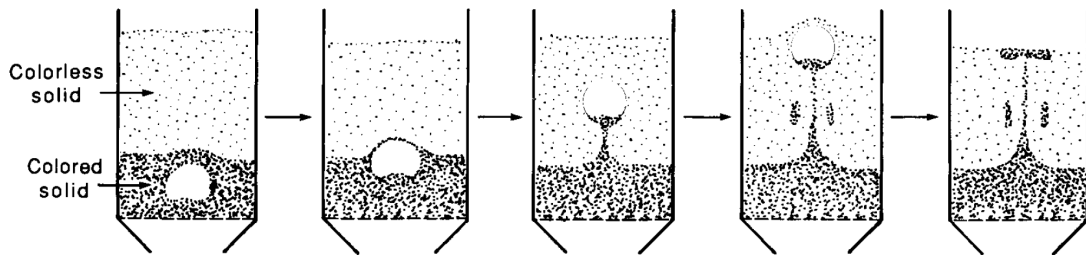


**Figure 3.4:** *Displacement of jetsam particles in the wake of a bypassing bubble (taken from Kunii and Levenspiel [28]).*

A picture of an experiment for mixing of dissimilar particles is shown in Figure 3.5. It shows the punctuation of a jetsam layer at the bottom which is penetrated by bubbles. The jetsam particles in the wake region are marked with a red dotted line.

The two-phase theory introduced by Toomey and Johnstone [103] gives an estimate of the gas flow which moves through the bed in the form of bubbles:

$$\dot{V}_b \sim u_0 - u_{mf} \tag{3.1}$$

Since the movement of bubbles is assumed to be the main cause for particle mixing or segregation processes, it makes sense to also correlate the degree of mixing with the *excess velocity* $(u_0 - u_{mf})$. For mono-component beds with a narrow particle size distribution the measurement of $u_{mf}$ is easy. However, it is much more difficult to
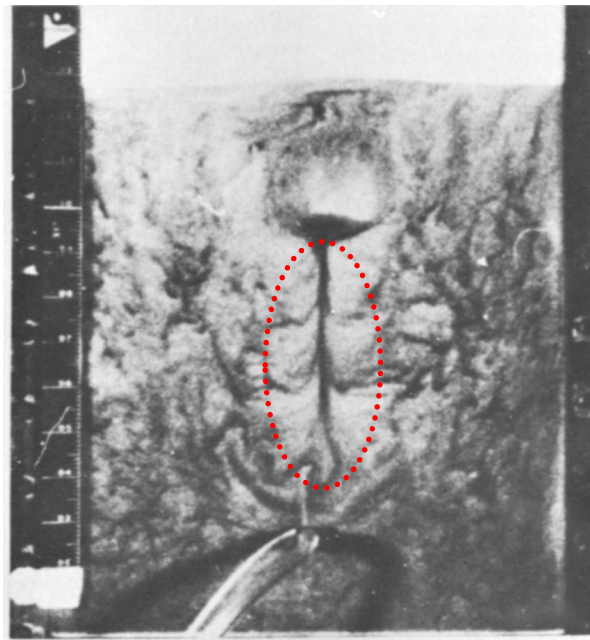
**Figure 3.5:** *Displacement of jetsam particles with bubbles in an experiment conducted by Rowe and Nienow [84].*

define a distinct value of the minimum fluidization velocity in binary systems because of segregation processes, as discussed in section 3.2.1. That is why an appropriate value of the minimum fluidization velocity for binary beds has to be chosen.

Rowe et al. [13] stated that the wake of the bubbles is the reason why jetsam particles can also be transported in the upper layers of the fluidized bed. The jetsam particles gather in the wake of the bubbles and are then transported upwards. Since mixing can only occur due to bubbles the earliest moment where segregation processes can occur is when the minimum fluidization of the FLUID component, $u_F$, is exceeded [104]. The more the fluidization velocity is increased, the more bubbles occur and therefore mixing is improved.

### Overview about the mixing mechanisms

A very extensive work on qualitative observations of fluidization mechanics of dissimilar solids was done by Rowe et al. [13]. All the investigated particle species are of diameters which are notably below 1 mm, and all used particle species have a distinct minimum fluidization velocity.

The second field is the mixing behavior of large particles, especially biomasses. Many studies in that field have been conducted by Zhang et al. [105, 106, 107, 108] and Fotovat et al. [109, 100, 110, 111].

Rowe et al. [13] identified four mixing mechanisms.

- **Lifting of particles in the wake of rising bubbles.** For the case of jetsam particles, the bubbles carry the jetsam-rich material from the bottom of the bed up to the top. There the bubbles erupt and distribute the jetsam particles across the surface. Rowe et al. [13] consider this mechanism the most important one.

- **Falling through bubbles.** If the rising gas velocity cannot support the particles they will fall through the bubbles, which act as free space. Rowe et al. [13] pointed out that this is the only way for large particles to move downwards in the bed. Beeckmans et al. [112] pointed out that this is only reasonable if the minimum fluidization velocity of the BIG particles exceeds that of the SMALL particles.

- **Inter-particle percolation.** This effect is supposed to be only relevant in regions which were disturbed by bubbles shortly before. If the small particles are also the smaller ones they may move downwards in the bed due to interstitial percolation. Chiba et al. [85] found a reverse phenomenon of that effect where the smaller and denser particles moved upwards. The effect was only observed if the small particles are sufficiently small and low in concentration in the bed.

- **Quasi-hydrostatic effect.** This effect causes particles to act flotsam or remain at the top of a bed of denser particles. Rowe et al. [13] pointed out that this is no effect causing segregation but preserving it.

For biomass/sand mixtures Zhang et al. [106] identified three mechanisms of segregation which are of similar nature as the mechanisms discussed above:

- **Percolation.** The segregation due to percolation occurs because of small vibrations at low fluidization rates. As a consequence, the small sand falls through the voids of large biomass particles. Therefore, the biomass accumulates at the top and segregation occurs.

- **Buoyancy.** For buoyancy driven segregation the authors calculate the ratio of buoyancy force and gravitational force. If the density of the expanded fluidized bed is larger than the density of the pure biomass, the biomass particles will act flotsam and will move to the surface of the bed.

- **Segregation caused by bubble motion.** Whereas the first two mechanisms occur for conditions where bubble movement is low this mechanism becomes

more present with higher fluidization rates and therefore more bubbling motion. Biomass is transported upwards in the wake of the bubbles. At the surface the bubbles erupt and the biomass is deposited at the bed surface. This is the same as the first mechanism discussed by Rowe et al. [13] earlier in this section.

Pressure fluctuations contain information about bubble behavior. The frequency of the fluctuations can be correlated with the bubble frequency and the amplitude or standard deviation contains information about the bubble size [113].

Zhang et al. [105] measured pressure fluctuations in a bed with large biomass particles. For a fixed fluidization rate the authors found that the standard deviation of the pressure signals decreases with increasing biomass concentration. The authors state that this could be due to the lesser probability of bubble coalescence.

Fotovat et al. [100] also investigated the influence of large biomass particles on the bubble behavior in a bubbling fluidized bed. Similar to Zhang et al. [105] they found the bubble size to decrease with higher biomass loadings. Biomass that is present in the bed leads to bubble breakage.

Furthermore, in another study [111] it was shown that also the shape of biomass particles can influence the bubble properties. They found that the bubble breakage is higher if cylindrical particles are present compared to spherical particles. Therefore, if the sphericity of the biomass particles was decreased, the bubble breakage is enhanced.

Chen et al. [114] pointed out that large bubbles worsen heat and mass transfer processes. If large particles are added to the bed bubbles are destroyed and the transfer processes are enhanced. They investigated mixtures from titanium slag (HEAVY and SMALL) and carbon particles (LIGHT and BIG) and emphasize that the superficial velocity has a significant influence on bubble size and bubble coalescence.

Fotovat et al. [100] also found that at the center of the bed the bubble frequency increases if the mass fraction of the biomass is increased. The authors argue that this is caused by the breakage of large bubbles. Increasing biomass concentration from 2 to 16 wt.-% in a sand fluidized bed shows significant lower void fractions at the wall of the bubbling bed for high fluidization velocities and the bubble phase is more present in the center of the bed. The dense or emulsion phase is more present in the wall region. Such behavior is also observed for beds consisting of only one species as e.g. shown by Pallarès and Johnsson [115].

In another study Fotovat et al. [110] performed radioactive particle tracking measurements in sand/biomass beds. Figure 3.6 shows the results for a biomass concentration of 2 wt.-% in a sand bed. On the abscissa the dimensionless distance ($r/R$) to the wall region ($r = R$) is shown. The biomass shows flotsam behavior and gathers at

the top of the bed. As stated above, in the core of the bed less biomass is present due to more bubbles in that region. The authors stated that for large biomass gasification or combustion reactors this effect is negligible since the ratio of the particle sizes and the bed diameter is much smaller for large vessels.
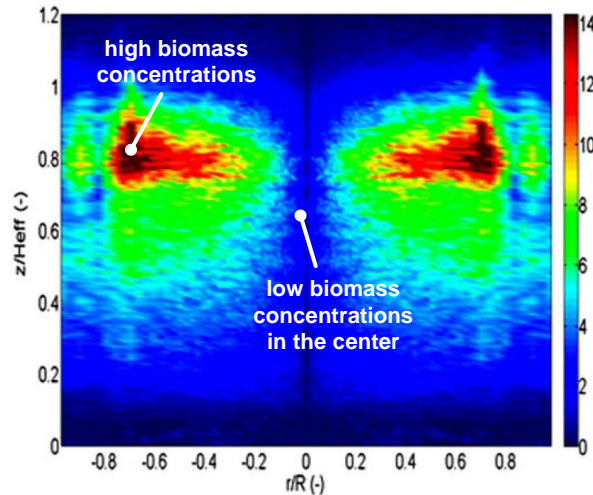


**Figure 3.6:** *Time-averaged concentration profile for a biomass/sand mixture containing 2 wt.-% of biomass in sand (Figure taken from Fotovat et al. [110]).*

### 3.2.3  Separation kinetics

**Time scales for separation**

In the introduction it was mentioned that in the steady state a dynamic equilibrium occurs. Starting from the initial condition the question arises how long it takes until the steady state is reached. Several authors investigated this topic with different mixtures [116, 91, 117, 118, 119, 120, 121, 122, 123, 124, 105, 125]. The time until this steady state is reached is referred to as $t_\infty$ in this study.

Generally, it can be concluded that the steady state is in most cases reached in 1 minute or less. The time needed, $t_\infty$, is dependent on the fluidization rate and the initial condition – but to a smaller extent.

Beeckmans et al. [117] investigated the displacement velocity, $u_d$, of HS/LB mixtures. They defined the displacement velocity by dividing the mean HS displacement by the time the bed was fluidized. A layer which consists of HS and LB was placed in a bed consisting of only LB particles. They found that $u_d$ increases the lower the initial layer is placed in the bed. Furthermore, $u_d$ decreases if the concentration of HS

in the layer is increased. The authors found that $u_d$ is in the range of 10 to 50 mm/s in all their experiments.

Early studies were conducted by Angelino et al. [116]. For various mixtures they give lengths of about 15 to 20 s until equilibrium is reached. Chiba et al. [118] investigated a HSF/LBP mixture and found that the equilibrium is reached within 30 s for all the cases. Furthermore, they found that $t_\infty$ depends on the initial concentration of the HSF particles. Yang and Keairns [91] stated that the dynamic equilibrium is established in less than 15 seconds in all experiments. Carsky et al. [119] found for a HSF/LBP mixture that the steady state was obtained after 45 to 90 seconds. Beeckmans et al. [120] found for a HS/LB mixture that steady state was reached after about 25 s. Hemati et al. [121] also stated that the equilibrium is established in less than 1 minute. For a HSF/LBP system investigated by Seo et al. [122] the steady state is reached after 60 to 90 seconds after starting fluidization.

Leaper et al. [124] investigated a HBP/LSF system and stated that the concentration and the height of the interface between the two species follow an exponential dependence until the steady state is reached: $dh_{bed}/dt = -\zeta_h(h_\infty - h_{bed})$. For their system they found that the equilibrium is established within 20 to 30 s. However, $\zeta_h$ is dependent on the fluidization velocity and the concentration of the HBP component, thus $\zeta_h = f(u_0, x_{HBP})$.

For wood/quartz sand mixtures, where the wood particles are considerably larger than the bed material (in the magnitude of $l_{p,biomass} \sim 100$ mm), Zhang et al. [105] found for all experiments that the steady state is reached in maximum 35 s or less. Shao et al. [125] also investigated systems with large particles compared to the bed material (wood and plastic in various shapes). They found that it always took less than 15 s to reach the equilibrium.

Yu et al. [123] investigated a HSF/LBF mixture and found that equilibrium is established after 10 min which is long compared to the other studies. The authors used large particles with diameters of the LB particles of about 20 to 40 mm.

**Influence of initial condition**

Carsky et al. [119] investigated the influence of the initial arrangement for a HSF/LBP system. They started from the total segregated state where once the HSF and once the LBP component is at the bottom of the bed. Due to their results the initial arrangement has no significant influence on the final concentration gradient in the bed. Beeckmans and Stahl [120] found for their HS/LB system that $t_\infty$ is lower if the fluidization is

started from the initially segregated state.

Zhang et al. [105] investigated wood/sand mixtures and three cases: complete segregation with biomass on the top, perfect mixing and complete segregation with biomass at the bottom. Since the last case has the largest deviation from the steady state profile it needs longer to come to the steady state. Also the time to reach the steady state decreases with the gas velocity.

## 3.2.4 Pressure profiles over the height of the bed

When a fluid flows through a bed of particulate matter two cases can be distinguished. The fixed bed occurs if $u_0 < u_F$. The pressure drop per height or the pressure gradient is proportional to the reverse quadratic particle diameter: $\nabla p \sim -\frac{1}{d_p^2}$ and shows a linear dependence of the fluidization velocity $u_0$ if $Re_p < 1$ since the quadratic term in velocity can be neglected. If the velocity is increased to $u_0 > u_P$ the complete bed is fluidized and the pressure drop depends upon the density of the bed: $\nabla p \sim -\rho_{bed}$ and remains constant for increasing $u_0$. $\rho_{bed}$ is the density of the bed which can be defined as a blend of gas and particle density as e.g. stated by Fan et al. [126]: $\rho_{bed} = \varepsilon_g \rho_g + \varepsilon_p \rho_p$.

Figure 3.7 shows the pressure profile over a binary mixture according to Chiba et al. [88] for fluidization velocities of $u_0 > u_P$. For perfectly mixed beds the pressure profile is linear over the height, Figure 3.7 (a). As mentioned earlier this case is unlikely to occur in beds consisting of dissimilar solids.

If a complete segregated bed is present two distinct layers form. The flotsam particles gather at the bed surface whereas the jetsam particles are located at the bottom of the bed. The distinct layer is also represented in the pressure profile. The pressure gradient in the bottom region is larger since the HEAVY particles are the jetsam particles in that case, Figure 3.7 (b) and therefore, the bed density is higher. The pressure gradient in the top region is smaller because of the LIGHT particles which act flotsam. In between a small transition region occurs.

The case of the partly mixed beds occurs between perfectly mixed an complete segregation. There forms a jetsam-rich layer in the bottom and a flotsam-rich zone at the top where these particles determine the pressure profile, Figure 3.7 (c). Furthermore, a much larger transition zone forms where the bubble wakes transport jetsam particles upwards towards the flotsam-rich top layer.

Olivieri et al. [97] investigated the pressure drop dependent on the superficial velocity in different heights of the beds for a HSF/LBP mixture. For the lower region
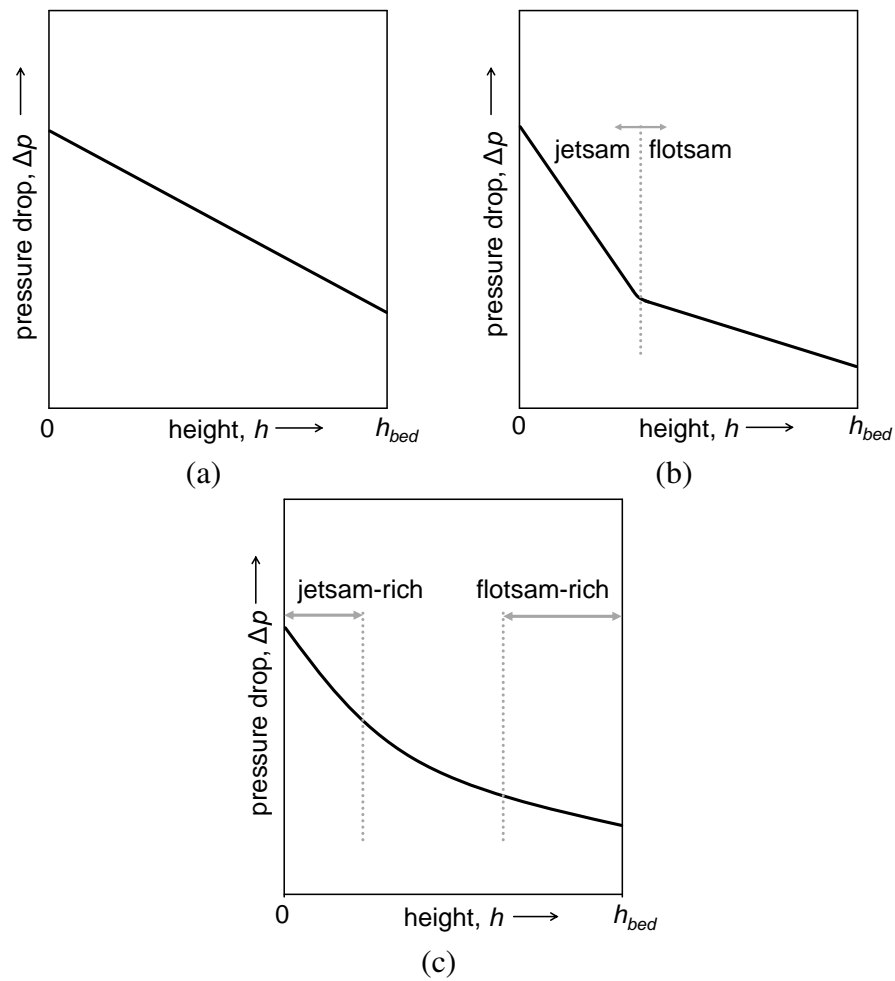
**Figure 3.7:** *Pressure drop over binary fluidized beds. (a) ... complete mixed bed, (b) ... complete segregated bed, (c) ... partly mixed bed (according to Chiba et al. [88]).*

of the bed they found that the pressure drop increases and comes then to the constant values, according to Figure 3.2 (c). However, for the pressure drop measured in greater heights of the bed the profile changes.

The authors distinguished various regions after the fixed bed region. First there occurs a relatively short region with constant pressure drop where the beds expands to a bubble-free regime. The velocity for that region is slightly below $u_F$. If the velocity is increased over $u_F$, the pressure drop decreases again in the higher regions of the bed since a flotsam layer forms. This happens in the transition region $u_F < u_0 < u_P$. Then, if the fluidization velocity is further increased also the pressure drop increases. At about $3u_P$ the pressure drop is constant in all the layers.

## 3.2.5  Bed expansion

If the fluidization velocity is increased also the bubble volume and the gas hold-up in the bed increase. Therefore, the bed expands more and the bed height increases. A common way to measure the bed expansion is either the pressure drop or a visual observation. Normalizing the measured bed height to the one at minimum fluidization conditions, $h_{bed}/h_{mf}$ is a common way to depict the results.

Chiba et al. [88] performed measurements on that. They investigated a HSF/LBP mixture and found a steep increase in bed expansion if the fluidization velocity exceeds $u_F$. After the transition region between $u_F$ and $u_P$ the bed expansions also increases but to a much smaller extent.

Fotovat et al. [100] investigated the influence of the loading of biomass cylinders on the bed expansion with sand as bed material. If the biomass loading was increased the authors found a decreasing bed expansion. As large particles are able to decrease the bubble size, the gas is more uniformly distributed throughout the bed and therefore the bed expansion also decreases.

## 3.3  Axial mixing processes

Section 3.2.2 focused on the general mechanisms on mixing in binary fluidized beds of dissimilar solids. In this section a discussion on the special aspect of axial mixing is given.

Axial mixing depends upon various variables:

- solid densities, $\rho_p$

- particle diameter, $d_p$

- particle shape, $\phi_p$

- bed mixture composition, $x$

- superficial velocity, $u_0$

- bed geometry: aspect ratio, cross section area

Mixing behavior is strongly influenced by the size and density ratio of the particle species in the bed. Therefore, the size ratio is defined as the ratio of the mean diameter

of the BIG to the SMALL particles:

$$SR = \frac{d_{p,BIG}}{d_{p,SMALL}} \tag{3.2}$$

and the density ratio in the same way as:

$$DR = \frac{\rho_{p,BIG}}{\rho_{p,SMALL}} \tag{3.3}$$

Although axial mixing processes got the most attention in literature some authors conducted experiments to investigate radial or azimuthal segregation patterns. Joseph et al. [127] found no azimuthal segregation and only low radial segregation dependent on fluidization velocity.

### 3.3.1 Size ratio, $SR$

The size ratio $SR$ of the particles has a great influence on mixing behavior. In binary fluidized beds there are two ways to influence the size ratio, $SR$: by varying the size of the SMALL or the BIG particles and keeping the other one constant.

Many authors conducted studies with biomass since it is of high practical relevance. Biomass is often used as fuel in combustion or gasification plants. Biomass is in most cases the lighter and also the bigger component.

The majority of the following results imply that if $SR \rightarrow 1$ the mixing improves for either constant diameter of the SMALL or BIG particles. However, results from some authors are somewhat contradictory, so some other factors occur which might have influence.

**Size of SMALL particles varied**

Bilbao et al. [128] investigated mixtures of straw and sand. They found that the smaller the particle sizes of sand get, the more uniform are the axial concentration profiles. For coarse sand particles segregation occurs.

Seo et al. [122] investigated resin beads/sand mixtures and found better mixing if the size of the sand is decreased. Fang et al. [129] investigated silicon sand/rice husk mixtures and also report that mixing gets better or concentration gradients become more even over the height if the size of the sand particles is decreased.

Qiaoqun et al. [130] investigated rice husk/sand mixtures. They reported that an increase of the size of the sand particles leads to an increase of the mass fraction of the

rice husk in the upper section of the bed.

Sun et al. [131] investigated mixtures of alumina and cotton stalk. They also found for cotton stalk sizes up to 70 mm that smaller diameters of the alumina favors mixing of the particles. However, if the sizes of the cotton stalk are increased even more to sizes up to 100 mm, an opposite trend occurs and the mixing is the best for the largest alumina particles.

Renzo et al. [87] investigated mixtures which consist of olive pits and sand. For small mass fractions of the sand particles ($x_{sand} < 0.2$) mixing gets qualitatively better if the size of the sand is increased. For the case of high sand mass fractions ($x_{sand} > 0.7$) no clear trend can be seen. It should be kept in mind that the authors used different superficial velocities for the experiments. For each mixture they fluidize until the mixture is in a well-fluidized state. Since diameters and mass fractions are varied also this velocity varies. Therefore, the comparison of the results regarding influence of the particle diameter is not entirely comparable to the results further above.

From these results it can be concluded that generally larger diameters of the SMALL bed material leads to worse mixing. However, as Sun et al. [131] showed there may be exceptions to that.

**Size of BIG particles varied**

Many experiments have been conducted with biomasses. Bilbao et al. [128] investigate mixtures of straw and sand. They found that the smaller the particle sizes of straw get the more uniform are the axial profiles are.

Xiaodong et al. [132] investigate mixtures of municipal solid waste (MSW) in a sand fluidized bed. They found that for wood particles the mixing gets more uniform with increasing particle size and that the wood particles tend to sink in the bed.

As mentioned in the previous section Sun et al. [131] investigated mixtures of cotton stalk and alumina. If the size of the cotton stalk is increased for small diameters of the alumina the mixing gets worse. However, for larger alumina sizes mixing improves with increasing size of cotton stalk.

Cluet et al. [133] investigated wood/olivine mixtures and found that mixing improves if smaller sizes of wood is used. Yu et al. [123] investigated a mixture of nylon and sand and found a decrease in mixing quality if the length of the nylon particles is increased.

Some authors also conducted experiments where coal was used. Hemati et al. [121]

reported that the size of the coal hardly influences the mixing behavior. However, they used short fluidization times of 1 min which could be too short since the used time is approximately the time for steady state, see section 3.2.3. Xiaodong et al. [132] found that mixing gets worse with increasing size of the coal particles. Wang et al. [134] kept the diameter of the bed material constant and found that an decreasing size of the coal ($DR$ is nearly the same for all investigated coal diameters) leads to a better mixing.

For heavier components similar results can be found. Xiaodong et al. [132] found that increasing the size of coal stone particles mixing gets worse. Similar results are reported by Wang et al. [134] who investigated beds with gangue.

Generally, if the size of large particles decreases the mixing gets better which is a similar result as found in the previous section.

### 3.3.2 Density ratio, $DR$

As already mentioned density has more influence on segregation than particle diameter [13]. The more different the densities of the particle species, the more segregation occurs [84, 132]. Generally, the denser particle species behaves jetsam [85]. However, in special cases this rule does not apply as it was shown [85, 87] – the denser component can also act flotsam.

There are also two possibilities to change the density ratio, by either increasing or decreasing the density of the SMALL and/or of the BIG particles.

From the following results no general statement can be drawn. Some authors report that mass fraction profiles get more uniform if the densities of the SMALL and BIG particles approach to each other [135, 125]. Other authors report that density has no influence at higher velocities [123, 133].

It was also reported that the tendency of the BIG particles for flotsam behavior increases if the density of the bed material is increased [132]. It was also seen that at low velocities a reduction in the density ratio between wood and olivine particles improves mixing. At higher velocities this effect is not visible any more [133].

**Density of SMALL particles varied**

Nienow et al. [135] investigated beds consisting of ballotini and sand as the HS component and char as the LB component. The authors found that if the density of the HS is decreased ($DR \rightarrow 1$), the mass fraction profile across the bed becomes qualitatively more uniform. However, this effect decreases with increasing velocity.

Xiaodong et al. [132] investigated beds of sand or coal as SMALL and typical particles contained in municipal solid waste (MSW): wood, candle, plastic and coal stone. They showed if the density of the SMALL particles is increased all the investigated MSW particles showed more flotsam behavior or at least the tendency to not move entirely to the bottom of the bed as it was the case for coal stone.

**Density of BIG particles varied**

Nienow et al. [136] investigated BIG and LIGHT flat particles of different density in a bed of HEAVY alumina particles. The authors described that for low velocities the HEAVY particles sink more, at higher velocities both LIGHT and HEAVY do.

Yu et al. [123] investigated beds of sand with cylindrical particles of wood, polyethylene, nylon and polyamide. For the smallest LIGHT particles (wood) they found a strongly flotsam behavior for low velocities, higher velocities give an even profile. Polyethylene and nylon show flotsam behavior although velocity has not that much influence like in the case for wood. For polyamide, which is the most HEAVY one they found that it acts strongly jetsam for low velocities and mixing increases which increasing velocity which results in a more even mass fraction profile. They found for velocities $FN = 3.0$ that density has no influence on mixing.

Cluet et al. [133] found that the influence of the fluidization velocity is also dependent on the density of the BIG particles. For low velocities (FN = 2.15) they found that beech wood (heavier) is better mixed than balsa wood (lighter). So, for low velocities the density has an effect on mixing. For higher velocities ($FN = 3.35$) they found that there is no difference between beech and balsa wood and concluded that there is less density influence or even none.

Shao et al. [125] investigated three different particle species of cylindrical shape: wood, plastic and metal in a sand bed. The wood particles behave flotsam since the density is lower than that of the bed material. The mixing gets better for $DR \rightarrow 1$, therefore mixing improves for plastic cylinders. Further increase of the density for the metal sticks leads to nearly complete segregation and sinking of the metal sticks to the bottom.

## 3.3.3 Fluidization velocity

Fluidization velocity is the aspect which is the most investigated one in the fluidization of dissimilar solids. Fluidization velocity can be varied in a broad range and goes through two different particle regimes: fixed bed and fluidized bed.

Occurring effects when increasing the superficial velocity have been discussed in section 3.2.2. Higher fluidization velocities cause more bubbles and hence a higher fluidization velocity causes better mixing since the jetsam particles penetrate more into the bed and mass fraction gradients become smaller with increasing fluidization velocity. This is reported by all conducted studies where the SMALL particles are also the HEAVY ones either for spherical particles [104, 137, 119, 138, 97, 127] or irregular shaped particles [135, 136, 128, 121, 122, 139, 123, 105, 106, 107, 131, 140, 133, 125]. In recent years the focus has shifted from spherical to irregular shaped particles as the LARGE particles.

Olivieri et al. [97] investigated mixtures consisting of silica sand as HSF and silica gel as LBP particles. They investigated the mass fraction profiles over the bed height dependent on the fluidization velocity. The mass fraction of the HSF was chosen to $x_{HSF} = 0.2$. The experiment was started from the ideally mixed state. They found for $u_0 \approx u_F$ that the bed remains ideal mixed. By increasing the velocity to $u_0 \approx u_P$ strong segregation occurred. By further increasing the fluidization velocity, $u_0 >> u_P$, mixing is improving again and the mass fraction profile is getting more uniform.

Zhang et al. [106] found similar trends also for sand beds with large biomass cylinders. The authors started at the well mixed state and measured the axial mass fraction profile for increasing velocities. They found that the more the velocity approaches $u_{cf}$ the mixing gets worse and is the worst at $u_0 = u_{cf}$. Park and Choi [140] report also sinking mixing quality starting at $u_0/u_{mf} = 1$ until $\approx 1.15$. After that the mixing quality improves again, Figure 3.8.



| $u_0/u_{mf} = 1.00$ | $u_0/u_{mf} = 1.07$ | $u_0/u_{mf} = 1.14$ | $u_0/u_{mf} = 1.35$ |
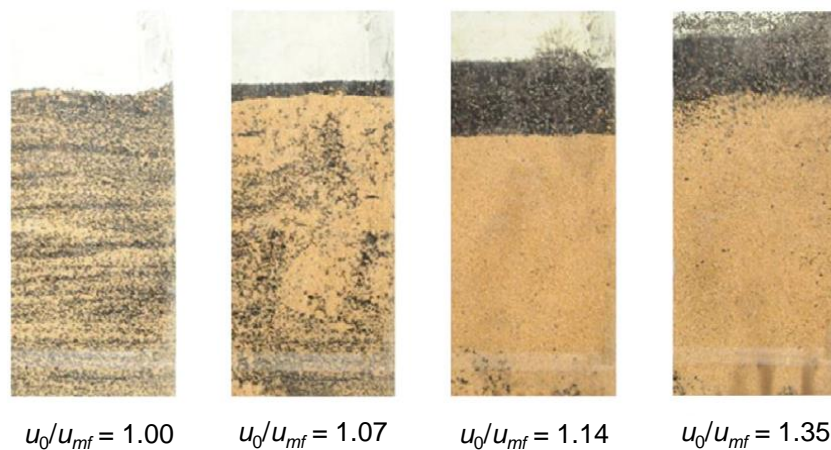
**Figure 3.8:** *Mixing behavior starting from the fixed bed condition (picture taken from Park and Choi [140].*

Carsky et al. [119] stated that in the region around $u_{MS}$ the highest segregation

occurs. Hemati et al. [121] stated that there is strong segregation if $u_0 < 2.5u_F$ for sawdust/sand mixtures. For $u_0 > 2.5u_F$ they found improved mixing. For a coal/sand mixture the same authors found that good mixing is obtained for $u_0 > 2u_F$.

Similar results are also provided by Nienow et al. [135] for a coal/sand system. For anion resins and glass beads Seo et al. [122] found also similar results and a strong segregation below about $u_0 < 1.5u_F$. Mourad et al. [139] found good mixing for mais/sand mixtures if $u_0 > 3.5u_F$.

If consequently the fluidization velocity is increased also the mixing becomes better because of the aforementioned reasons. Nienow et al. [104], Carsky et al. [119] or Hoffmann et al. [138] showed that for HSF/LBP mixtures. Naimer et al. [137] investigated a HS/LB system and also strong segregating HBP/LSF system the mixing quality was improved through higher velocities.

Nienow et al. [135] investigated systems with large char particles of 5 mm diameter and found more uniform mass fraction profiles over the height with increasing velocity. Experiments with biomass (straw [128], mais [139], wood [141, 133]) showed the same result. Yu et al. [123] investigated mixtures of sand as HS particles and wood, polyethylene, nylon and polyacetal as LIGHT and BIG particles. The authors found that increasing superficial velocity leads to better mixing and more uniform mass fraction profiles.

For large biomass cylinders Zhang et al. [105] found that the mixing gets better with higher velocities. The authors found that the time which it takes to come from the initial to the steady state decreases with velocity. Therefore, also the mixing kinetics are accelerated if the velocity is increased. However, with even higher velocities ($u_0/u_{mf,sand} > 6$) mixing is getting worse and the mass fraction of biomass in the top layer is increasing again making a U-shaped curve of the mass fraction of the top layer for velocities ($1 < u_0/u_{mf,sand} < 10$). If these results are analyzed with a mixing index (where $M = 1$ means ideal mixing and $M = 0$ perfect segregation), a distinct maximum can be observed [107]. This can also be seen schematically in Figure 3.9.

Nienow et al. [136] also found worse mixing for high velocities. They argued that at these velocities the LIGHT particles are more easily lifted upwards and gather at the top of the bed. For cotton stalk Sun et al. [131] also found a slightly decreasing mixing quality with increasing superficial velocity. The authors concluded that at high fluidization rates ($u_0/u_{mf} > 3$) more light cotton stalk is blown into the dilute phase, therefore, more cotton stalk is gathering at the top of the bed and mixing decreases again.
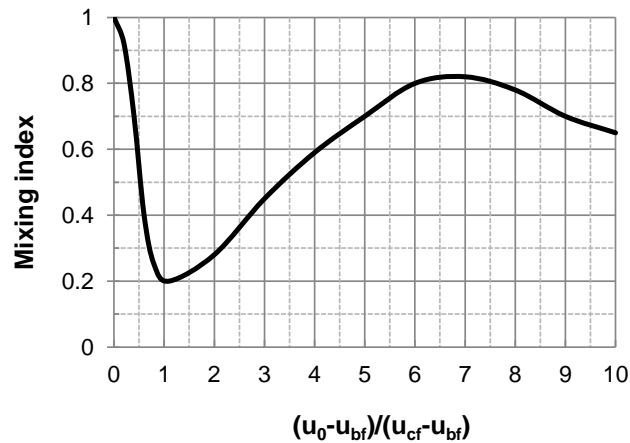
**Figure 3.9:** *Variation of the mixing index with the fluidization velocity for large biomass cylinders (according to [106]).*

### 3.3.4 Mass fraction

If the HEAVY particles are also the BIG particles they behave jetsam. However, in the case where the HEAVY particles are also the SMALL particles it can occur for sufficiently small HS mass fractions that these particles start to behave flotsam [85, 87]. Furthermore, higher mass fractions of HS particles in the bed enhance mixing processes [137, 97, 128]. For low mass fractions of the LB particles also no influence [121] or a contrary result [122] was found.

Chiba et al. [85] investigated a system consisting of hollow char/glass beads. They found that a very low mass fraction of HEAVY particles leads to a flotsam tendency if the size ratio is sufficiently small and if low fluidization velocities are present. If $x_{HEAVY} < 0.3$ the HEAVY component acts flotsam. After a transition range they concluded that the HEAVY becomes jetsam if the mass fraction is $x_{HEAVY} > 0.7$. They explained that with the ability of the small particles to pass through the voids formed by the larger particles. However, the authors only used superficial velocities in the range of $u_F \leq u_0 \leq u_P$. The phenomena are found for both defluidization processes.

Renzo et al. [87] investigated mixtures of glass beads and sand granules, respectively, and olive pits. For high mass fraction of the HEAVY particles they behave jetsam which is in accordance to the findings by Chiba et al. [85]. With increasing mass fraction of the LIGHT particles they behave jetsam. This is dependent on the size ratio. The smaller the HEAVY particles are the higher the mass fraction of the HEAVY can be to obtain this inversion phenomenon.

Naimer et al. [137] used a bed consisting of copper shot/ballotini (HS/LB) and found strong segregation for different jetsam mass fractions. For larger mass fractions of the HS a larger transition zone between the flotsam and jetsam particles forms.

Olivieri et al. [97] investigated the mixing index for various mass fractions of the HSF particles and found that the velocity to obtain $M > 0.9$ is strongly dependent on the composition of the mixture. If the mass fraction of the HSF particles is increased the velocity to obtain high mixing indices decreases.

For velocities $u_0 = 2.2u_{cf}$ Joseph et al. [127] found also better mixing for higher fractions of HS particles. For lower velocities ($u_0 = 1.2u_{cf}$) the authors found a strong segregation profile for systems with low HS content and report that a layer of jetsam at the bottom formed with uniform composition. Increasing the HS content the profile approaches a linear form.

For sand/straw systems Bilbao et al. [128] found that higher sand mass fractions in the bed improved mixing. However, Seo et al. [122] used mass fractions of resin of 15 and 30 wt.-% in a sand fluidized bed and found that increasing the mass fraction of the resin leads to an increase of the mixing index and therefore better mixing. For coal Hemati et al. [121] did not find a dependence of the mass fraction of coal between 7 to 14 wt.-%.

According to the results of Zhang et al. [106] the axial profile is similar for mass fractions of cotton stalk cylinders between 1 to 3 wt.-%. However, the characteristic maximum of the mixing index dependent on the velocity (as seen in section 3.3.3) is moved to higher velocities if the mass fraction of the cotton stalk cylinders is increased.

### 3.3.5 Particle shape

Some authors also investigated the influence of the shape of the particles [136, 133, 111, 125]. This is done especially for different plastics or wood particles. The following results summarize the findings.

Cluet et al. [133] reported that wood chips tendentially mix better than wood dowels. The authors explain that with the shape of the chips since it allows the chips to come to a vertical position and sink into the bed.

Fotovat et al. [111] found a similar axial distribution of cylindrical and spherical particles especially for low biomass loadings of around 2 wt.-%. For a rising biomass loading they observed that cylindrical particles have a stronger tendency to move to the top of the bed. Similar results were obtained by Shao et al. [125]. They also found that plastic cubes and spheres have no significant difference in their mixing behavior.

Nienow and Cheesman [136] investigated the fluidization behavior of large flat particles of low weight. They reported that these flat particles mix better than spherical ones and that flat particles and spheres show similar mixing behavior at high fluidization velocities and tended to a flotsam behavior. However, at low velocities flat particles which were placed at the top of the bed remained there but also sank to the bottom and therefore showed jetsam behavior. The authors stated that this is due to an overlayer of bed material at the top and when they are at the bottom they remain there.

### 3.3.6 Bed geometry

Higher beds could mean bigger bubbles and since bubbles are the cause for mixing processes higher beds should give better mixing from that point of view. Nienow et al. [104] investigated the mixing index with the height as parameter and found better mixing with increasing bed height. However, Carsky et al. [119] as well as Cluet et al. [133] found no dependence of mixing with respect to bed height.

Park and Choi [140] investigated the influence of the geometry of the cross section area: circular, square and rectangular. In all experiments the square cross section obtained the best mixing (although strong segregation was present, for square it was the least).

## 3.4  Mixing in circulating fluidized ed devices

Mixing and segregation of circulating fluidized bed systems is also carried out by some authors [142, 20, 143, 144, 145, 146]. This includes all systems where a bed material is circulating like riser/loop seal combinations as well as systems where a e.g. bubbling and a fast fluidized bed are coupled.

Nakagawa et al. [142] investigated the segregation profile over the height of a riser and used FCC particles as HSF particles and silica sand and activated alumina, respectively, as LBP particles. Using a particle reservoir and a U-shaped loop seal they were able to control the solids recirculation rate in a small range independent from the fluidization rate of the riser.

For the case where $u_0$ in the riser is below the terminal velocity of the LBP particles strong segregation occurs. However, if the solids recirculation rate is increased nearly a uniform profile along the height can be obtained. They argue that the force exerted from the HSF particles is increased with increasing solids recirculation rate which results in better mixing along the height. This also shows that heavy particles can be

transported upwards although its terminal velocity is not exceeded.

If $u_0$ is higher than the terminal velocity of the LBP particles the authors measured a uniform mass fraction profile. This also caused high solids recirculation rates which then lead to more force exerted from the HSF particles and drag the LBP particles more easily upwards.

Alghamdi et al. [144] investigated a cold flow model of a 10-kW-CLC plant. The investigated mixtures of glass beads (HSF) and polyethylene (LBP). Similar to Nakagawa et al. [142], they also found that mixing gradually gets better with higher superficial velocities in the riser. For their configuration they recommend to use values of $u_{0,riser}/u_{t,HEAVY} > 1.25$ to obtain good mixing and no segregation between the two reactors.

Bidwe et al. [145] performed segregation experiments in a cold flow model which was operated in a bubbling bed regime. The cold flow model had a drain at the bottom where particles could be removed from the bed. Furthermore, a solids supply at the top of the bed was installed. The authors used steel powder as HSF particles and limestone as LBP particles. With that configuration they aimed to model a sand/biomass system.

In their experiments they found that although the bed material drain at the bottom the limestone particles have a tendency to move to the top of the bed and show flotsam behavior. After the experiments the authors found higher LBP mass fractions at the end of the experiment than the initial mass fraction. An accumulation occurred.

Lim [143] and Bosch [20] investigated cold flow models of a DFB steam gasification system. They investigated the influence of scaled biomass loadings on the bed material recirculation rate and pressure drops. However, they performed no experiments regarding mixing.

## 3.5  Summary and conclusion

In this chapter the experimental evidence of the last decades regarding the binary fluidization of dissimilar solids were reviewed. Regarding mixing three cases can be distinguished: perfect mixing, complete segregation and partial mixing, which is the most common if beds consisting of dissimilar particle species are present.

In beds of dissimilar solids an equilibrium occurs between mixing and segregation processes. The mixing process is determined by gas bubble movements. The bubble drags a wake behind which is filled up with particles. Further mixing mechanisms are the inter-particle perculation of larger particles to the surface and also a quasi-hydrostatic effect which causes lighter and bigger particles to float on the surface.

The time until the steady state or the equilibrium between mixing and segregation processes is obtained is given by most authors of about 1 min or less. The initial mixed or segregated condition of the bed seems to have an influence on this time.

The minimum fluidization velocity is also of importance for binary mixtures of dissimilar particles. However, there are more characteristic velocities for binary beds than it is the case for beds containing only one particle species. Additionally to a minimum fluidization velocity, other velocities can be defined, where the fluidization process starts and ends, $u_{bf}$ and $u_{cf}$, or where the first bubbles arise, $u_{ib}$.

However, the minimum fluidization velocity depends greatly on the measuring method. The fast defluidization process favors mixing and gives therefore higher minimum fluidization velocities. Even if the bed is fluidized and then slowly defluidized different results for the minimum fluidization velocity occur.

Furthermore, the minimum fluidization velocity increases with the content of biomass particles in the system and also with higher diameters of the bed material and biomass particles. Similar results are also found for the complete fluidization velocity, $u_{cf}$. A lot of correlations to calculate the minimum fluidization velocity of binary mixtures as well as the complete fluidization velocity were developed by many authors.

The axial mass fraction profile is influenced by various parameters:

- particle diameter, $d_p$

- solid densities, $\rho_o$

- particle shape, $\varphi_p$

- mass fraction, $x$

- fluidization rate, $u_0$

- bed geometry: aspect ratio, cross section area

Many studies showed that smaller particle sizes of either the HEAVY or LIGHT particles favor mixing. The density is reported to have a major influence on the mixing processes. The higher the density difference between the particles is the more segregation occurs.

The higher the fluidization velocity the more bubbles penetrate into the bed. Therefore, more jetsam material is carried upwards in the bed and mixing is improved. However, it was found that mixing could worsen for very high velocities. In beds consisting of sand and biomass it was found that the bubble size decreases if the biomass content is increased.

Regarding particle shape cylinders are supposed to segregate more than chips and spheres. Furthermore, higher beds are supposed to show better mixing behavior.

Although many experiments were conducted the number of parameters and possible combinations are huge. Therefore, some evidence is clear for some parameter variations contradictory results are shown. More experiments on that are necessary to bring light in all the dark fields of the fluidization of dissimilar solids.

# 4 Simulation of dual fluidized bed processes with Barracuda

In this chapter the modeling and simulation of DFB systems with Barracuda is carried out. Data was used from a cold flow model of a scale of 1:4 of the commercial plant and also of the commercial plant itself.

First, the focus was on the hydrodynamics and, therefore, the cold flow model of the Güssing reactor was simulated. Since the drag law has a massive influence on the results, four relevant drag laws were used and the bed material recirculation rate, pressure drops and pressure profiles were calculated and compared to experimental results.

Based on these simulations the commercial DFB system in Güssing was modeled. In that model all relevant boundary conditions were implemented to obtain a representation as close as possible to the commercial plant. That means that not only the inlet flows were considered but also recycled streams. Furthermore, chemical reactions and heat transfer processes were included.

For the simulations Barracuda V17 was used. The hardware infrastructure was a workstation with an Intel Core i5-3570 and 16 GB RAM. Since Barracuda V17 supports a GPU acceleration the workstation was also supplied with a graphics card of the type GeForce TITAN X.

For the cold flow model and the commercial plant, respectively, first the model setup is described. Afterwards the simulation results and the comparison to measurement are provided and the results are discussed.

## 4.1 Literature review

In this section relevant studies published so far with Barracuda are shortly reviewed and discussed. Therefore, two sections are presented, one which focuses on studies where Barracuda was used to simulate cold flow models and one where Barracuda is used for the simulation of hot biomass gasification and for combustion reactors.

## 4.1.1 Studies conducted in cold flow models

Barracuda was used in many studies to investigate the flow behavior inside cold flow models of fluidized beds. Investigations of the influence of the solid pressure and restitution coefficient on bed hydrodynamics were carried out by Lim et al. [147]. Further studies dealt with bubbling beds [148, 149, 150], spouting beds [151], internally circulating fluidized beds [152] and risers [153, 154, 155, 156, 157, 158]. Qiu et al. [159] simulated a part of an circulating fluidized bed combustor [159]. Full loops of circulating fluidized bed models were investigated by Clark et al. [160], Wang et al. [161, 162] and Hamilton et al. [163].

A full bench scale unit for carbon capture applications was simulated by Clark et al. [160]. The unit consists of two fluidized beds (one bubbling, one fast), two loop seals, a riser and a cyclone. The simulation predicts measured pressure drops with reasonable accuracy. Bed material circulation rates were not measured by the authors. Therefore, a comparison with the simulated values of the circulation rates cannot be done.

A setup consisting of a fast fluidized bed, cyclone and U-type loop seal was simulated by Wang et al. [161]. They investigated the hydrodynamics inside the reactor and used the following drag laws: Wen-Yu/Ergun, Wen-Yu and Ganser. For the Wen-Yu/Ergun drag law they used two different configurations: One with the default parameters implemented in Barracuda and one with the standard parameters. They calculated bed material recirculation rates and pressure drops over the riser and compared the simulation results to the experimentally obtained values. They found out that the Wen-Yu drag model predicted best the bed material recirculation rate. On the other hand the Wen-Yu/Ergun drag model with the standard parameters gave the best predictions for the total pressure drop. A follow-up work was carried out by the same authors [162] to investigate the influence of the flow rate in the riser and the loop seal as well as the total bed inventory on the recirculation rate. Simulation results showed a reasonable agreement with the experimentally found values. Furthermore, the trends of the curves were predicted correctly.

Hamilton et al. [163] investigated two configurations of a chemical looping process. The authors compared a dual bubbling bed (BB) and a dual circulating fluidized bed (CFB). The drag model by Wen-Yu was used. The dependence of the fluidization rate in the air reactor on the total solid recirculation rate was investigated experimentally. No pressure measurements were carried out. The simulation overpredicted the recirculation rates in the dual CFB system but it gave good predictions of the trends. The simulation failed to predict the dependence for the dual BB configurations.

## 4.1.2 Studies conducted for hot biomass gasification and/or combustion plants

Barracuda was also used for the simulation of hot industrial systems, such as FCC regenerators [164], fluidized bed classifiers [165], coal gasifiers [78], chemical looping combustors [166], and CFB combustors [167, 168, 169].

Some studies were carried out where biomass combustors were simulated. Weng and Omer [170] investigated three different circulating fluidized bed combusters located in Germany and Poland. As fuels either biomass or coal/biomass mixtures were used. The simulations were used to investigate erosion behavior, temperatures as well as the distribution of gas species inside the system. Via the simulations it was possible to reduce erosion behavior leading to a more stable process operation.

Kraft et al. [146] simulated a bubbling fluidized bed boiler which is fired with biomass. The reactor suffered from severe ash deposit build-up which negatively influenced the fluidization behavior. The simulation showed that with the current operation mode large zones occur which exceeded the ash melting temperature. Therefore, three different operation points were tested with different air staging between primary and secondary air. Doing so the zones of high temperatures could be significantly reduced resulting in lower probability for ash deposit build-up.

More relevant for the present work are studies where biomass gasification was simulated with Barracuda as done by several authors. The devolatilization of the biomass particles is often assumed to occur instantaneously. This assumption can be questioned since the release of the volatiles produces a considerable amount of gas which can have a significant influence on bed hydrodynamics and can also influence the rising movement of the fuel particles as shown by some authors [18, 19].

Thapa et al. [171] investigated the gasification reactor of a DFB system. The inlet and outlet of the bed material recirculation were modeled with an inlet and outlet boundary condition. The gasification reactor is of cylindrical shape, olivine is used as bed material and wood chips as fuel. No dimensions of the reactors are provided by the authors. The fuel feed rate is set to 28 kg/h, which equals approximately 100 kW$_{th}$. The authors calculated and analyzed gas and particle temperatures, product gas composition and the distribution of different gas species within the reactor. However, no experimental data is provided and the simulation is not validated.

In a similar study Thapa and Halvorsen [172] used Barracuda to investigate the gasification reactor of a DFB system. Similar to Thapa et al. [171] the bed material recirculation is modeled with inlet and outlet boundary conditions in the gasification

reactor. The reactor is 2 m high and has a diameter of 0.55 m. As bed material they used olivine. Wood was used as fuel with a feeding rate of 450 kg/h, which is about 1.6 $MW_{th}$. The authors investigated the influence of various parameters on the product gas total energy. The varied parameters are the bed material recirculation rate, the bed material temperature, the flow rate and temperature of the steam. However, the authors do not present a validation of their model.

Loha et al. [173] investigated a cylindrical bubbling bed gasifier in laboratory scale with a diameter of 0.05 m and a total height of 0.5 m. Rice husk is used as fuel and the authors assume that the devolatilization is instantaneous and completed at the inlet of the feeding position. They compared the simulated and measured gas composition for various operating points and found good agreement. Based on this, they simulated the particle volume fractions inside the reactor and the distribution of the gas species within the system.

Liu et al. [51, 174, 175] investigated a dual fluidized bed biomass gasification system with a full load of 1 $MW_{th}$. It consists of a gasification reactor, a combustion reactor, a cyclone, and a loop seal. The gasification reactor is fluidized with steam and almond prunings were used as feedstock. They modeled the devolatilization with a single step global model for drying and release of volatiles. As reaction kinetics an Arrhenius approach was used.

In a first study [51] they investigated the distribution of product gas species inside the gasification reactor. Similar investigations were done in a follow-up study [175]. They found good agreement between the simulated and measured product gas compositions. Temperatures are predicted with deviations of up to 65 K in the gasification reactor and 35 K in the combustion reactor. Further investigations regarding temperatures are carried out [175]. In a further study [174] they investigated the influence of various parameters on the solid circulation rate. The parameters were the particle diameter of the bed material, solid inventory, air staging in the combustion reactor and steam supply to the gasifier. They found the recirculation rate to decrease with increasing particle diameter and an increasing circulation rate with increasing solids inventory. If more air is fed into the combustion reactor (either at the bottom or at primary or secondary air) the recirculation rate is increased.

## 4.2 Modeling of the Güssing cold flow model

In this section the modeling of the Güssing cold flow model is presented. This includes the description of the used geometry including boundary and initial conditions.

Furthermore, relevant simulation parameters are given.

## 4.2.1 Cold flow model of the DFB system in Güssing, Austria

The cold flow model of the Güssing DFB system was scaled according to the full set by Glicksman [65]. Based on that a scale for the cold flow model of 1:4 results compared to the commercial plant since the usage of the full set assigns fixed scale factors for geometry as stated in section 2.3.2. As the commercial plant the cold flow model consists of a gasification reactor, chute, combustion reactor, cyclone, and loop seal. The total height of the cold flow model is 2.3 m, the diameter of the freeboard in the gasification reactor is 0.5 m. The cold flow model is constructed with acrylic glass. Air is used as gasification agent at ambient conditions.

To fulfill the scaling criteria a heavy bed material has to be used, in the present case this was bronze with a mean diameter of $d_p = 118$ $\mu$m and a density of 8730 kg/m$^3$. In Figure 4.1 the particle size distribution of the used bed material is depicted.
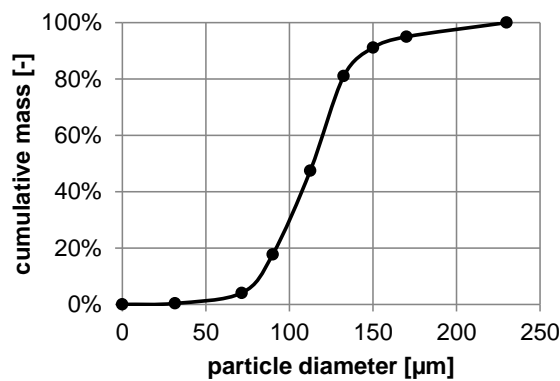


**Figure 4.1:** *Particle size distribution of the used bronze powder.*

**Circulation rate measurements**

During operation the fluidization air of the loop seal was closed abruptly. The bed material through-flow is then stopped and the bed material accumulates in the downpipe of the cyclone. The increase in the height of the bed material in a certain time can then be correlated with the bed material recirculation rate which can be calculated as follows:

$$\dot{m}_{rec} = \rho_{p,bulk} \frac{\Delta h_{bed}}{\Delta t} A_{ls}. \tag{4.1}$$

**Pressure measurements**

The pressure was measured in the following positions:

- **Gasification reactor (2):** directly above the bottom gas distributor and at the gas exit;

- **Riserv (4):** directly above the bottom gas distributor, in the middle, between middle and top, at the top;

- **Loop seal (2):** at the lowest position of the two legs of the loop seal.

The number in the brackets indicates the number of pressure measurement positions.

The loop seal is of an U-shape and consists of two legs. One leg is coming from the cyclone and is called the "down" leg. The other one which is connected to the gasification reactor is called the "up" leg, Figure 4.2.
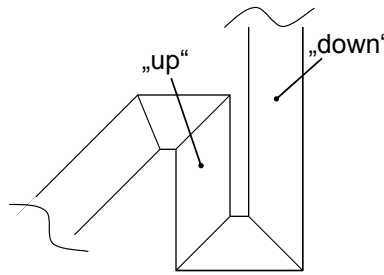


**Figure 4.2:** *Schematic view of the loop seal of the cold flow model and the labels of the "up" and "down" leg, respectively.*

More Details on the configuration of the cold flow model can be found in [20].

## 4.2.2 Simulation setup

**Geometry**

The geometry was drawn according to drawings of the cold flow model also given in Bosch [20]. A mesh size with 152,968 computational cells was used, which corresponds to side-lengths of the control volumes of about $1.5 \times 1.5 \times 1.5$ cm$^3$. For the present study, 796,182 computational particles were used. With the computational hardware used it took about 0.5 hours to simulate 1 second. An analysis of the influence of the mesh size on the results showed that the used mesh is fine enough.

**Initial and Boundary conditions**

As initial condition the system was filled with air at ambient conditions at 298 K. As in the experiments the simulation geometry was filled with 130 kg of bed material. Simulation parameters are shown in Table 4.1. For the simulations also the particle size distribution used in the experiments, according to Figure 4.1, was implemented.

**Table 4.1:** *Properties for gas and particle species used in the Barracuda simulations.*

| parameter | value | dimension |
|-----------|-------|-----------|
| $\rho_p$ | 8730 | kg/m$^3$ |
| $\rho_{p,bulk}$ | 5300 | kg/m$^3$ |
| $d_p$ | 118 | $\mu$m |
| $\phi_p$ | 1 | [–] |
| $m_{bed}$ | 130 | kg |
| $\rho_g$ | 1.169 | kg/m$^3$ |
| $\mu_g$ | $1.82 \cdot 10^{-5}$ | kg/(m s) |
| $T$ | 298 | K |
| $p$ | 101325 | Pa |

The boundary conditions for the simulations were set according to the experiments. The positions are shown in Figure 4.3. Flow inlet conditions were implemented for the bottom of each the gasification reactor, the combustion reactor and the loop seal. Primary and secondary air inlets were specified as "Injection Boundary Conditions" in Barracuda. These special boundary conditions simulate a pointwise injection of the inflow into the geometry. As gas species air was used. Two pressure boundary conditions were used, one at the outlet of the gasification reactor and one at the outlet of the cyclone.

In the experiments the primary and secondary air is introduced via nozzles. Barracuda offers so-called injection boundary conditions which were used for that. For the bottom fluidization in the gasification and combustion reactor even flow boundary conditions were used.

For the simulations three simulation cases are selected from results of the cold flow model experiments:

- **Simulation case 1:** bottom fluidization in the riser of 0.0072 kg/s, Table 4.2

- **Simulation case 2:** bottom fluidization in the riser of 0.022 kg/s, Table 4.3

- **Simulation case 3:** bottom air varied between 0.025 to 0.033 kg/s, Table 4.4
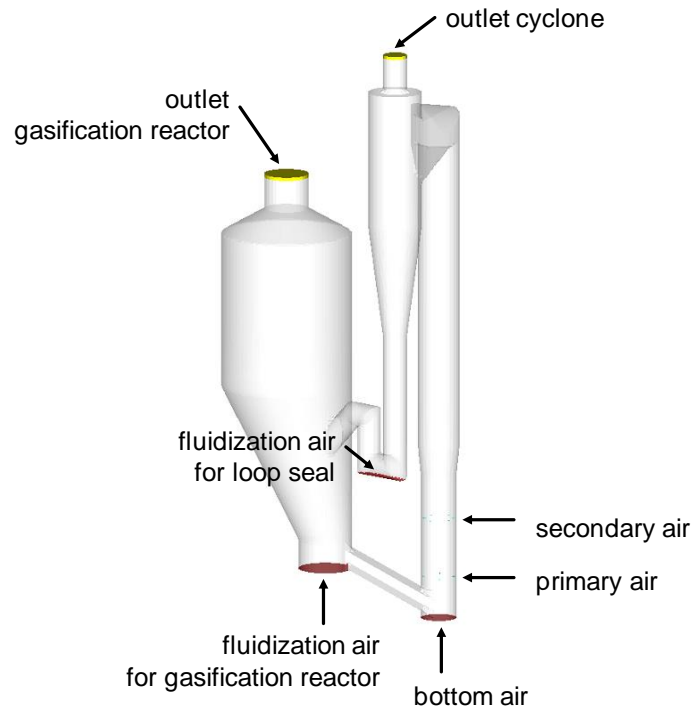
**Figure 4.3:** *Boundary conditions used in the simulations of the cold flow model.*

For simulation case 1 and simulation case 2, an increasing ratio of secondary to total air, $\dot{m}_{sec}/\dot{m}_{tot}$, was used; the air feed moves further up in the riser, more air is fed in the secondary air position. For simulation case 3, the ratio of secondary to primary air, $\dot{m}_{sec}/\dot{m}_{prim}$, was kept constant, only the bottom air was varied. For all experiments the total air into the riser was kept constant.

**Table 4.2:** *Inlet mass flows for simulation case 1, a bottom fluidization of the riser of 0.0072 kg/s.*

| reference | $\dot{m}_{sec}/\dot{m}_{tot}$ | gasification reactor (kg/s) | bottom air (kg/s) | primary air (kg/s) | secondary air (kg/s) | loop seal |
|---|---|---|---|---|---|---|
| S01a | 0.4 | 0.016 | 0.0072 | 0.091 | 0.061 | 0.0022 |
| S01b | 0.5 | 0.016 | 0.0072 | 0.078 | 0.079 | 0.0022 |
| S01c | 0.6 | 0.016 | 0.0072 | 0.059 | 0.096 | 0.0022 |
| S01d | 0.7 | 0.016 | 0.0072 | 0.041 | 0.110 | 0.0022 |

The operating points and ranges used for the present simulations are also drawn into the regime diagram by Grace [68] extended by Schmid et al. [1], Figure 4.4. For the calculation the values in Table 4.5 were used. The operation point of the loop seal is

**Table 4.3:** *Inlet mass flows for simulation case 2, a bottom fluidization of the riser of 0.022 kg/s.*

| reference | $\dot{m}_{sec}/\dot{m}_{tot}$ | gasification reactor (kg/s) | bottom air (kg/s) | primary air (kg/s) | secondary air (kg/s) | loop seal |
|---|---|---|---|---|---|---|
| S03a | 0.4 | 0.016 | 0.022 | 0.075 | 0.066 | 0.0022 |
| S03b | 0.5 | 0.016 | 0.022 | 0.058 | 0.082 | 0.0022 |
| S03c | 0.6 | 0.016 | 0.022 | 0.045 | 0.096 | 0.0022 |
| S03d | 0.7 | 0.016 | 0.022 | 0.028 | 0.11 | 0.0022 |

**Table 4.4:** *Inlet mass flows for simulation case 3, the simulations with varied bottom air between 0.025 to 0.033 kg/s.*

| reference | $\dot{m}_{sec}/\dot{m}_{prim}$ | gasification reactor (kg/s) | bottom air (kg/s) | primary air (kg/s) | secondary air (kg/s) | loop seal |
|---|---|---|---|---|---|---|
| B03a | 1.9 | 0.016 | 0.025 | 0.049 | 0.095 | 0.0022 |
| B03b | 1.9 | 0.016 | 0.028 | 0.047 | 0.089 | 0.0022 |
| B03c | 1.8 | 0.016 | 0.033 | 0.047 | 0.085 | 0.0022 |

calculated for one of the two legs.

As it can be seen the gasification reactor as well as the loop seal are operated in the bubbling bed regime. The bottom fluidization air of the combustion reactor is varied over a large range, starting about from the middle of the bubbling fluidization regime ($\dot{m}_{bottom}$ = 0.0072 kg/s) until the border to the turbulent fluidization ($\dot{m}_{bottom}$ = 0.033 kg/s). In all simulation cases at the top of the combustion reactor the fast fluidization regime is reached which ensures the particle transportation upwards and the bed material recirculation.

**Simulation parameters**

The simulations parameters for the Barracuda simulation are shown in Table 4.1. Furthermore, the blended acceleration model in Barracuda [79] was turned on.
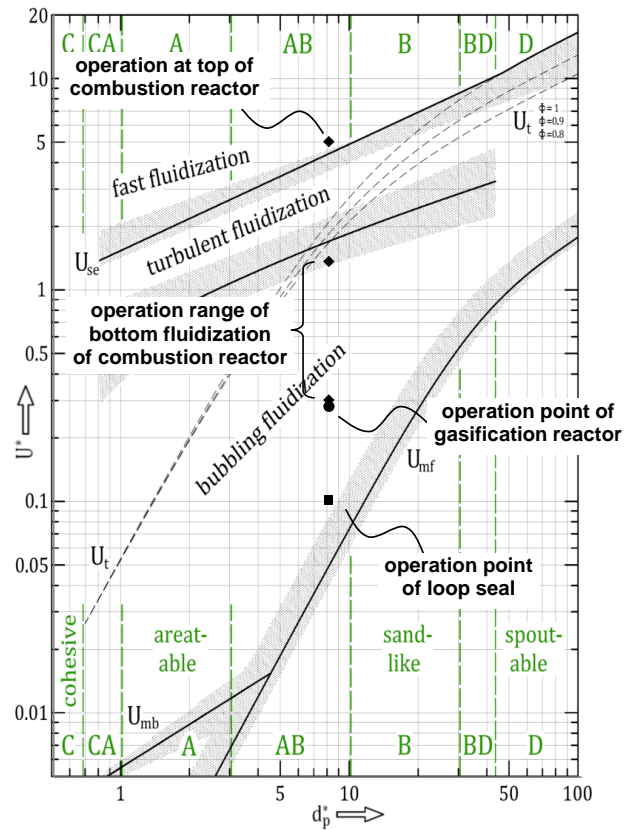
**Figure 4.4:** *Operating conditions of the cold flow model experiments.*

## 4.3 Modeling of the hot Güssing reactor

In this section the modeling of the hot reactor of the Güssing DFB system is described. Geometry and boundary conditions are presented as well as the chemical reactions ranging from drying and devolatilization of the biomass particles to heterogeneous and homogeneous oxidation reactions.

### 4.3.1 Modeling of chemical reactions

#### Pyrolysis model

The used reaction mechanism for the simulations of the DFB reactor in Güssing is shown in Figure 4.5. It represents the main steps drying, primary and secondary pyrolysis and also the division of the devolatilization products into "wood gas", "tar" and "char", as described in section 2.2.

First the wet biomass particle is fed into the reactor. A drying step follows where the moisture evaporates and leaves the particle. The dried particle further undergoes

**Table 4.5:** *Simulation parameters for the simulation of the Güssing cold flow model.*

| **particle-to-wall interaction** | |
| --- | --- |
| normal-to-wall retention coefficient | 0.3 |
| tangent-to-wall retention coefficient | 0.99 |
| diffuse bounce | 0 |
| **particle-to-particle interaction** | |
| close-pack particle volume fraction, $\varepsilon_{cp}$ | 0.616 |
| maximum momentum redirection from collision | 40% |
| pressure constant in Eq. (2.54), $P_s$ | 1 Pa |
| non-dimensional exponent in Eq. (2.54), $\beta$ | 3 |
| non-dimensional constant in Eq. (2.54), $\alpha$ | $10^{-7}$ |
| **time settings** | |
| total simulation time | 20 s |
| start time for averaging | 10 s |
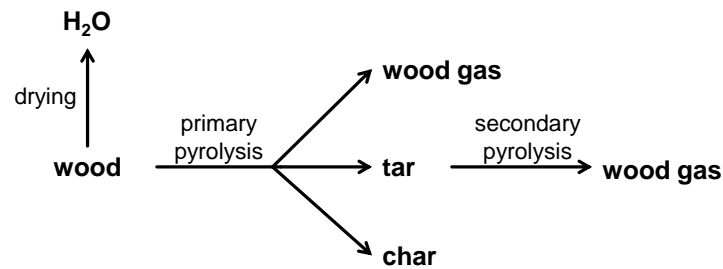


**Figure 4.5:** *Mechanism for biomass conversion used in the present study.*

a primary pyrolysis step where the three pseudo-components wood gas, tar and char are formed. Diego et al. [176] showed that during pyrolysis the particle size slightly decreases. This little particle shrinkage is also considered in the simulations. In a secondary pyrolysis step the "tar" component is further degraded into wood gas.

In the present model, the product gas does not contain any tar load. The tar component is fully converted to wood gas. Since the amounts of tar in the raw product gas is in the range of g/Nm$^3$ [17] and is thus unlikely to have an influence on hydrodynamics, it is neglected.

Wood gas consists of the components $H_2$, CO, $CO_2$, $CH_4$ and steam. Since the prediction of the composition of the product gas for biomass pyrolysis is not possible yet [16] the composition is fixed. In Table 4.6 the mass composition of wood gas after the primary pyrolysis according to Bryden and Ragland [177] is shown in the first

column.

**Table 4.6:** *Composition of wood gas after primary [177] and secondary pyrolysis [178].*

| component | primary pyrolysis | secondary pyrolysis |
|-----------|-------------------|---------------------|
| $H_2$ | 0.084 | 0.207 |
| $CO$ | 0.306 | 0.527 |
| $CO_2$ | 0.192 | 0.124 |
| $CH_4$ | – | 0.142 |
| $H_2O$ | 0.418 | – |

The composition of the "tar" is not specified and acts as pseudo-component where all the higher hydrocarbons and organic condensable gases are lumped together. It is an intermediate product in the devolatilization mechanism of the reaction of the biomass particles. After the "tar" component has formed, it undergoes a further conversion step which is called secondary pyrolysis.

The secondary pyrolysis reactions are modeled as a homogeneous reaction. A simple mechanism was chosen in the present work:

$$tar \rightarrow \nu_{CO}CO + \nu_{CO_2}CO_2 + \nu_{CH_4}CH_4 + \nu_{H_2}H_2 \; . \tag{4.2}$$

The stoichiometric coefficients are set according to Boroson et al. [178] and are depicted in the second column of Table 4.6.

In this work the char moving to the combustion reactor is assumed to consist of pure carbon and ash. The carbon is then oxidized and provides the heat for bed material heat-up. The ash does not participate in the reactions and shows inert character. After full conversion of the char particles only the ash particles remain in the system.

For drying, primary and secondary pyrolysis steps simple Arrhenius approaches of the following form are used, where the *i* represent the different reactions:

$$k_i = k_{0,i}e^{-\frac{E_{a,i}}{R_m T_p}} \; , \tag{4.3}$$

For the drying and primary pyrolysis reactions the kinetics are taken from Chan et al. [179]. The kinetics for the secondary pyrolysis reaction is taken from di Blasi [180]. The values for the pre-exponential factors and the activation energies for the reactions are shown in Table 4.7.

The aforementioned reactions occur with heat effects. The drying reaction is strongly endothermic with the evaporation enthalpy of water, $\Delta h_{evap}$. The primary and sec-

**Table 4.7:** *Kinetic data for drying and primary pyrolysis reactions according to Figure 4.5.*

| reaction | $k_0$ (1/s) | $E_a$ (J/mol) | ref. |
|---|---|---|---|
| drying | $5.13 \cdot 10^6$ | 87,900 | [179] |
| wood $\rightarrow$ gas | $1.3 \cdot 10^8$ | 140,000 | [179] |
| wood $\rightarrow$ tar | $2.0 \cdot 10^8$ | 133,000 | [179] |
| wood $\rightarrow$ char | $1.08 \cdot 10^7$ | 121,000 | [179] |
| tar $\rightarrow$ gas | $4.26 \cdot 10^6$ | 107,000 | [180] |

ondary pyrolysis reactions show lightly endothermic behavior. Values are taken from Gronli and Melaaen [61].

Calculated and measured devolatilization times were compared to ensure meaningful predictions by the single particle reaction mechanism. Therefore, experimentally obtained values by Sreekanth et al. [57] were used and are depicted with the simulation results in Figure 4.6. The single particle model overestimates the devolatilization time for particles with a diameter smaller than 25 mm particles and underestimates the devolatilization times for particles with $d_p$ = 25 mm. The error is 12% or smaller and is considered as sufficiently small for the following simulations.
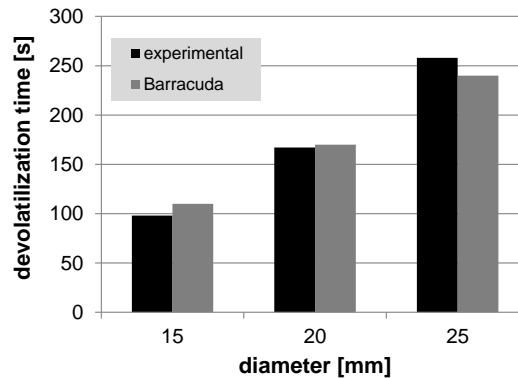


**Figure 4.6:** *Calculated and measured devolatilization times from Sreekanth et al. [57].*

**Further considered reactions**

In the simulation also homogeneous and heterogeneous gas phase kinetics are employed, Table 4.8.

The kinetics for the water-gas-shift (WGS) reaction is taken from Macak and Malecha [181] and the reaction mechanism is expressed in the following form:

**Table 4.8:** *The homogeneous and heterogeneous reactions.*

| reaction | name | number |
|---|---|---|
| $C + O_2 \rightarrow CO_2$ | char oxidation | (A) |
| $CO + H_2O \leftrightarrow CO_2 + H_2$ | water-gas-shift reaction | (B) |
| $2\,CO + O_2 \rightarrow 2\,CO_2$ | CO oxidation | (C) |
| $2\,H_2 + O_2 \rightarrow 2\,H_2O$ | $H_2$ oxidation | (D) |
| $CH_4 + 2\,O_2 \rightarrow CO_2 + 2\,H_2O$ | $CH_4$ oxidation | (E) |
| $C_{16}H_{34} + 24.5\,O_2 \leftrightarrow 16\,CO_2 + 17\,H_2O$ | RME oxidation | (F) |

$$\dot{r}_{WGS} = k_0 e^{\frac{E_a}{R_m T_p}} \left( c_{CO} c_{H_2O} - \frac{c_{CO_2} c_{H_2}}{K_{WGS}} \right) \tag{4.4}$$

where $K_{WGS}$ is the equilibrium constant of the water-gas-shift reaction and can be calculated with the following equation [16]:

$$K_{WGS} = \frac{y_{H_2} y_{CO_2}}{y_{H_2O} y_{CO}} = 0.029 e^{\frac{4094}{T_p}} \tag{4.5}$$

The $y_i$ are the molar fractions of the gas components $H_2$, $CO_2$, $H_2O$ and CO. In the Güssing plant the water-gas-shift (WGS) reaction is not in equilibrium. Therefore, the equilibrium constant was adapted to match the conditions in the real operation. Kinetics for these reactions are depicted in Table 4.9.

The kinetics used for the homogeneous oxidation reactions of CO, $H_2$ and $CH_4$ occurring in the combustion reactor due to the recirculated product gas are also shown in 4.9.

**Table 4.9:** *Parameters for the homogeneous gas phase reactions.*

| reaction number | reaction rate $(mol/m^3)$ | $k_0$ (dependent) | $E_a$ (kJ/mol) | ref. |
|---|---|---|---|---|
| (B) | see Eq. (4.4) | 2.78 | 12.6 | [181] |
| (C) | $\dot{r} = k c_{CO} c_{O_2}^{0.25} c_{H_2O}^{0.5}$ | $3.98 \cdot 10^{20}$ | 167 | [182] |
| (D) | $\dot{r} = k c_{H_2} c_{O_2}$ | $2.20 \cdot 10^{18}$ | 109 | [183] |
| (E) | $\dot{r} = k c_{CH_4}^{0.7} c_{O_2}^{0.8}$ | $1.58 \cdot 10^{19}$ | 203 | [184] |

In the gasification reactor, gasification reactions like $C + H_2O \rightarrow CO + H_2$ or $C + CO_2 \rightarrow 2\,CO$ also occur. The time scales of these reactions are slow compared to the drying and devolatilization processes [185]. Therefore they have been omitted for

simplicity and due to the calculation times of 150 s which is little compared to the usual operation, which is on the order of $10^3$ hours.

The oxidation of the char (reaction equation (A) in Table 4.8) is modelled according to Wartha [186] with an Arrhenius approach:

$$\dot{r}_{char} = 8.56 \cdot 10^{-2} e^{\frac{16,600}{R_m T_P}} S_{p,char} p_{O_2}^{0.5} \; . \tag{4.6}$$

The reaction scheme for the oxidation of the RME emulsion is depicted in Figure 4.7. The RME emulsion enters the system as liquid particle. First it undergoes a drying step where the water is released followed by the evaporation step of the liquid RME. The gaseous RME is modelled as n-Hexadecane. The reaction equation of the gas-phase oxidation of the gaseous RME is depicted in Table 4.8, reaction (F), and modelled according to Sazhin [187]:

$$\dot{r}_{RME} = 2.137 \cdot 10^9 \cdot e^{-\frac{125,000}{R_m T}} c_{RME}^{0.25} c_{O_2}^{1.5} \tag{4.7}$$
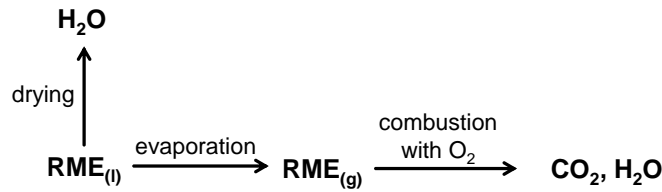


**Figure 4.7:** *Reaction scheme for the RME reaction.*

## 4.3.2 Simulation setup

### Geometry

Construction plans were the basis to implement the geometry of the DFB system in Güssing in Barracuda. The geometry was drawn in Autodesk Inventor and was then imported to the Barracuda Mesh Generator. For the simulations in this work a mesh with 140,000 computational cells was used. Transferring this mesh count to the control volume side-length leads to sizes of about $6 \times 6 \times 6$ cm$^3$. The count for the computational particles in the simulation were set to approximately 700,000 computational particles.

**Initial and Boundary conditions**

In the current study the system was initially filled with nitrogen. According to operational data the total bed material mass of 3000 kg was implemented. To shorten the simulation time the bed material in the gasification reactor and the combustion reactor was set to temperatures typical for operation.

The inlet streams are as follows:

- **Biomass:** Wood chips are fed into the gasification reactor.

- **Fluidization steam.** The gasification reactor and the loop seal are both fluidized with steam.

- **Fluidization air:** The fluidization of the combustion reactor is carried out with air. There are three separate streams: bottom, primary and secondary air.

- **Recycled streams:** From downstream gas cleaning fly char from the product gas filter and RME emulsion from the tar scrubber are fed back to the combustion reactor. Furthermore, product gas is fed back into the combustion chamber for temperature control.

- **Air for oil burner:** A small amount of air is used to cool the oil burner which is located in the combustion reactor.

These boundary conditions are implemented as flow conditions. The data for these inlet mass flows are taken from operational data from the control system of the plant. Their positions within the DFB system is shown in Figure 4.8. The boundary conditions for the bottom fluidization of the gasification and combustion reactor, respectively, as well as for the wood inlet were implemented as even boundary conditions. Inlet for the fluidization of the loop seal, primary and secondary air in the combustion reactor as well as inlet for RME emulsion, product gas recirculation and fly char recirculation were implemented as injection boundary conditions which represent a pointwise inlet.

The values of all mass flows over the system boundaries with their temperatures are shown in Table 4.10. The given temperatures represent the temperature with which the stream is inserted into the system.

There are two flows out of the systems:

- product gas exit
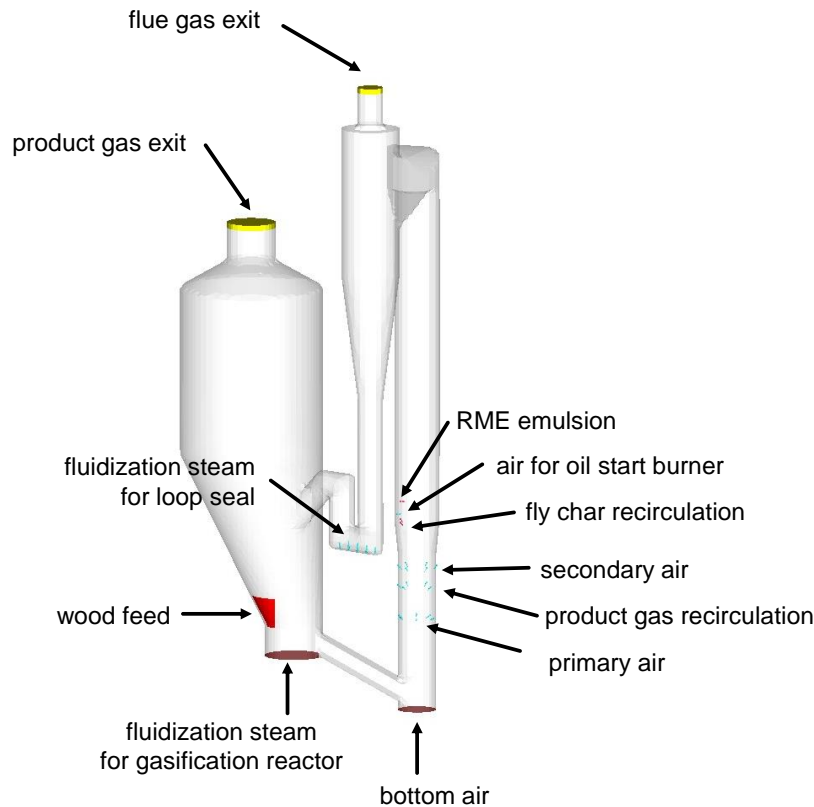
**Figure 4.8:** *Inlet and outlet boundary conditions for the simulation of the Güssing commercial DFB system.*

• flue gas exit

Both these boundary conditions are implemented as pressure conditions where the pressure is specified. Their positions are also shown in Figure 4.8.

Comprehensive process simulations have been carried out of this reactor [188]. The bed material recirculation rate is hard to measure therefore only values from process simulation and from experience were available. A value of $\dot{m}_{rec}$ = 27 kg/s was assumed for the commercial plant. Furthermore, the composition of the flue gas was not measured and also the values from process simulations were used.

As already mentioned a stream of recirculated product gas is fed back to the combustion reactor for temperature control of the system. For the simulation its composition is kept constant for simplicity and because large fluctuations are not considered to occur during the duration of the simulation which is short compared to typical operation times. In this work the following composition of the dry product gas was applied: $y_{CH_4}$ = 10%, $y_{CO}$ = 21%, $y_{CO_2}$ = 24% and $y_{H_2}$ = 45%. This corresponds to a typical composition of the product gas and is in accordance with measurement values from the

**Table 4.10:** *Mass flows and temperatures of the inlet streams for the boundary conditions.*

|                      | mass flow | temperature |
| -------------------- | --------- | ----------- |
|                      | (kg/s)    | (K)         |
| **gasification reactor** |       |             |
| steam                | 0.1238    | 673         |
| wood                 | 0.717     | 298         |
| **loop seal**        |           |             |
| steam                | 0.0158    | 673         |
| **combustion reactor** |         |             |
| bottom air           | 0.266     | 695         |
| primary air          | 0.75      | 695         |
| secondary air        | 0.315     | 695         |
| starting burner      | 0.01      | 338         |
| product gas          | 0.0194    | 358         |
| RME emulsion         | 0.0156    | 353         |
| fly char             | 0.00528   | 379         |

commercial plant as published by Kirnbauer et al. [6].

In addition to flow and pressure boundary conditions also thermal boundary conditions can be implemented in Barracuda. Doing so also the heat loss of the system can be considered. According to Pröll [188] the heat loss in such commercial DFB system is limited to a low percent value. Parameters are set in the simulation to account for such low percent ranges of the heat loss.

**Particle species used in the simulations**

As previously mentioned, a DFB system is a complex system where many different particle species are present:

- bed material

- wood chips

- wood char

- fly char

- RME droplets

Table 4.11 provides all the necessary data for the simulations. In the following additional information is given.

In the commercial plant olivine is used as bed material. Catalytic effects do not influence the fluid mechanics and are therefore not considered. The solid and bulk density as well as the specific heat capacity of the bed material were taken from Bosch [20]. Kirnbauer et al. [6] published a particle size distribution of olivine used in the commercial plant with a mean particle diameter of $d_p$ = 510 μm. This particle size distribution was also implemented in Barracuda and used in the simulations. It is shown in Figure 4.9.
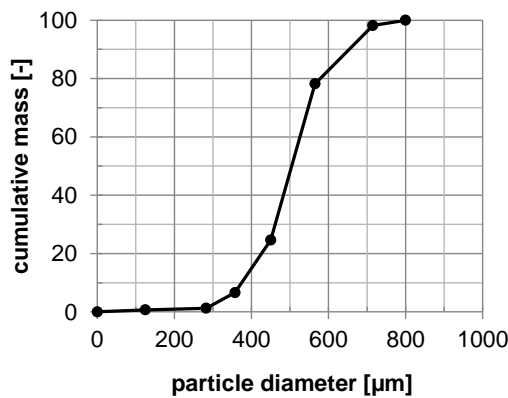


**Figure 4.9:** *Particle size distribution of the olivine particles according to [6].*

The particle size distribution of the wood particles were chosen according to Jünger [189] and is depicted in Figure 4.10. Values for the moisture content of the biomass are taken from experience and from Bosch [20] and are $x_{moisture}$ = 0.33 for the simulations. As fuel mostly hard wood is used in the CHP plant in Güssing. For its dry state a density of 660 kg/m$^3$ is assumed [44]. Since density is important for hydrodynamics of particles in fluidized beds, see chapter 3, the density increases due to the high water content is considered and estimated according to [190].

For the char a density of 300 kg/m$^3$ is specified according to given literature values which are in the range of 200 to 450 kg/m$^3$ [191, 56, 192, 193, 194, 62].

Kirnbauer et al. [195] published the experimental composition of fly char. For the current case it was assumed that the fly char only consists of carbon and ash, similar to the char. The particle size distribution for the fly char was also set according to measurements.

In the commercial plant RME emulsion is fed into the system as droplets which is simulated in the current simulation as particles. The composition is estimated according to experience values and a composition of 50 wt.-% water (condensate) and RME,
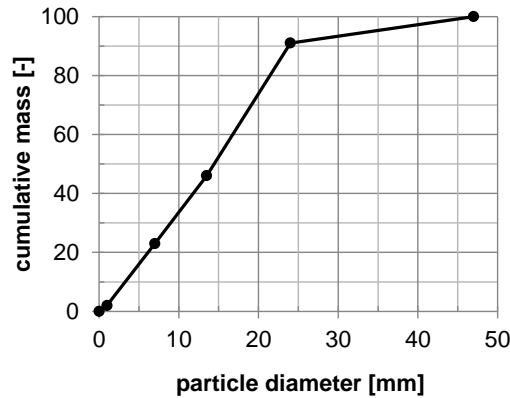
**Figure 4.10:** *Particle size distribution of the wood chips according to [189].*

respectively, is set. As previously mentioned, the RME is modeled as n-Hexadecane (Cetane, $C_{16}H_{34}$).

## Simulation parameters

As pointed out in section 4.3.1 the fuel particle models include drying, primary and secondary pyrolysis processes. Haseli et al. [54] as well as Sreekanth et al. [57] provide time scales for the release of the volatiles of wood particles which are of different size. As they showed typical time scales are in the range of $10^2$ seconds for particles with sizes in the order of $(0.1–5)\times10^{-2}$ m. Therefore, the calculation time for the simulations is set to 150 s to cover also complete devolatilization of particles fed into the system.

As starting time for averages 100 s were used, the average period is thus from 100 to 150 s. These two times are also shown in Table 4.12.

Time steps for the simulations of the commercial plant were in the range of $3 \cdot 10^{-4}$ to $8 \cdot 10^{-4}$ s. The Barracuda solver automatically controls the time steps according to the Courant–Friedrichs–Lewy (CFL) number. It took about 1.5 hours to simulate 1 second.

For the simulations further parameters have to be specified which are summarized in Table 4.12. The implemented blended acceleration model [79] is used in all the simulations conducted in this work. The convective heat transfer between the gas and particles is calculated with the equation of Ranz–Marshall [35, 36] which is shown in Eq. (2.26).

**Table 4.11:** *Parameters for particles and liquid droplets.*

| bed material (olivine) | | ref. |
|---|---|---|
| solid density [kg/m$^3$] | 2800 | [20] |
| bulk density [kg/m$^3$] | 1540 | [20] |
| particle diameter [µm] | 510 | [6] |
| specific heat capacity [kJ/(kg K)] | 0.95 | [20] |
| **wood chips** | | |
| wet solid density [kg/m$^3$] | 800 | op. data |
| dry solid density [kg/m$^3$] | 660 | op. data |
| particle diameter [mm] | 14.5 | [189] |
| $x_{wood,H_2O}$ [kg/kg] | 0.33 | op. data |
| $x_{wood,ash}$ [kg/kg] | 0.01 | op. data |
| $\Delta h_{pyrolysis}$ [kJ/kg] | 150 | [43] |
| **wood char** | | |
| solid density [kg/m$^3$] | 300 | estimated |
| mean particle diameter [mm] | 15 | [189] |
| **RME emulsion** | | |
| density RME [kg/m$^3$] | 880 | [196] |
| $\Delta h_{evap,RME}$ [kJ/kg] | 254 | [196] |
| $x_{droplet,H_2O}$ [kg/kg] | 0.50 | op. data |
| $x_{droplet,RME}$ [kg/kg] | 0.50 | op. data |
| **fly char** | | |
| solid density [kg/m$^3$] | 300 | estimated |
| $x_{flychar,C}$ [kg/kg] | 0.26 | [195] |
| $x_{flychar,ash}$ [kg/kg] | 0.74 | [195] |

## 4.4  Simulation of the Güssing cold flow model

In this section the results from the simulations of the Güssing cold flow model are
presented. First a discussion about the quality of the prediction of the minimum flu-
idization velocity is given. Another focus lies in the investigation of the pressure and
the particle volume fraction inside the system. Especially the measured pressure pro-
files are compared to the experimental data. Since the bed material recirculation rate
is important for the commercial plant, it was also calculated with Barracuda and com-
pared to experimental data.

To quantify the deviations between experimentally found and simulated values the

**Table 4.12:** *Simulation parameters.*

| particle-to-wall interaction | |
|---|---|
| normal-to-wall retention coefficient | 0.3 |
| tangent-to-wall retention coefficient | 0.99 |
| diffuse bounce | 0 |
| **particle-to-particle interaction** | |
| close-pack volume fraction | 0.54 |
| maximum momentum redirection from collision | 40% |
| pressure constant, $P_s$ | 1 Pa |
| non-dimensional exponent, $\beta$ | 3 |
| non-dimensional constant, $\alpha$ | $10^{-7}$ |
| **time settings** | |
| total simulation time | 150 s |
| start time for averaging | 100 s |

relative deviation, $rd$, is introduced

$$ rd = \left| \frac{x_{simulation} - x_{experiment}}{x_{simulation}} \right| \tag{4.8} $$

with $x_{simulation}$ and $x_{experiment}$ as the values obtained by Barracuda simulation and experiment, respectively. If in this section the term relative deviation is mentioned, always $rd$ in the definition according to Eq. (4.8) is used.

## 4.4.1 Calculation of the minimum fluidization velocity

The minimum fluidization velocity is a characteristic velocity for fluidized beds hydrodynamics since it determines the transition from fixed to bubbling bed.

As previously mentioned the drag law has a large influence on the gas-particle momentum transfer. Without doing any measurements it is difficult to say which drag law to use for the calculations.

If $u_{mf}$ and the hydrodynamic behavior of a fluidized bed is predicted correctly this could serve as a first hint which drag law to use. Bosch [20] measured the minimum fluidization velocity for the bed material he used in his experiments. This value is shown in Figure 4.11 and is labeled as "experimental". The minimum fluidization velocity was also calculated with Barracuda to obtain a first estimate of the prediction quality of the different drag laws used in this work.

Figure 4.11 shows the calculated $u_{mf}$ with the drag laws EMMS, Ganser, Turton-Levenspiel and Wen-Yu/Ergun. Furthermore, $u_{mf}$ was calculated with two correlations of the form of Eq. (2.16). In the correlations the coefficients proposed by Wen and Yu [32] and Grace [33] were used.
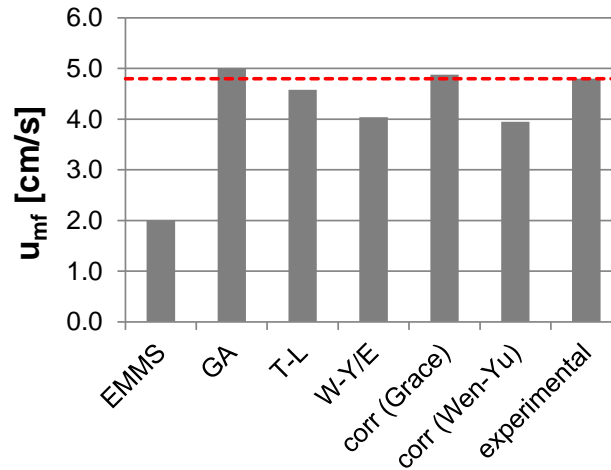


**Figure 4.11:** *Minimum fluidization velocity, $u_{mf}$, simulated various drag laws and also calculated with two correlations as well as the experimentally obtained value. Ga ... Ganser, T–L ... Turton-Levenspiel, W–Y/E ... Wen-Yu/Ergun.*

It can be seen that the EMMS drag law produces the largest error with a relative deviation of about 60%. The best predictions are made by the drag laws by Ganser and Turton-Levenspiel which with relative deviations of about 4%. The Wen-Yu/Ergun blend drag law produces relative deviations of about 15%.

It should be noted that the coefficients proposed by Wen and Yu [32] produce larger deviations than the coefficients proposed by Grace [33]. Generally, the former one always give larger $u_{mf}$ than the latter.

## 4.4.2  Fluidization regimes in the cold flow model

The DFB system is a hydrodynamically complex system since various particle regimes are present: fixed bed, bubbling fluidized bed, fast fluidized bed. The qualitative prediction of these regimes is important for further investigations of hydrodynamics via simulations.

Figure 4.12 shows the particle distribution in the cold flow model for all the simulated drag laws for the simulation case S01a ($\dot{m}_{bottom} = 0.022$ kg/s and $\dot{m}_{sec}/\dot{m}_{tot} = 0.4$).
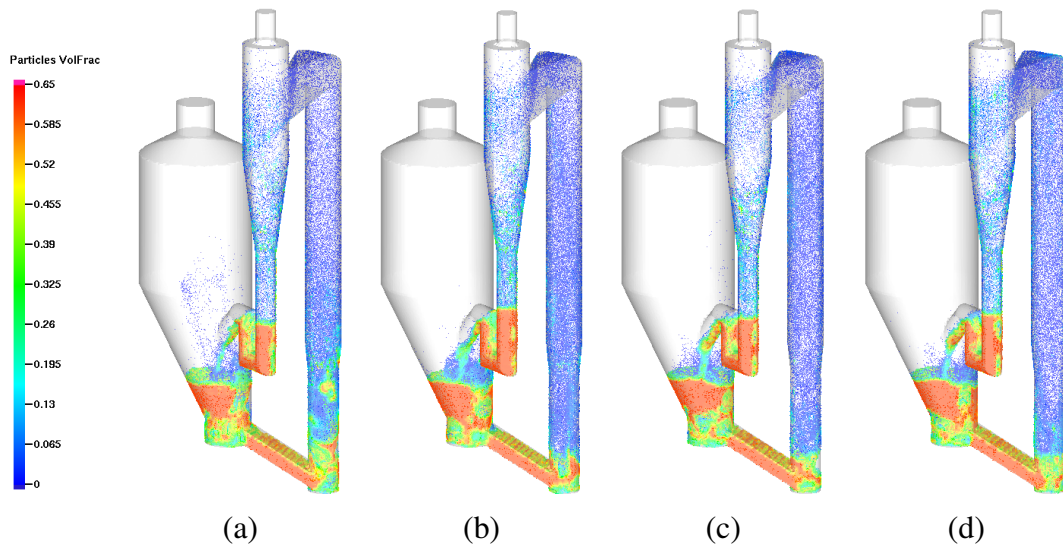
**Figure 4.12:** *Calculated particle volume fraction in the cold flow model with the different drag laws for simulation case S01a. (a) ... EMMS, (b) ... Ganser, (c) ... Turton-Levenspiel, (d) ... Wen-Yu/Ergun. Red color indicates close pack volume fraction, blue particles indicate dilute flow.*

The colors of the particles indicate the packing state of the particles. The legend on the left in Figure 4.12 shows the particle volume fraction, $\varepsilon_p$. Red colors indicate close pack ($\varepsilon_p \rightarrow \varepsilon_{cp}$) or a fixed bed condition. A more dilute gas-solid flow is indicated by blue colors where $\varepsilon_p \rightarrow 0$.

According to Figure 4.12 all drag laws predict the regimes well. In the gasification reactor a bubbling bed occurs in the simulations. The chute is filled with a moving fixed bed and the fast fluidized bed regime in the combustion reactor is depicted qualitatively correct. Furthermore, the characteristic denser zone at the bottom of the fast fluidized bed is also predicted. With increasing height the gas-solids flow become more dilute. Separation of particles from the air flow occurring in the cyclone is also predicted by the simulation. In the loop seal a bubbling bed can be observed which also corresponds to the experimental experience.

## 4.4.3 Prediction of the pressure in the cold flow model

In this section the measured and calculated pressures are compared. For the gasification reactor and the two legs of the loop seal only the pressures at the bottom of the beds were measured and compared to the simulations. For the combustion reactor pressures over the height were measured. Therefore, it was also possible to compare a calculated pressure profile over the height with these 4 measurements.

**Gasification reactor and loop seal**

In the Güssing cold flow model pressures were measured at the bottom of the gasification reactor and at the bottom of each of the two legs of the loop seal. These pressures were also calculated with Barracuda and compared to the experimental results.

The comparison of the simulated and experimentally obtained results are compared in Figure 4.13. Three diagrams are depicted each for one of the three simulation cases 1 (S01a–d), 2 (S03a–d) and 3 (B03a–c). For each simulation case the bottom pressures for the gasification reactor and the two legs of the loop seal ("up" and "down" according to Figure 4.2) are depicted.

Since the pressures in each simulation case do not vary much mean values were calculated and used in the diagrams to get a qualitative overview of the prediction quality of the drag laws.

It can be seen that all the drag laws give qualitative good predictions for the pressure at the bottom of the gasification reactor. However, for the bottom pressure of the loop seal only the EMMS drag model gives values close to the experimentally found ones. The other 3 drag laws (Ganser, Turton-Levenspiel and Wen-Yu/Ergun) obtain pressures which are significantly higher than the experimental values.

For a more quantitative analysis the relative deviations for each simulation is depicted in Table 4.13. The cells are colored according to the relative deviation. Green values mean values of $rd \to 0$. Red values indicate $rd \to 0.5$ since deviations of 50% were considered as large for predictions by a simulation. The range in between is colored with a gradation of colors where the center at $rd = 0.25$ is colored yellow.

It can be seen that the pressure in the gasification reactor is predicted with relative deviations of around or below 10% by all used drag laws which was also seen in Figure 4.13.

Only the EMMS drag law predicts the pressures in the loop seal with relative deviations in a percent range below 20%. For simulation case 1 the relative deviations are around or lower than 10%. For the simulation cases 2 and 3 the relative deviations become slightly higher and are mostly between 10% and 20%.

The other drag laws do not give such low relative deviations. For simulation case 1 the relative deviations are lower (20% to 45%) and increase for simulation cases 2 and 3 up to 65%. As it will be seen in the following this has a direct impact on the prediction quality of the pressure drop in the combustion reactor.

Furthermore, in Table 4.13 also the average relative deviation for each drag law was calculated to give a rough estimation about the prediction quality of the drag laws.
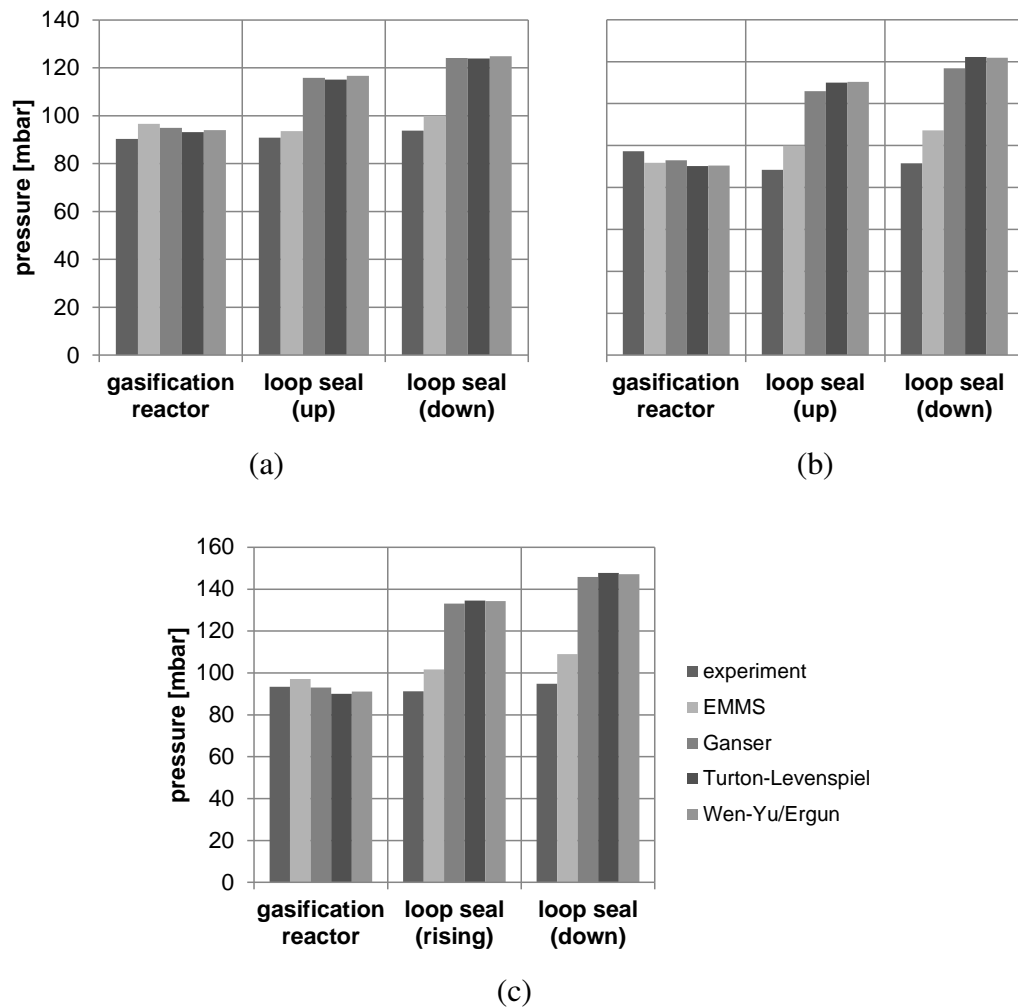
**Figure 4.13:** *Comparison of calculated and measured pressures in the gasification reactor and the "up" and "down" leg of the loop seal. (a) ... simulation case 1, (b) ... simulation case 2, (c) ... simulation case 3.*

The mean value also represents the aforementioned fact that the EMMS drag law gives tendentially the best predictions of the pressure.

## Combustion reactor

For the combustion reactor also measurements over the height were available. Figure 4.14 compares the calculated and experimentally found values of the pressure drops over the combustion reactor. The pressure drops for all simulations were calculated and drawn into the diagram. On the abscissa the experimental and on the ordinate the corresponding simulated values are shown. The black line represents a relative deviation of 0% – the experimental and simulated value match exactly. The interval

**Table 4.13:** *Relative deviation according to Eq. (4.8) of all the simulation results for the pressures at the bottom of the gasification reactor and the two legs of the loop seal. The drag laws by Ganser, Turton-Levenspiel and Wen-Yu/Ergun are shown as GA, T-L and W-Y/E.*

|  |  | EMMS | GA | T-L | W-Y/E |
|---|---|---|---|---|---|
| gasification reactor | S01a | 5.5% | 4.6% | 0.9% | 2.5% |
|  | S01b | 6.2% | 3.8% | 1.5% | 1.9% |
|  | S01c | 7.7% | 5.8% | 4.4% | 5.4% |
|  | S01d | 8.4% | 6.7% | 5.8% | 6.5% |
| loop seal (up) | S01a | 0.4% | 27.2% | 25.9% | 32.2% |
|  | S01b | 6.3% | 32.8% | 33.1% | 36.4% |
|  | S01c | 0.7% | 27.3% | 25.4% | 25.0% |
|  | S01d | 5.7% | 22.3% | 22.5% | 19.7% |
| loop seal (down) | S01a | 3.7% | 32.1% | 31.3% | 38.0% |
|  | S01b | 10.8% | 39.3% | 40.4% | 42.1% |
|  | S01c | 4.0% | 31.9% | 30.4% | 29.2% |
|  | S01d | 8.3% | 26.0% | 26.4% | 23.0% |
| gasification reactor | S03a | 8.0% | 7.6% | 10.4% | 10.6% |
|  | S03b | 2.6% | 3.5% | 4.9% | 4.5% |
|  | S03c | 2.9% | 2.0% | 4.8% | 5.3% |
|  | S03d | 8.7% | 4.2% | 8.7% | 7.1% |
| loop seal (up) | S03a | 12.6% | 42.4% | 47.9% | 53.1% |
|  | S03b | 12.6% | 44.5% | 47.9% | 51.2% |
|  | S03c | 14.0% | 46.1% | 50.7% | 45.3% |
|  | S03d | 13.1% | 37.0% | 41.8% | 40.0% |
| loop seal (down) | S03a | 17.1% | 49.6% | 56.5% | 60.9% |
|  | S03b | 18.7% | 54.2% | 59.2% | 61.9% |
|  | S03c | 16.6% | 51.8% | 57.1% | 51.1% |
|  | S03d | 16.3% | 42.5% | 48.7% | 46.1% |
| gasification reactor | B03a | 11.5% | 1.1% | 3.9% | 3.9% |
|  | B03b | 0.6% | 2.0% | 1.1% | 1.0% |
|  | B03c | 0.6% | 1.9% | 5.6% | 2.5% |
| loop seal (up) | B03a | 10.3% | 40.8% | 42.1% | 46.8% |
|  | B03b | 9.6% | 43.3% | 46.4% | 47.7% |
|  | B03c | 14.5% | 53.7% | 53.9% | 47.3% |
| loop seal (down) | B03a | 16.1% | 51.3% | 52.6% | 56.9% |
|  | B03b | 11.9% | 49.9% | 53.7% | 54.7% |
|  | B03c | 16.9% | 60.1% | 61.1% | 54.1% |
| average |  | 9.2% | 28.8% | 30.5% | 30.7% |
| standard deviation |  | 5.4% | 19.5% | 20.7% | 20.9% |

$-25\% < rd < 25\%$ is represented by the two dashed lines. This would also correspond to the yellow colors in Table 4.13.
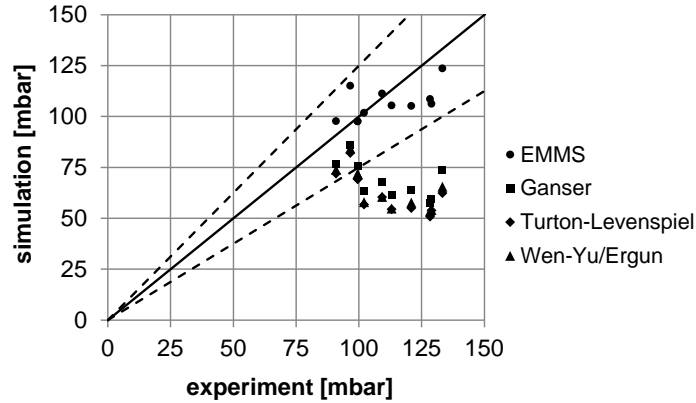


**Figure 4.14:** *Simulated and experimental pressure drops over the riser for all the conducted simulations. The dashed lines represent $-25\% < rd < 25\%$.*

Only the EMMS drag law predicts pressure drops which are within the interval $-25\% < rd < 25\%$. For the other drag laws only some points of Ganser and Turton-Levenspiel are within the ±25% interval. The results produced by the Wen-Yu/Ergun drag law are consistently outside that interval. Deviations are up to 60%.

As previously mentioned, also the pressure profile was measured in the cold flow model. Figure 4.15 shows the simulated pressure distribution over the height of the combustion reactor for all the used drag laws compared to experimental values. In the simulations the pressure was averaged across the cross section area of the combustion reactor. The experimental values are distinct and are marked with a circle.

For simulation cases 1 and 2 the diagrams are shown for $\dot{m}_{sec}/\dot{m}_{tot} = 0.4$ (S01a and S03a). For simulation case 3 the values are shown for the lowest bottom air fluidization (B03a).

In all simulation cases the experimental results of the lowest and the highest pressure measurement are on the pressure profile predicted by the EMMS drag law. This confirms that the pressure drop is predicted well by the EMMS drag model. However, in between the predicted pressure drop is too low for the measurements at 1 and 1.5 m.

The other drag models are not able to predict the overall pressure drop and especially underestimate the pressure at the bottom of the combustion reactor, as it can be seen from Figure 4.15. Similar to the EMMS drag law, they also fail to predict the pressure profile and the experimental points at heights of 1 and 1.5 m.

(a)



(b)



(c)
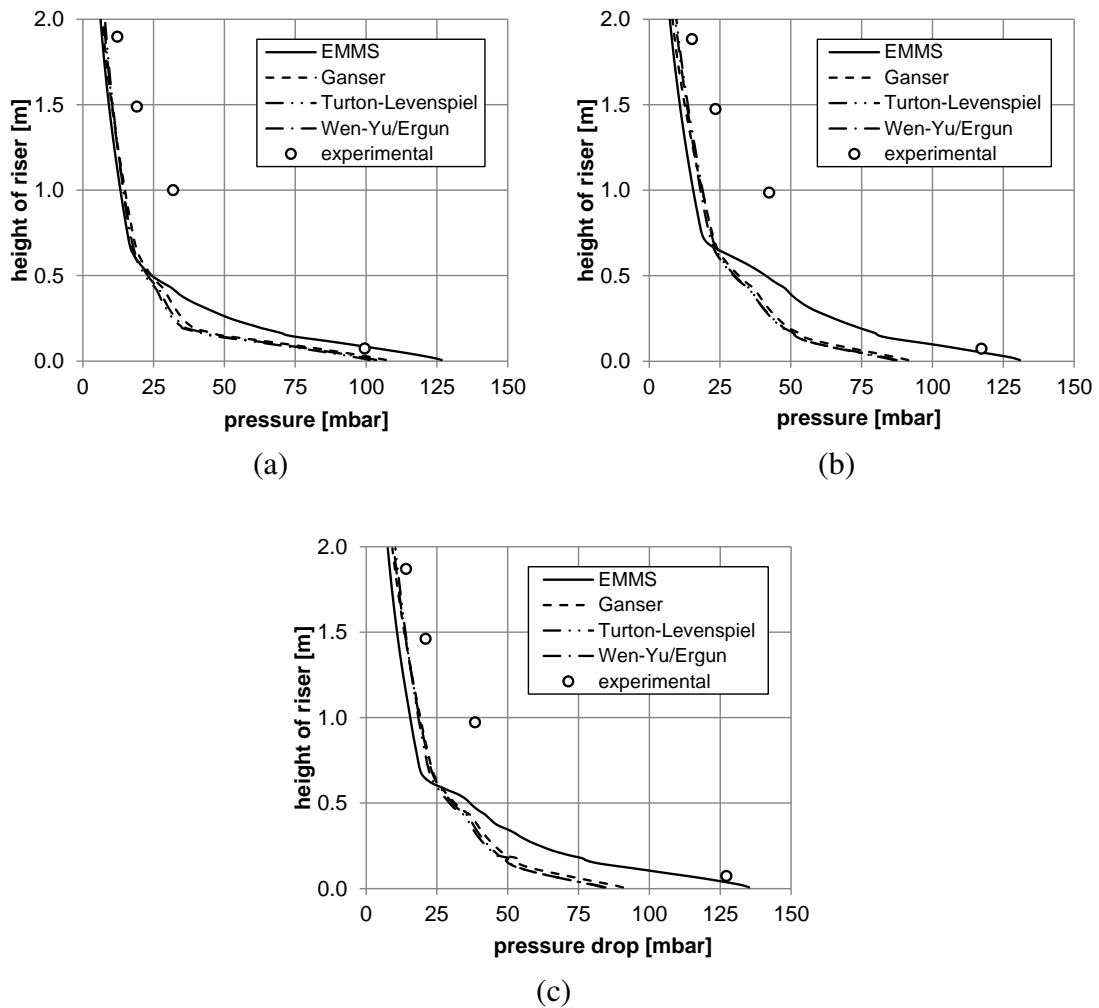
**Figure 4.15:** *Comparison of calculated and measured pressure profiles over the combustion reactor. (a) ... S01a, (b) ... S03a, (c) ... B03a.*

## 4.4.4  Particle volume fraction in the combustion reactor

The particle volume fraction is related to the pressure gradient: $\varepsilon_p \sim \frac{1}{\rho_p g}\nabla p$, if one assumes that $\rho_p \gg \rho_g$, which is a good approximation for gas-solid fluidized beds since the gas density is always in the order of $\rho_g \sim 10^0$ whereas the particle density is in the order of $\rho_p \sim 10^3$. This means that higher calculated pressure gradients also imply that a higher amount of bed material is present in a specific region.

Calculating the pressure drop only gives an estimate of the total bed material amount along the height of the combustion reactor. Therefore, also the particle volume fractions were calculated in the combustion reactor of the cold flow model.

Figure 4.16 depicts the calculated particle volume fraction over the height of the combustion reactor. The data were averaged over time and over the cross section area

of the combustion reactor.
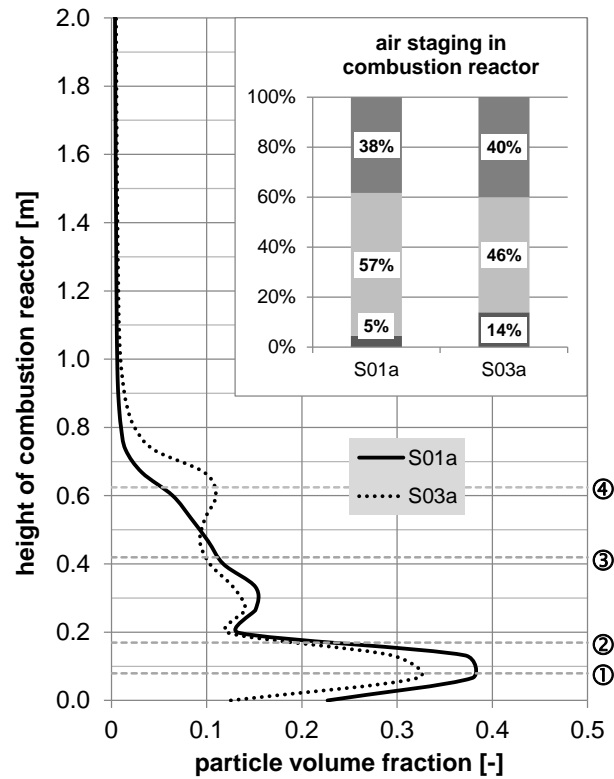


**Figure 4.16:** *Calculated average particle volume fraction in the combustion reactor over the height. S01a and S03a are the simulation cases according to Table 4.2 and 4.3.*

In this Figure curves for the two simulation cases S01a and S03a, according to Table 4.2 and 4.3, for the EMMS drag model are presented. On the abscissa the particle volume fraction, $\varepsilon_p$, is shown and on the ordinate the height of the combustion reactor.

Furthermore, the percentage of the air staging in the combustion reactor is depicted for the two simulation cases. The bottom value is the bottom fluidization, the middle value represents the primary and the top value the secondary fluidization. The difference between S01a and S03a is that more air is shifted from the primary fluidization to the bottom fluidization whereas the secondary fluidization remains nearly constant.

The numbers ①, ② and ③ mean the positions of the bed material inlet from the chute (①) and the inlets of the primary and secondary air, ② and ③. The position of the expansion of the cross section of the combustion reactor is marked with ④.

At the bottom of the combustion reactor particle volume fractions of $\varepsilon_p = 0.2$ to 0.3 occur. At the position of the inlet of the bed material from the chute ① there is an increase of the average bed material concentration.

For the simulation case S01a the average particle volume fraction is higher. Since in this case a lower bottom fluidization occurs also more bed material accumulates at the bottom of the bed.

Moving further upwards in the reactor to the inlet of the primary air ② one sees that there an increase of the particle volume fraction occurs. A denser zone is forming above the inlet of the primary air inlet. This can be seen for both simulation cases S01a and S03a. As it was the case at the bottom also after the primary fluidization $\varepsilon_p$ is higher for S01a.

At the secondary air inlet ③ no increase in the particle volume fraction can be seen for the simulation case S01a but a steady decrease until $\varepsilon_p \rightarrow 0$ at about 0.9 m in height.

For the simulation case S03a there also forms a zone of increasing particle volume fraction at location ④. Compared to the simulation case S01a the bed material is shifted somewhat upwards in the reactor. In the region where the combustion reactor expands to a higher diameter also the particle volume fraction increases forming a denser region of bed material.

Figure 4.17 shows the averaged particle volume fraction for the cut-plane in the middle of the combustion reactor for all drag laws. For better illustration, the maximum of the particle volume fraction was set to 0.4. Therefore, particle volume fractions $\varepsilon_p > 0.4$ occur purple which is the case in the chute of the cold flow model. Red indicates particle volume fractions of $\varepsilon_p \rightarrow 0.4$, whereas blue indicates a dilute flow with $\varepsilon_p \rightarrow 0$.

For all drag laws a zone of a denser bed in the bottom of the combustion reactor can be seen. But as the pressure profiles indicate a higher amount of bed material can be found in the bottom region only for the EMMS drag law. Furthermore, for the EMMS drag law at the location ④ it can be seen that at the wall a denser bed forms compared to the flow in the core.

Such a behavior is similar to the formation of a second bed at this position. Schmid et al. [1] used such constrictions in their novel gasification system.

## 4.4.5 Bed material recirculation rates

For commercial DFB systems the bed material recirculation rate is of great importance since it determines the transport of hot bed material back to the gasification reactor to provide the energy for the devolatilization and gasification reactions. Therefore it influences the temperature levels between gasification and combustion reactor.
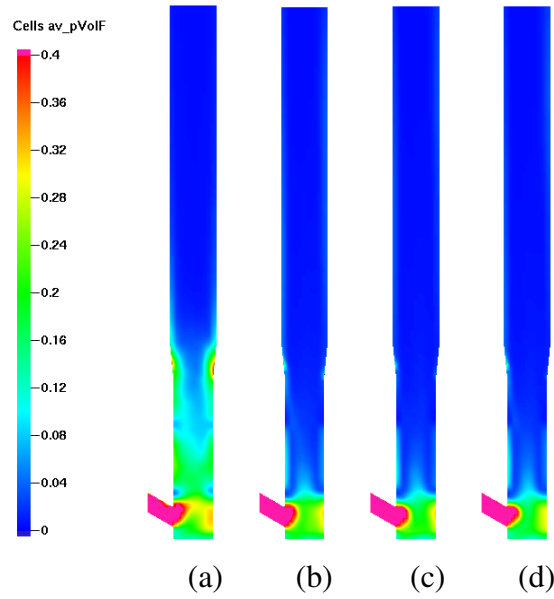
**Figure 4.17:** *Calculated particle volume fractions in the combustion reactor for the simulation case S01a. (a) ... EMMS, (b) ... Ganser, (c) ... Turton-Levenspiel, (d) ... Wen-Yu/Ergun. Red indicates volume fractions of $\varepsilon_p \rightarrow 0.4$, blue particles indicate dilute flow ($\varepsilon_p \rightarrow 0$), purple indicates $\varepsilon_p > 0.4$.*

In the Barracuda simulation the bed material recirculation rate, $\dot{m}_{rec}$, was obtained by differentiating the integrated particle mass which flows through the chute to the combustion reactor.

For all three simulation cases also the bed material recirculation rate was simulated and compared to experimental values. For simulation case 1 and 2 the bed material recirculation rate was investigated dependent on the ratio of secondary and total air in the combustion reactor, $\dot{m}_{sec}/\dot{m}_{tot}$. Increasing $\dot{m}_{sec}/\dot{m}_{tot}$ represents a shift of the air from the primary to the secondary air position, since the bottom air is kept constant for each of the two simulation cases. For simulation case 3 the bottom air was varied with a constant ratio of $\dot{m}_{sec}/\dot{m}_{tot} = 1.9$. For all experiments the total amount of air into the combustion reactor was constant.

The experimental and simulated results for the simulation cases 1 and 2 are shown in the Figures 4.18 and 4.19. In both simulation cases the experiments show that that a shift of air from the primary to the secondary air (increasing $\dot{m}_{sec}/\dot{m}_{tot}$) decreases the bed material recirculation rate.

For simulation case 1 all the drag laws are able to predict the decreasing trend. The drag laws by Ganser, Turton-Levenspiel and Wen-Yu/Ergun are able to predict also the slope of the curve for $0.5 \leq \dot{m}_{sec}/\dot{m}_{tot} \leq 0.7$. Whereas the experiment predicts the largest change in $\dot{m}_{rec}$ for $\dot{m}_{sec}/\dot{m}_{tot} = 0.4 \rightarrow 0.5$ the aforementioned 3 drag laws
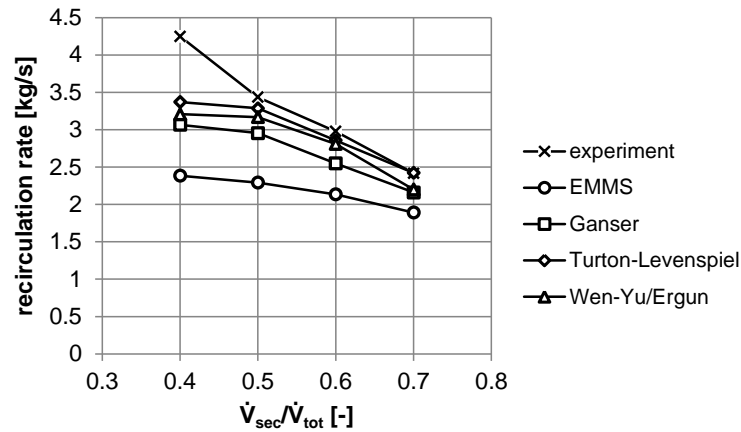
**Figure 4.18:** *Experimental and simulated values for the bed material recirculation rate for simulation case 1.*
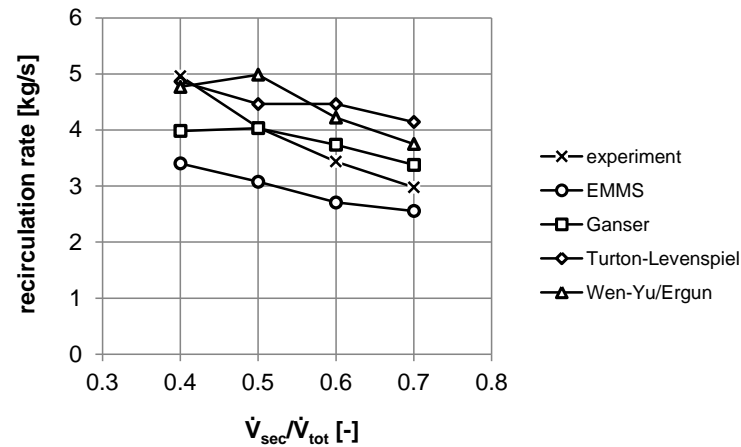


**Figure 4.19:** *Experimental and simulated values for the bed material recirculation rate for simulation case 2.*

predict the smallest change in that region.

The EMMS drag law calculates a curve with a decreasing bed material recirculation rate but with a slope which is too small compared to the experimental results. Furthermore, the EMMS drag law also shows the largest distance to the experimental values which results in the highest relative deviation.

Similar to simulation case 1 also in simulation case 2 the bed material recirculation rate decreases if $\dot{m}_{sec}/\dot{m}_{tot}$ is increased. The drag laws by Ganser and Wen-Yu/Ergun first predict an increase in $\dot{m}_{rec}$ and then a decrease where the slope for the Ganser drag model is smaller than the experimental values. The drag model by Wen-Yu/Ergun produces a slope which is nearly parallel to the experimental curve.

The predicted bed material recirculation rate by the Turton-Levenspiel drag model

goes first down, then up and then down again. The trend is to lower $\dot{m}_{rec}$ which is in agreement with the experimental data. However, for higher $\dot{m}_{sec}/\dot{m}_{tot}$ the deviation between simulation and experiment becomes larger.

As it was for simulation case 1 also for simulation case 2 the EMMS drag model underpredicts the bed material recirculation rate. It shows a qualitative decreasing trend but tendentially not as steep as the experiments.

If the bottom air is increased the bed material rate increases as indicated by the experiments and shown in Figure 4.20.
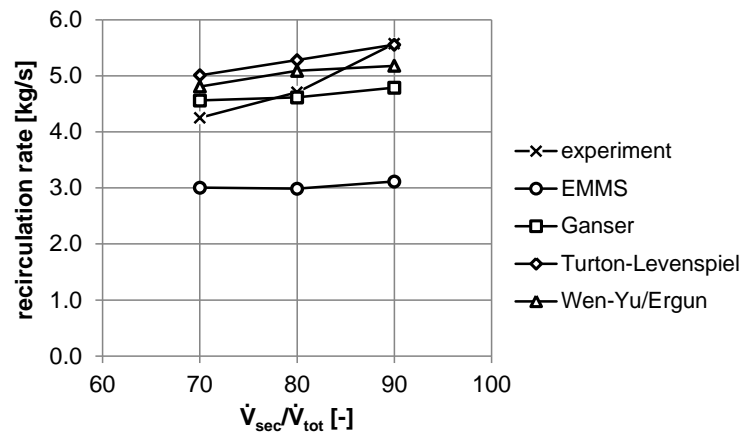


**Figure 4.20:** *Experimental and simulated values for the bed material recirculation rate for simulation case 3.*

The drag models by Ganser, Turton-Levenspiel and Wen-Yu/Ergun predict also qualitatively this increase but to a far smaller extent. These drag laws produce values which are in the range of the values found in the experiments. As in the previous cases the EMMS drag model underpredicts the experimentally found vales and therefore the predicted curve for $\dot{m}_{rec}$ lies under the experimental curve. Only a small increase in $\dot{m}_{rec}$ is predicted by the EMMS drag model for if the bottom air is increased from $\dot{m}_{bottom} = 0.028 \rightarrow 0.033$ kg/s.

Table 4.14 shows the relative deviations of the calculated bed material recirculation rates. This table shows a qualitative overview of the quality of the predictions by the drag laws. The last row shows the results for the Güssing commercial plant, which is discussed in the following section.

It can be seen that the EMMS drag model produces qualitatively the largest deviation. Calculating the average also shows that. Except for the simulation S03d the deviation is always larger than 20% and goes up to 44%.

The other drag laws, Ganser, Turton-Levenspiel and Wen-Yu/Ergun, show tenden-

**Table 4.14:** *Relative deviation of all the simulation results for the bed material recirculation rate.*

|  | EMMS | GA | T-L | W-Y/E |
|---|---|---|---|---|
| S01a | 44% | 28% | 21% | 25% |
| S01b | 33% | 14% | 4% | 8% |
| S01c | 28% | 14% | 4% | 6% |
| S01d | 22% | 11% | 0% | 9% |
| S03a | 31% | 20% | 2% | 4% |
| S03b | 24% | 0% | 10% | 23% |
| S03c | 21% | 9% | 30% | 23% |
| S03d | 14% | 13% | 39% | 26% |
| B03a | 29% | 7% | 18% | 13% |
| B03b | 37% | 2% | 12% | 8% |
| B03c | 44% | 14% | 0% | 7% |
| average | 30% | 12% | 13% | 14% |
| standard deviation | 9.0% | 7.4% | 12.3% | 8.2% |
| Güssing | 18% | 81% | 84% | 80% |

tially lower average deviations as indicated by the mean value. Also the average values of the deviations are for many cases between 0 and 15%. However, relative deviations go up to 39% for the simulation B03c as predicted by the Turton-Levenspiel drag law.

### 4.4.6 Summary and discussion

The simulation results confirm that the drag law has a large influence on the results. Therefore, the prediction of the bed material distribution, pressures in the systems and bed material recirculation rate, depends strongly on the drag law that is used in the simulations.

In the cold flow model various regimes occur: fixed bed (chute), bubbling bed (gasification reactor and loop seal) and fast bed (combustion reactor). Furthermore, also particle separation has to be predicted. Qualitatively, all drag laws are able to predict these processes. Therefore, the Barracuda code is able to predict the fluidization regimes in cold flow models of DFB systems.

All drag laws predict the pressure drop over the bubbling bed in the gasification reactor with a good accuracy; the relative deviation is consistently around or below 10%.

However, only the EMMS drag law predicted the pressures at the bottom of the loop seal and the pressure drop over the combustion reactor with good accuracy. Since the

pressure drop is also related with the amount of bed material in the parts of the system, the accurate prediction of pressure drops is essential.

The other drag laws (Ganser, Turton-Levenspiel and Wen-Yu/Ergun) overpredicted the pressure at the bottom of the loop seal and therefore underpredicted the pressure drop over the combustion reactor. This indicates that too little bed material is present in the combustion reactor. From calculation of the particle volume fraction it can be also qualitatively seen that the amount of the bed material in the "down" leg is higher for the drag laws of Ganser, Turton-Levenspiel and Wen-Yu/Ergun which also indicates a maldistribution of bed material between loop seal and combustion reactor.

Looking only at the simulation of the pressures within the system the EMMS drag model gives the best results, since it is able to give good accuracy for the pressure at the bottom of the gasification reactor and in the two legs of the loop seal. Furthermore, it is the only drag model which gives accurate values of the pressure drop along the height of the combustion reactor. However, it has limitations in predicting the pressure profile over the height.

Although the EMMS drag model predicts well the total pressure drop over the combustion reactor it fails to correctly calculate the pressure profile. Only the bottom and the top measurement is predicted correctly but the pressure measurements in between were underpredicted. Also the other drag laws underpredicted the measured pressure along the height. This implies that too much bed material is found at the bottom of the combustion reactor and too little at the upper part.

An investigation of the particle volume fraction along the height of the combustion reactor showed that a zone with higher bed material amounts could form at the location where the combustion reactor expands to a higher diameter. Such a behavior is similar as also observed by Schmid et al. [1] in their novel gasification system.

The experiments showed that the bed material recirculation rate depends strongly upon the operating conditions. This dependence and the resulting experimentally found trends were only predicted to a small extent by the simulations. Opposite to the pressures the EMMS drag model fails to accurately predict the bed material recirculation rate and produces relative deviations of up 44%. Only one simulation was able to predict the bed material recirculation rate with a relative deviation of below 15% which can be considered as good accuracy. All the other drag models give much lower relative deviations. The drag model by Wen-Yu/Ergun gives acceptable predictions of the trends for simulation case 1 and 2. The experimentally measured trend for simulation case 3 was not predicted by any of the used drag models.

If only the relative deviations between the simulation results and the experimental

values are considered, the Ganser drag model shows the best behavior and also the lowest average relative deviation. However, the results by Wang et al. [161] are not in agreement to these findings.

In the beginning of the section also the minimum fluidization velocity was calculated with all the used drag models. The Ganser drag model predicts best the experimentally found value and the EMMS drag model gives the worst prediction. From this result it seems the most accurate to use the Ganser drag model for the calculations. However, the bed material distribution within the system is then probably not predicted correctly.

From the simulations in this work it is difficult to give a general prediction which drag law to use. Especially, having in mind that the results from the commercial plant where the EMMS drag model surprisingly predicts the bed material recirculation rate much better than the other drag models. This is discussed in more detail in section 4.5.

## 4.5 Simulation of the Güssing commercial plant

In this section the simulation results of the commercial DFB system in Güssing are presented. Since the drag law has a massive influence on the results first the drag model is chosen which gives the best approximation of the bed material recirculation rate in the commercial plant.

After choosing the appropriate drag law temperatures, pressures and gas compositions inside the system were calculated and compared to measured values from the commercial plant. This step acts as a comprehensive model validation to investigate the applicability of the model to investigate design considerations.

The mixing of the hot bed material and the mixing of biomass particles in lateral direction in the bed of the gasification reactor was investigated. Furthermore, the influence of the slope in the gasification reactor on fluidization behavior was investigated.

Similar to the investigation of the Güssing cold flow model also the relative deviation between the simulation and the operation data is defined, according to Eq. (4.8), as follows

$$rd = \left| \frac{x_{simulation} - x_{operation}}{x_{simulation}} \right|, \qquad (4.9)$$

where $x_{simulation}$ means the value predicted by Barracuda and $x_{operation}$ is the value from the real operation.

## 4.5.1 The influence of the drag law on the recirculation rate

The circulating bed material stream transports on the one hand the char loaded bed material to the combustion reactor where the char burns and the bed material is heated up. As it can be seen from Eq. (4.6) the surface area of the char influences the reaction rate of the oxidation. The more surface area is available the more char will be oxidized.

On the other hand the circulating bed material transports the heat from the combustion reactor to the gasification reactor. So, the recirculation rate has a massive influence on the operation behavior of a DFB system and the temperature levels within the system. Therefore, its prediction is an important issue and it has to be predicted accurately in a simulation of a DFB system.

As it was already pointed out, the choice of the drag law can influence the simulation results to a great extent. It determines the quality of the predictions of pressures and bed material distribution within in the system and also the bed material recirculation rate.

Also for the simulation of the commercial plant the following drag laws were tested: EMMS, Ganser, Turton-Levenspiel and Wen-Yu/Ergun.

The bed material recirculation rate was obtained similar as in the simulation of the Güssing cold flow model. The time integrated particle mass through the chute was differentiated and then averaged.

Figure 4.21 shows the calculated bed material recirculation rates for the different drag laws EMMS, Ganser (GA), Turton-Levenspiel (T–L) and Wen-Yu/Ergun (W–Y/E). The typical value for the Güssing commercial plant was obtained via mass and energy balances from a process simulation.
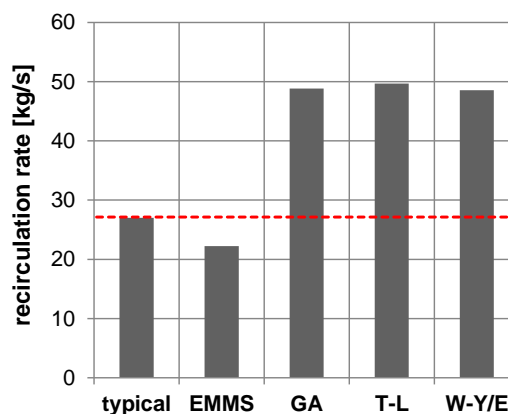


**Figure 4.21:** *Calculated bed material recirculation rates.  GA ...  Ganser, T–L ...  Turton-Levenspiel, W–Y/E ... Wen-Yu/Ergun.*

The EMMS drag model underestimates the typical value for the recirculation rate by about 18%. The other three drag models overestimate the typical value of the Güssing commercial plant by about 80%.

Based on this investigation the EMMS drag law was chosen to be best suited for further simulations. Therefore, all the results presented in the following for the Güssing commercial plant are conducted with the EMMS drag law.

## 4.5.2 Fluidization regimes

Figure 4.22 shows the whole DFB system of Güssing plant. The particles are colored according to the particle volume fraction. The colors at the left side indicate the packing density. If the particles are colored red they are near close pack ($\varepsilon_p \rightarrow \varepsilon_{cp}$), if they are blue a more dilute flow occurs ($\varepsilon_p \rightarrow 0$).

In the gasification reactor a bubbling bed occurs in the simulation what is in agreement with the experience and also plausible since olivine is a group B particle according to Geldart's classification [30]. In the bed bubbles are visible (referred to as "bubbling bed" in Figure 4.22). Furthermore, a characteristic splash zone forms at the top of the bed where the bubbles erupt and the particles are somewhat splashed into the freeboard. Also this behavior is to be expected.

It can be seen in the chute a moving bed occurs and also in the loop seal a bubbling bed forms. In the combustion reactor a transporting fluidized bed occurs which ensures that the bed material is circulating in the DFB system. In the cyclone the particles are separated from the gas flow. These flow behavior is to be expected and is plausible in qualitative terms.

In the experiments at the top of the moving bed in the chute always a less dense region was observed. The simulation was also able to predict this behavior, which can be seen in Figure 4.22. The particles in the upper section of the chute are colored yellow to green, indicating a bed which is not in close pack.

It can also be seen in the combustion reactor that a denser zone forms at the bottom. Such behavior is qualitatively expected for a fast fluidized beds [197]. This can also be seen in Figure 4.23 where the average particle volume fraction is depicted in a contour plot. Purple colors indicate that the particles are in close pack, which is the case for the packing density of the particles in the chute. In the region where the bed material enters the combustion reactor from the chute a denser region forms indicated by red and yellow colors ($\varepsilon_p \sim 0.3$ to $0.35$).

In the region where the riser expands to a larger diameter also a denser region at the
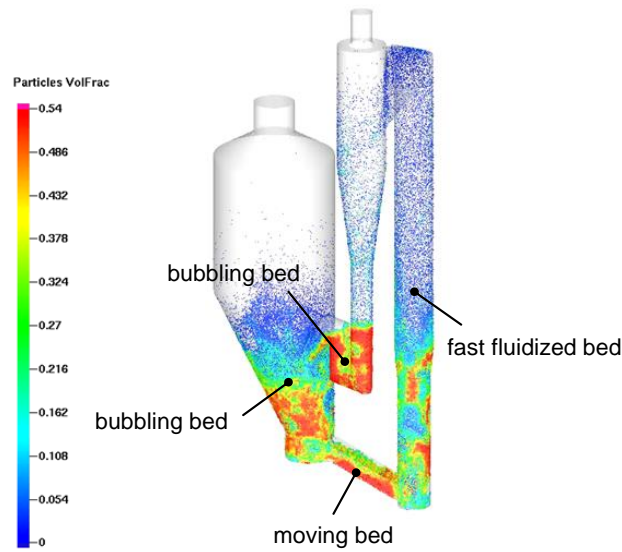
**Figure 4.22:** *Particle volume fraction in the whole system of the commercial plant.*

wall region can be observed. This could also be seen in the simulations of the cold flow model as discussed in section 4.4. With increasing height the particle volume fraction decreases and a dilute gas-solid flow occurs, also indicated by blue colors.

### 4.5.3  Pressure drops

The correct prediction of pressure drops over gasification and combustion reactor serves also as a hydrodynamic validation whether the simulation is able to predict the distribution of bed material within the system. As previously mentioned the pressure drop is a measure of the amount of bed material between two heights: $\varepsilon_p \sim \frac{1}{\rho_p g} \nabla p$.

Figure 4.24 shows the measured and calculated pressure drops over the gasification and the combustion reactor, respectively. It can be seen that the EMMS drag law is able to reproduce accurately the pressure drops in both reactors. The relative deviation is in a low percent range.

No pressure measurements were available over the height of the combustion reactor therefore the calculated pressure profile could not be compared to experimental values as it was the case for the cold flow model simulations, section 4.4.

### 4.5.4  Temperatures inside the system

Temperatures are a measure for the sensible energy content of a flow. Therefore, calculation of the temperatures inside the DFB system are a method for validation if the
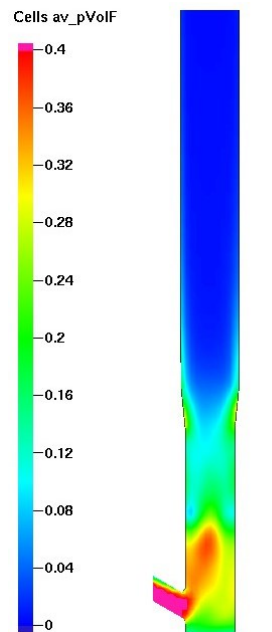
**Figure 4.23:** *Average particle volume fraction in the combustion reactor.*

reaction rates work and the right amount of heat is released or consumed. The temperatures are averaged between 100 and 150 s to get a meaningful mean value which can be compared to operational data.

The temperatures at the following positions are compared between the simulation and the commercial plant and are used for validation of the model:

- in the bed and freeboard of the gasification reactor

- in the upper section of the combustion reactor

- at the exit of the cyclone

- at the bottom of the loop seal

As it can be seen from Figure 4.25 the simulation is able to predict all the measured temperatures with relative deviations in a low percent range. As in the commercial plant also the temperature in the freeboard is slightly lower than in the bed due to heat loss. Furthermore, the increase in temperature in the combustion reactor can be seen in the simulation. This implies that the oxidation reactions in the combustion reactor give accurate reaction rates and heat releases.

Also the temperature difference between the gasification and the combustion reactor is predicted by the simulation showing that there are endothermic reactions ongoing in
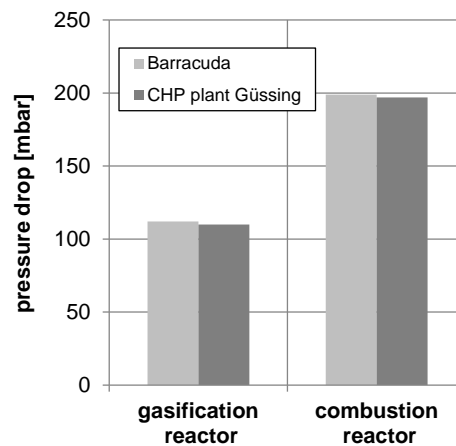
**Figure 4.24:** *Measured and calculated pressure drop over gasification reactor and combustion reactor.*
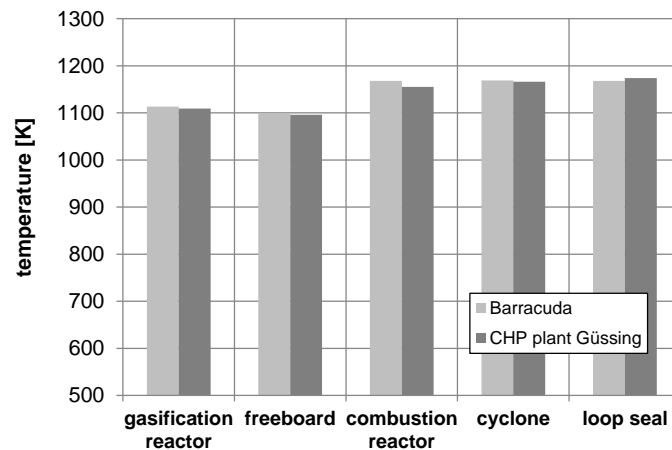


**Figure 4.25:** *Measured and simulated time-averaged temperatures in the system.*

the gasification reactor. In the present simulation the heat consumption is mostly due to the strongly endothermic water evaporation and slightly endothermic devolatilization reactions. These are strictly speaking no reactions but have to be implemented as such in the Barracuda simulations.

## 4.5.5  Composition of product and flue gases

In this section the simulated product and flue gas compositions with Barracuda are compared to data from the commercial plant operation and process simulation calculations. The composition of the product gas was measured from real operation in the Güssing plant. The flue gas composition was not measured but calculated with a pro-
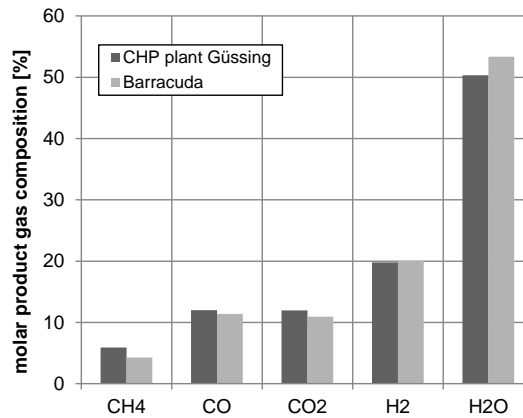
**Figure 4.26:** *Comparison between simulated and measured compositions of the wet product gas [6].*
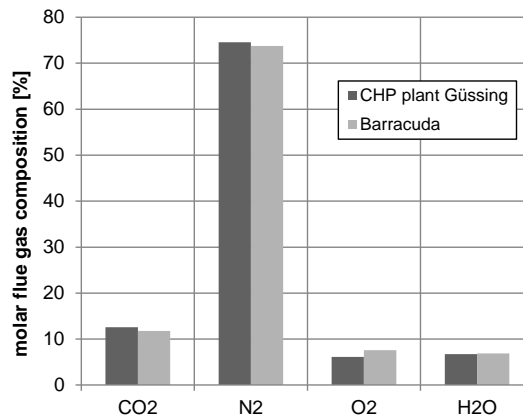


**Figure 4.27:** *Typical molar composition of the flue gas compared with time-averaged values calculated by Barracuda.*

cess simulation of the whole plant. In both the following diagrams also time-averaged values were used.

Figure 4.26 shows the Barracuda results of the wet product gas composition compared to typical values in the DFB plant in Güssing according to Kirnbauer et al. [6]. The values are given in mole percent. As it can be seen the simulated values are in good agreement with the measured data.

For the flue gas exiting the cyclone results from process simulations were used. The results from Barracuda agree well with the data obtained by process simulation, Figure 4.27. Furthermore, the $O_2$ content shows that also the right amount of char is burnt in the combustion reactor if one supposes that fly char, RME and recycled product gas are fully oxidized.

## 4.5.6 Summary and discussion

In this section simulation results and their validation of the commercial plant in Güssing were presented.

The best estimation of the recirculation rate gives the EMMS drag model, the other drag models produce relative deviations of up to 80% which is very high for good predictions of the hydrodynamic behavior. Liu et al. [51, 174] modeled a full loop of a DFB system. They used the Wen-Yu/Ergun drag model but did not give an estimation based on balance equations of the recirculation rate in their reactor. Therefore, no comparison can be made regarding the quality of the prediction of the different drag laws between the results in this and their work.

The simulation model was able to predict correctly the different fluidization regimes in simulated DFB system and the pressure drops were calculated accurately compared to the operational data. The relative deviations were in a low percent range which is an excellent agreement for gas/solid simulations. It indicates that the amounts of the particles are distributed correctly within the system.

Furthermore, the simulation correctly predicted measured product gas compositions. The composition of the flue gas, exiting the cyclone, which was obtained by mass balances with process simulation was also correctly predicted. This implies that a correct amount of char was burnt in the combustion reactor.

Temperatures were also predicted correctly by the simulation. The temperature increase in the combustion reactor was correctly predicted which indicates that the oxidation reactions in the combustion reactor release the right amount of heat.

It can be concluded that the model has sufficient accuracy for further simulations and investigations. These are performed in chapter 6.

# 5 Investigation of fuel mixing in DFB systems by means of cold flow modeling

In this chapter the idea and design of the cold flow model is presented. First, the requirements on the cold flow model are discussed. The calculations are based on Glickman's simplified similarity set. Later a detailed description of the relevant parts of the cold flow model is given including geometry and basic design data. The function principle of the cold flow model is given.

In the second part experimental results are given. The char concentration in the recirculating stream was investigated based on various parameters: superficial velocity, bed material recirculation rate, char concentration, bed height.

## 5.1 Design of the cold flow model

In this section the whole design process of the cold flow model is described. First, the requirements and the purpose of the cold flow model are presented. Then the scaling calculations are carried out to obtain the right dimensions of the bed, diameters for the particles, recirculation rates and fluidization velocities.

Next the design and construction of the specific parts of the cold flow model are described. For each of the core components of the cold flow model relevant design parameters, dimensions and functions are given.

### 5.1.1 Requirements of the cold flow model

Up to now the char hold-up in the gasification reactor and also the char concentration in the recirculating bed material are not known. The amount of char in the recirculating bed material stream is difficult to obtain by CPFD Barracuda simulations since the

movement of the char depends on the assumptions of the model. And no validation of the simulation results would be possible.

The following requirements have to be ensured in the cold flow model.

- **Same fluidization condition as in the gasification reactor of the commercial plant.** The Güssing plant is the basis for the investigations. Therefore, as a first step the hydrodynamic similarity of the behavior of the bed material in the cold flow model has to be ensured as close as possible to the bed material movement in the commercial plant. By applying scaling criteria this can be achieved.

- **Similar behavior of the binary bed.** In the Güssing commercial plant a fluidized bed consisting of multiple particle species exist. In this work the behavior of the char and biomass is investigated. Therefore, it has to be properly scaled to ensure hydrodynamic similar behavior close to the ongoing mixing and segregation processes in the commercial plant.

- **Bed material recirculation.** The investigation of the char in the recirculating stream is the main purpose of the cold flow model. Thus, and because also in the Güssing plant a recirculation stream exists such has to be implemented also in the cold flow model. Furthermore, in that part particle backflow should be inhibited to avoid segregation or accumulation processes which could distort the results.

- **Ability of controlling the bed material recirculation rate.** As mentioned earlier, the air staging in the combustion reactor significantly influences the bed material recirculation rate. For the planned experiments the recirculation rate should be controlled independently from the air flows.

- **Sampling during operation.** To account for sampling, an appropriate possibility of removing the bed material has to be installed. Sampling should be possible during operation without a shutdown of the operation.

Since fundamental investigations were carried out, a rectangular shape of the fluidization reactor was chosen because of construction and application reasons. It should be possible to make adaptions of the fluidization reactor. Thus, a slope for further mixing experiments or also an extension of the bed cross section area can be implemented. For the control of the recirculation rate a rotary valve was used since it is an established

way to set or extract fixed amounts of powder, as e.g. done in the pharmaceutical industry. Furthermore, it is able to act as a pressure seal between different parts of the cold flow model.

The transportation device for the bed material in upwards direction and to close the recirculation loop a pneumatic conveyor was designed. Screw conveyors would be an option but for binary mixtures backflow and segregations processes could occur which is not acceptable for the present case. Particle separation was carried out with a cyclone which was often used with success in cold flow models at TU Wien [20, 198, 1].

Between the cyclone and the fluidization reactor a loop seal was implemented to close the recirculation loop. The connection between loop seal and gasification reactor was chosen as the best spot for the sampling. The connection can be constructed with a flexible tube which can be easily disconnected and bed material can be extracted. Therefore, the air flows and the rotary valve do not have to be shut down for sampling but can continue in operation. A high frequency of sampling is thus ensured.

## 5.1.2 Scaling of the cold flow model

For the current design process the simplified set of similarity rules by Glicksman [66] was used since the full set only allows one scaling factor based on the present gas and particle species.

The gasification reactor of the Güssing reactor is used as a basis for the cold flow model. The simplified set allows to choose the scaling factor which was set to 1:12 in the present study.

For the scaling procedure with the simplified set, Eq. (2.42), the following values are given:

- hot or commercial plant (subscript c): $d_{p,c}$, $\rho_{g,c}$, $\mu_{g,c}$, $\rho_{p,c}$

- cold flow model (subscript m): $\rho_{g,m}$, $\mu_{g,m}$

- scaling factor

The subscript $c$ stands for the hot commercial plant and $m$ stands for the cold flow model.

In the following the used calculation procedure is shown which is based on Yang [199].

The required density of the bed material in the cold flow model $\rho_{p,m}$ is calculated as follows:

$$\frac{\rho_{g,m}}{\rho_{p,m}} = \frac{\rho_{g,c}}{\rho_{p,c}} \tag{5.1}$$

From the equality of the Froude numbers the superficial velocity in the cold flow model can be calculated:

$$\frac{u_{0,m}^2}{g L_m} = \frac{u_{0,c}^2}{g L_c} \rightarrow u_{0,m} = u_{0,c} \left(\frac{L_m}{L_c}\right)^{1/2} \tag{5.2}$$

$L_m$ and $L_c$ are characteristic length scales for the cold flow model and the commercial plant, respectively.

For the calculations the velocity at the bed surface in the commercial plant was used. The bed height was estimated according to the simulations of the commercial plant in section 4.3. The superficial velocity was calculated based on the assumption that all the moisture and volatiles were released into the gas phase latest at that point. This estimate is in good agreement as it can be seen from the Barracuda simulations in Figure 6.5 (a). Table 5.1 shows the results of the calculations.

**Table 5.1:** *Calculation of the superficial velocity for the Güssing reactor.*

| parameter | bed surface |
|---|---|
| $d_{bed}$ [m] | 1.65 |
| $A_{bed}$ [m$^2$] | 2.14 |
| $u_0$ [m/s] | 1.11 |

With the superficial velocity the minimum fluidization velocity of the cold flow model, $u_{mf,m}$, can be calculated.

$$\frac{u_{0,m}}{u_{mf,m}} = \frac{u_{0,c}}{u_{mf,c}} \rightarrow u_{mf,m} = u_{mf,c} \frac{u_{0,m}}{u_{0,c}} = u_{mf,c} \left(\frac{L_m}{L_c}\right)^{1/2} \tag{5.3}$$

The particle diameter for the bed material in the cold flow model is the corresponding diameter to the calculated $u_{mf,m}$. To calculate the minimal fluidization velocity the correlation of Grace [33] is used:

$$Re_{p,mf} = \frac{u_{mf} d_p \rho_g}{\mu_g} = \sqrt{27.2^2 + 0.0408\,Ar} - 27.2 \tag{5.4}$$

Scaling of the bed material recirculation rate gives

$$\frac{\dot{m}_{rec,m}}{\dot{m}_{rec,c}} = \frac{\rho_{p,m}}{\rho_{p,c}} \frac{u_{0,m}}{u_{0,c}} = \frac{\rho_{p,m}}{\rho_{p,c}} \left(\frac{L_m}{L_c}\right)^{1/2} \tag{5.5}$$

For the design calculations the values shown in Table 5.2 are used. Note that also the results from the calculations are shown.

**Table 5.2:** *Used design values for the cold flow model.*

|  | **Güssing** | **cold flow model** |
|---|---|---|
| $d_p$ [μm] | 510 | 118 |
| $\rho_p$ [kg/m³] | 2800 | 8750 |
| $\phi_p$ [−] | 0.93 | 1 |
| $\rho_g$ [kg/m³] | 0.208 | 1.17 |
| $\mu_g$ [kg/m s] | $4.20 \cdot 10^{-5}$ | $1.82 \cdot 10^{-5}$ |
| $u_0$ [m/s] | 1.11 | 0.32 |
| $u_{mf}$ [m/s] | 0.127 | 0.0489 |
| $\dot{m}_{rec}$ [kg/s] | 27 | 0.30 |
| $d_{bed}$ [m] | 1.65 | 0.12 |

The diameter of the bed material particles and the properties for the hot product gas of typical composition are taken from Kirnbauer et al. [6]. The density of the bed material particles as well as the sphericity are taken from Bosch [20]. The properties of the air are calculated according to VDI-Wärmeatlas [29]. $d_{bed}$ is the diameter of the conical reactor at the bed surface and is estimated from the operating conditions.

The scaling procedure would give a density for the bed material of about 15,700 kg/m³. Bronze is chosen since it has a high density and was also often used in cold flow model studies, e.g. [21], [198], [1]. The scaling procedure gives a mean particle diameter of $d_p$ = 101 μm. Bronze was only available in a PSD with a mean diameter of $d_p$ = 118 μm. For the experiments this was considered to be close enough to the value from the scaling calculations. Later it is shown that the absolute relevant deviations in relevant dimensionless numbers are around 20% or lower. The calculated and used values for the cold flow model in this study are given in Table 5.2.

Dimensionless numbers can be used to determine the degree of agreement between the values for the hot and cold conditions. If relevant dimensionless numbers match hydrodynamic similarity between the cold flow model and the commercial plant is more likely.

Since not the exact values can be used as calculated (density and diameter of the

bed material) a deviation occurs in these numbers. To give an estimate the following numbers were used: $Fr_p$, $Re_p$, $\frac{\rho_p}{\rho_g}$, $\frac{u_0}{u_{mf}}$, $Ar$, $U^*$ and $d_p^*$.

$Fr_p$, $\frac{\rho_p}{\rho_g}$ and $\frac{u_0}{u_{mf}}$ occur in the simplified set by Glicksman. $Fr_p$ and $\frac{\rho_p}{\rho_g}$ also appear in Reh's [67] consideration. Reh also uses the Reynolds number, $Re_p$, which is also included in the full set [65]. $U^*$ and $d_p^*$ are the parameters in the dimensionless regime diagram by Grace [68].

If these numbers are calculated with the used solids diameter and density, $d_p = 118$ μm and $\rho_p = 8750$ kg/m$^3$, are compared to the numbers obtained for the commercial plant the results shown in Table 5.3 are obtained.

Relative deviations between the cold flow model and the commercial plant were calculated as follows:

$$rd = \frac{x_{model} - x_{commercial}}{x_{commercial}}, \tag{5.6}$$

where $_{model}$ and $_{commercial}$ mean values from the cold flow model and the commercial plant, respectively. If the values from the DFB plant are overestimated, $rd > 0$. If the values calculated for the cold flow model are smaller, $rd < 0$.

**Table 5.3:** *Comparison of relevant dimensionless numbers.*

|  | **Güssing** | **cold flow model** | $rd$ |
|---|---|---|---|
| $Fr_p$ | 0.077 | 0.088 | 0.146 |
| $Re_p$ | 2.81 | 2.43 | −0.135 |
| $\rho_p/\rho_g$ | 13,442 | 7485 | −0.443 |
| $u_0/u_{mf}$ | 8.8 | 6.6 | −0.253 |
| $Ar$ | 430 | 498 | 0.158 |
| $U^*$ | 0.373 | 0.307 | −0.176 |
| $d_p^*$ | 7.55 | 7.92 | 0.050 |

From Table 5.3 it can be seen that the dimensionless numbers are in good agreement, relative deviations are in the range of about 20%. However, the deviation for the density ratio is much larger due to the reasons mentioned above. Therefore, it is assumed that the fluid mechanics between the cold flow model and the commercial plant will be similar.

Since also char will be used in the experiments it has to be scaled in an appropriate way. In this work as scaling criterion the ratios of the diameters and densities of the char and the bed material were kept constant:

$$\frac{d_{p,char}}{d_{p,bed}} \qquad \text{and} \qquad \frac{\rho_{p,char}}{\rho_{p,bed}} \tag{5.7}$$

## 5.2 Description of relevant parts of the cold flow model

### 5.2.1 Fluidization reactor

Figure 5.1 shows the full and a cutaway view of the gasification reactor. The cross section area of the fluidization reactor is of a rectangular shape. By using plates it can be divided in three sections. In this work only the one closest to the outlet to the upper chute was used.
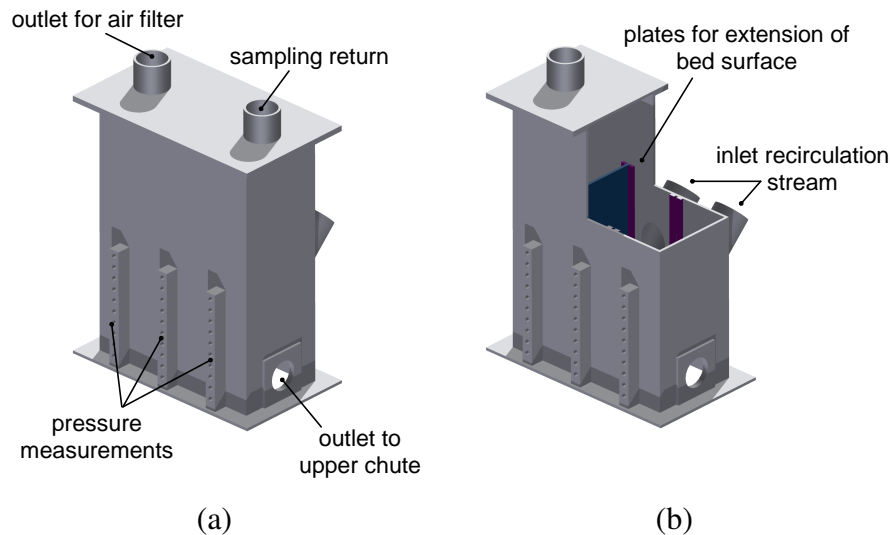


**Figure 5.1:** *Fluidization reactor of the cold flow model. (a) ... full view, (b) ... cutaway view.*

Each chamber's dimensions are $0.10 \times 0.15$ m$^2$. The hydraulic diameter corresponds to the scaled bed diameter. The height of the fluidization reactor is about 0.5 m. The fluidization air is fed from the bottom. Each chamber is fluidized with 12 nozzles with a 1/8" inlet. The nozzles are protected by of metal wire to prevent the bed material from flowing back into the air supply tubes.

At the front wall threaded holes are provided for pressure measurements. 10 holes are implemented over the height for each chamber. The diameter of the outlet of the bed material is 0.052 m in diameter. The cross section area of the outlet tube can be varied with a gate valve (not shown in Figure 5.1). In this work the outlet was closed by half, thus only the lower half of the outlet was used.

Two outlets at the top exist. One is used for the outflow out the fluidization air, which then flows to an air filter to remove fines from particle abrasion. The other one is used as sampling return to fed back the extracted bed material after sampling.

After the experiments with polyethylene particles the cold flow model the design of the gasification reactor was altered to investigate the influence of the slope on the fluidization behavior.

Therefore, a slope was implemented which is based on the design of commercial DFB plants. The alteration was made for further investigations regarding scale-up and design considerations. A schematic drawing of side view is shown in Figure 5.2. Experimental results on that are found in section 6.4.
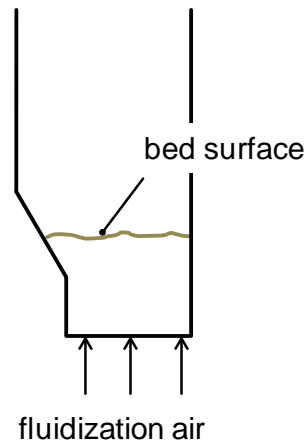


**Figure 5.2:** *Changed design of the fluidization reactor.*

The cross section area at the bottom is the same as previously mentioned ($0.10 \times 0.15$ m$^2$). The slope is provided with nozzles to enable fluidization.

## 5.2.2 Rotary valve

The used rotary valve is from Schäffer Verfahrenstechnik. It is driven with an electric engine with 0.25 kW. The rotary valve is operated with a frequency converter and a potentiometer to be able to control the speed.

The rotary valve was calibrated and a correlation between the speed and the throughput of the rotary valve was established. The calibration curve of the rotary valve is depicted in Figure 5.3.

For the calibration the fluidization reactor was first filled with bronze. Then the system was emptied by using the rotary valve with different speeds. The necessary
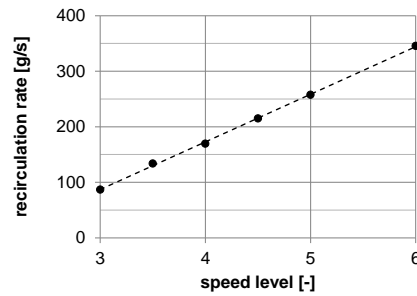
**Figure 5.3:** *Calibration curve of the rotary valve.*

time was measured and divided by the whole mass, which was transported through the rotary valve. For the relevant speed levels the equation to calculate the bed material recirculation rate is

$$\dot{m}_{rec}\ [\text{g/s}] = n_{Speed} * 85.7 - 170 \tag{5.8}$$

The calibration curve is valid for speeds between 3 to 6, the calculated bed material recirculation rate ($\dot{m}_{rec}$) is given in g/s.

### 5.2.3  Riser

In the cold flow model the riser works as pneumatic conveyor and is operated at a condition with $u_0 > u_t$. Therefore, a sufficient high superficial velocity has to be ensured. The Grace diagram can be used for estimating the operation conditions for the riser. According to the particle size distribution of the bronze, Figure 5.9, the largest particle diameter is about 150 µm. Therefore, this diameter is used to calculate the riser operating conditions.

Table 5.4 shows the calculated values for the design of the riser. $U^*$ is chosen as the upper limit of the fast fluidization range. For the used tube with a inner diameter of $d_{i,riser} = 52$ mm a volume flow of about $\dot{V}_{req} = 72$ Nm$^3$/h is necessary according to the calculations.

In the experiments the experience was gained that a volume flow of $\dot{V} = 50$ Nm$^3$/h is sufficient to ensure pneumatic conveying and to guarantee particle transport without backflow.

**Table 5.4:** *Calculation data for the riser of the cold flow model.*

| parameter | value | dimension |
|-----------|-------|-----------|
| $d_{p,max}$ | 150 | μm |
| $u_t$ | 2.56 | m/s |
| $d_p^*$ | 10.1 | [-] |
| $U^*$ | 8 | [-] |
| $d_{i,riser}$ | 52 | mm |
| $u_{0,req}$ | 10.5 | m/s |
| $\dot{V}_{req}$ | 72.4 | Nm$^3$/h |

## 5.2.4  Cyclone

After the pneumatic conveyor the bed and char particles have to be separated from the air stream. Based on the data of the rotary valve and the design of the pneumatic conveyor the cyclone for that task was calculated and designed according to Zogg [200].

A 3D plot of the cyclone is shown in Figure 5.4. The basic dimensions of the used cyclone are given in Table 5.5.
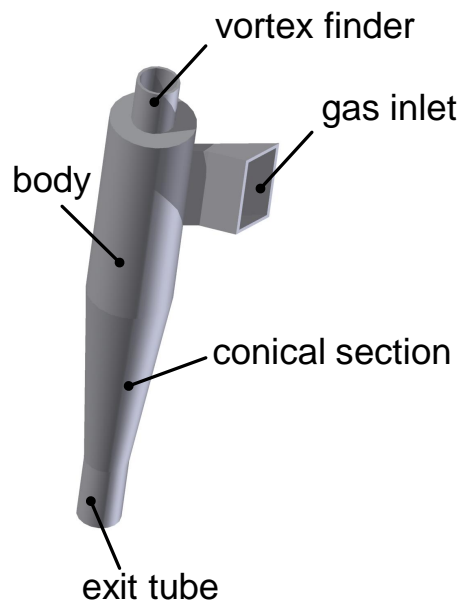


**Figure 5.4:** *Drawing of the cyclone.*

Based on a volume flow of 50 Nm$^3$/h the efficiency of the cyclone is almost 100%. The mass of the bronze exiting the cyclone after several hours of operation is in the range of grams. Therefore, the bed material loss during the experiments does not need

to be considered.

**Table 5.5:** *Basic dimensions of the used cyclone.*

| parameter | value | dimension |
|---|---|---|
| total height | 0.6 | m |
| height of conical section | 0.3 | m |
| body diameter | 0.11 | m |
| diameter of vortex finder | 0.052 | m |
| length of vortex finder | 0.026 | m |
| diameter of exit tube | 0.052 | m |
| dimensions gas inlet | $0.018 \times 0.12$ | m |

## 5.2.5  Loop Seal

The loop seal in the Güssing cold flow model and commercial plant is of U-shape, as it can be seen in Figure 4.2. Peining et al. [201] investigated the flow characteristics in various types of loop seals and found that a N-shape loop seal performs best regarding throughput.

To allow great flexibility regarding throughput and bed material recirculation rates these findings were also considered for the design of the loop seal. Thus, highest throughput is ensured. Figure 5.5 shows the drawing of the loop seal. The air is fed at the bottom side via three 1/4" nozzles.
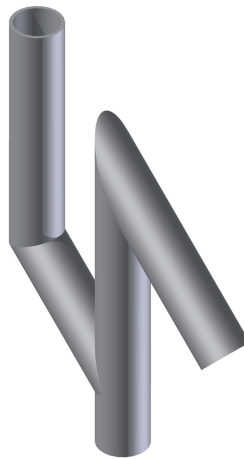


**Figure 5.5:** *Design of the used loop seal.*

To ensure high throughput through the loop seal and sufficient bubbling behavior of the bed the air supply was designed to be able to reach a fluidization number of

around 6. Since the loop seal consists of two legs the cross section area has to be taken double the size of the inner diameter of the tube. Table 5.6 summarizes the calculated conditions for the loop seal.

**Table 5.6:** *Calculated data for loop seal*

| parameter | value | dimension |
|-----------|-------|-----------|
| $d_{i,loop\ seal}$ | 0.052 | m |
| $FN$ | 6.2 | [-] |
| $\dot{V}$ | 3.0 | Nm$^3$/h |

The loop seal and the fluidization reactor are connected with a flexible tube. This flexible tube can be disconnected from the fluidization reactor and a sample can be taken. So, sampling can occur without any changes in the operational set-up meaning rotary valve speed and the fluidization of the cold flow model can remain constant.

## 5.3  Function principle and flowsheet

The cold flow model consists of the following parts which also correspond to the flow direction of the bed material stream:

- fluidization reactor

- upper chute

- rotary valve

- lower chute

- riser (pneumatic conveyor)

- cyclone

- loop seal

The flowsheet of the cold flow model is depicted in Figure 5.6. The cold flow model in reality is shown in Figure 5.7.

The fluidization reactor is operated in the bubbling bed mode. Via the air supply at the bottom several fluidization numbers can be operated. At the top the fluidization air
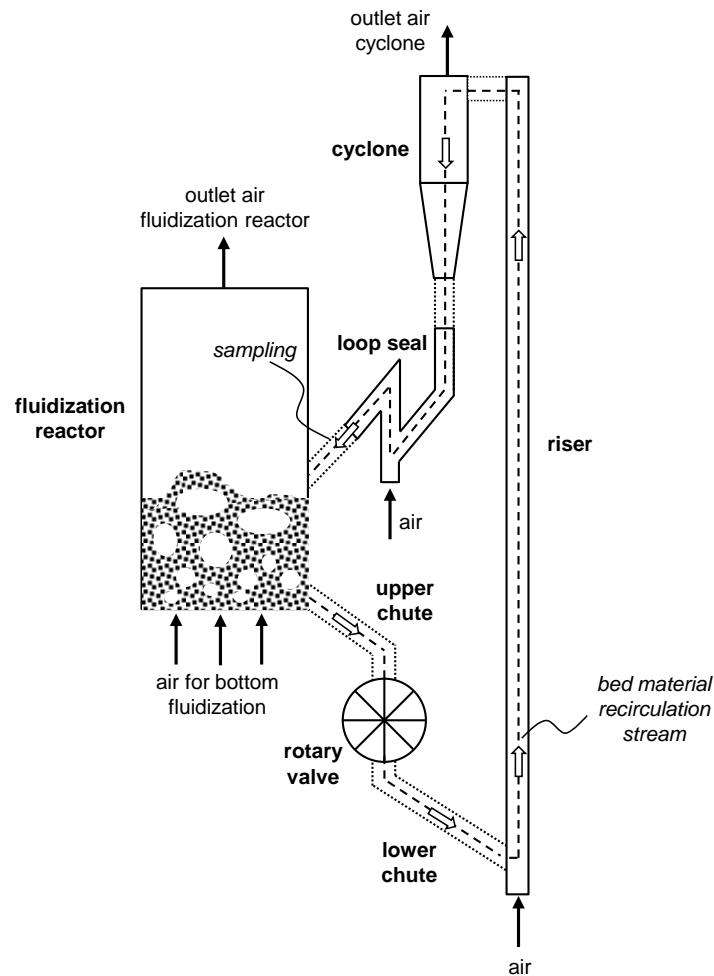
**Figure 5.6:** *Flow sheet of the cold flow model.*

leaves the fluidization reactor and flows through a filter to separate fines which arise from abrasion.

Via the outlet at the bottom of the fluidization reactor the solids stream is transported to the upper chute. The upper chute is filled with solids to enable a constant inlet stream into the rotary valve. The rotary valve controls the bed material recirculation stream.

Via the lower chute the solids stream flows to the riser where the solids are conveyed upwards pneumatically. At its top the solids stream enters the cyclone where the particles are separated from the gas flow.

The loop seal connects the cyclone to the fluidization reactor. Furthermore, the flexible tube between the loop seal and the fluidization reactor can be disconnected. It is possible to remove some recirculating solid for further investigation of the char concentration. Via a sampling return at the top of the fluidization reactor the samples
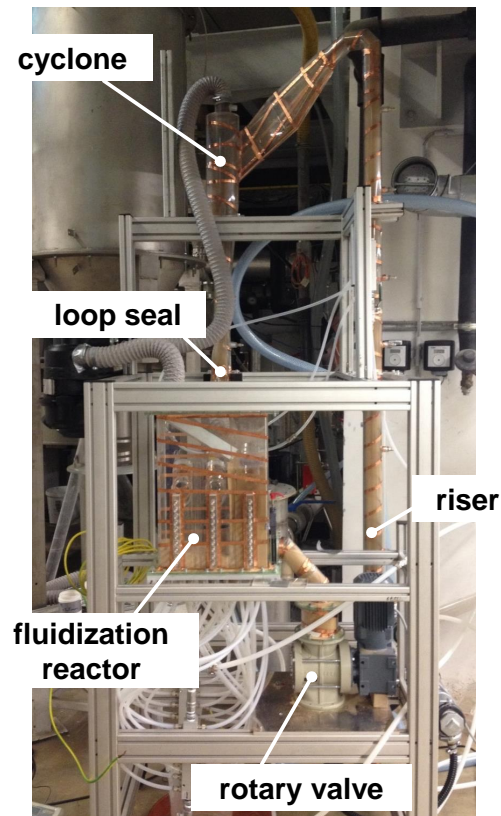
**Figure 5.7:** *Cold flow model.*

are fed back into the system.

The cold flow model is supplied with pressurized air at 9 bar from the pressurized air system at TU Wien. The air supply is shown in Figure 5.8.

## 5.4  Methodology

### 5.4.1  Particle species used in the experiments

As mentioned above bronze powder with a mean particle diameter of $d_p = 118$ µm was used. The particle size distribution is shown in Figure 5.9.

Furthermore, the other two used particle species were polyethylene (PE) and gravel. Table 5.7 shows the data for the used PE and gravel particles. PE was used to simulate the char movement in the system whereas gravel was used to simulate biomass.

If the ratios in Eq. (5.7) are applied to the used particle species, polyethylene and gravel, the corresponding values for the particle species in the commercial plant in
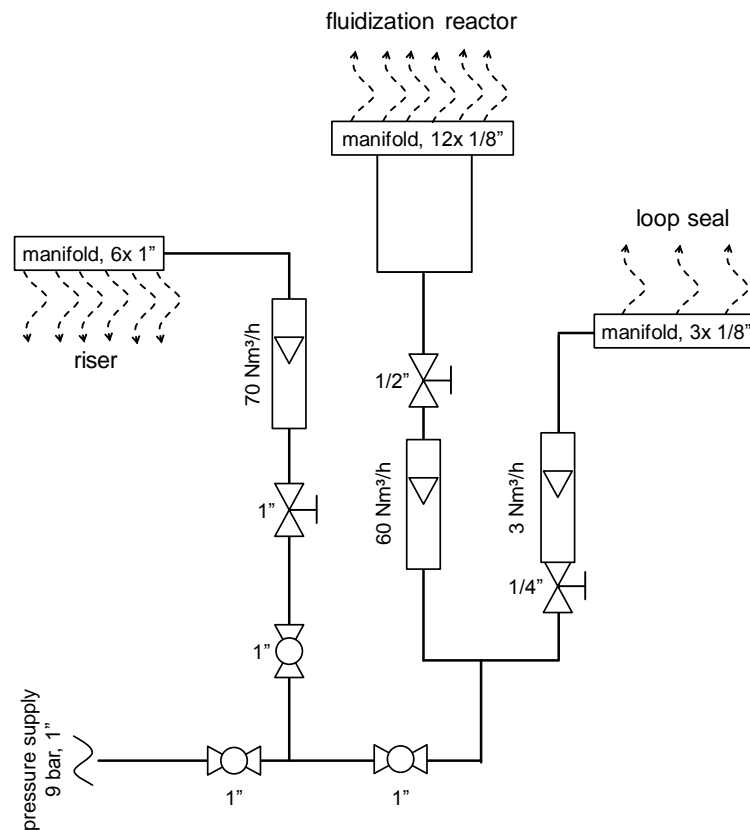
**Figure 5.8:** *Air supply of the cold flow model.*

**Table 5.7:** *Diameters and densities of the used polyethylene and gravel particles.*

|                     | PE        | gravel    |
|---------------------|-----------|-----------|
| $d_p$ [mm]          | 2.5–3.15  | 2.5–3.15  |
| $\rho_p$ [kg/m$^3$] | 930       | 2292      |

Güssing are obtained. The results are shown in Table 5.8. For the calculations the mean diameter of the used PE and gravel particles are used.

The diameters for the char and the biomass are in the range of 12 mm which is a typical size of the used wood, also in accordance with the PSD of wood shown in Figure 4.10.

The density of char is in the range of biomass chars as also mentioned in section 4.3.2. The density of the biomass corresponds to fresh and wet biomass which is of higher density as already dried wood.
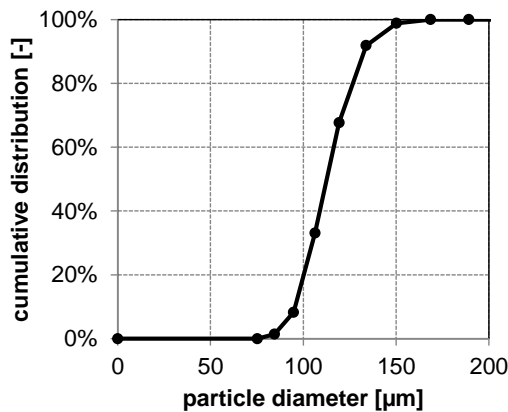
**Figure 5.9:** *Particle size distribution of the bronze powder used in this work.*

**Table 5.8:** *Corresponding values of the commercial plant in Güssing based on the used polyethylene and gravel in the experiments.*

|  | commercial plant | | | cold flow model | | |
|---|---|---|---|---|---|---|
|  | *bed material* | *char* | *biomass* | *bed material* | *PE* | *gravel* |
| $d_p$ [mm] | 0.510 | 12.2 | 12.2 | 0.118 | 2.83 | 2.83 |
| $\rho_p$ [kg/m$^3$] | 2800 | 298 | 733 | 8750 | 930 | 2292 |

## 5.4.2 Experimental procedure and data analysis

For the experiments the following parameters were used and varied:

- **Air flow rate in the fluidization reactor.** Volume flows of 9 to 24 Nm$^3$/h were used. This corresponds to fluidization numbers of $FN$ = 3 to 9. Typical fluidization numbers for the Güssing commercial plant are in the range of 7 to 9.

- **Bed material recirculation rate.** In the experiments three values for $\dot{m}_{rec}$ were used: 173, 258, and 344 g/s. Scaled values for the Güssing commercial plant is at about 300 g/s.

- **Char concentration in the system.** For the experiments three different char concentrations were used: 2, 4, and 6 wt.–% of char in the bed material. For the commercial plant there are no values from measurements. Singh et al. [14] gave values of around 5 wt.-% for combustors.

- **Bed height in the fluidization reactor.** In the experiments bed heights of 9, 11, and 13 cm at minimum fluidization conditions in the fluidization reactors

were used. A typical corresponding bed height at scaled conditions at which the commercial plant in Güssing is operated is then around 9 to 11 cm.

- **Density of the particles.** Experiments were conducted also with particles with higher density representing biomass in the system. The experiments were carried out at fluidization numbers and bed heights in the aforementioned range.

For better illustration the operating points and ranges can be depicted in Grace's diagram. Figure 5.10 shows the points of the operating conditions. The fluidization reactor is operated in a range of $FN = 3$ to 9, as previously mentioned. This corresponds to a vertical range in the diagram. To ensure sufficient throughput also the loop seal is operated in a medium bubbling range. In the riser a fast fluidized bed occurs and the particles are conveyed upwards.
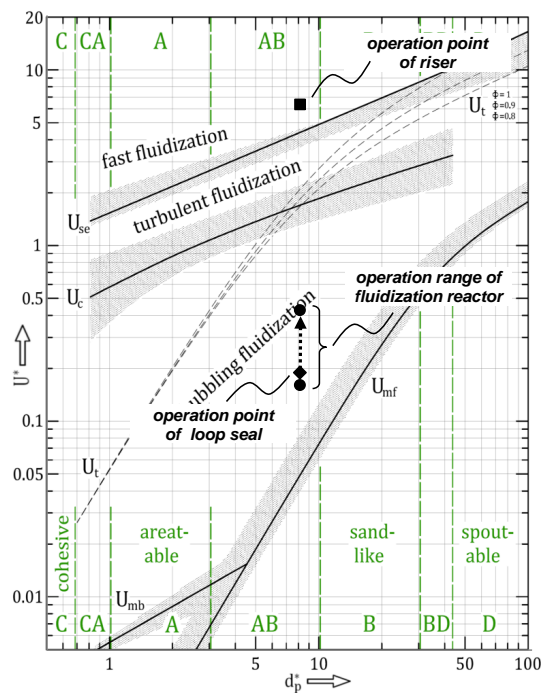


**Figure 5.10:** *Grace diagram with operating points.*

To investigate the char concentration in the bed material recirculation stream samples were extracted at the sampling point. Since the bed material and the char are of different size sieving is possible to separate them. The masses of the two species were recorded. Then the sample was fed back into the system. To ensure sufficient time for remixing and obtaining a steady state after the disturbance of the sampling 10 times the

residence time in the fluidization reactor was allowed to pass. Then the next sample was taken.

The char concentration in each sample was calculated as follows:

$$c_{char,i} = \frac{m_{char,i}}{m_{bed,i}}, \tag{5.9}$$

where $m_{char,i}$ and $m_{bed,i}$ mean the mass of the char and the bed material in the sample, respectively.

Fluidized beds show highly stochastic behavior. Therefore, for each operating point $n = 10$ experiments were carried out and a mean value, $\bar{c}_{char}$ was calculated:

$$\bar{c}_{char} = \frac{1}{n} \sum_i c_{char,i} = \frac{1}{n} \sum_i \frac{m_{char,i}}{m_{bed,i}} \tag{5.10}$$

In the following for each operating point in the experiments a mixing factor, $M$, is calculated:

$$M = \frac{\bar{c}_{char}}{c_{char,system}}. \tag{5.11}$$

$M$ can have values between 0 and 1. If $M = 0$ no char is found in the bed material recirculation stream, since $\bar{c}_{char} = 0$. The other border case $M = 1$ means that in the bed material recirculation stream is the same amount of char as on average in the whole system: $\bar{c}_{char} = c_{char,system}$.

For the experiments with gravel the same procedure for the experiments and the data analysis was used. The mixing factor is then calculated analogous: $M = \frac{\bar{c}_{gravel}}{c_{gravel,system}}$

## 5.5 Results

In this section the influence of various parameters on the char concentration in the bed material recirculation stream is investigated. Furthermore, experiments were carried out with gravel particles to simulate biomass.

The investigated parameters are the fluidization rate, the bed material recirculation rate, the char concentration in the system and the bed height in the fluidization reactor.

In the following diagrams on the abscissa the fluidization number, $FN = \frac{u_0}{u_{mf}}$ and on the ordinate the mixing factor, $M$, is shown. The curves will be drawn for one specific condition of the char concentration in the system, bed material height and bed material recirculation rate indicated by the scheme shown in Figure 5.11.
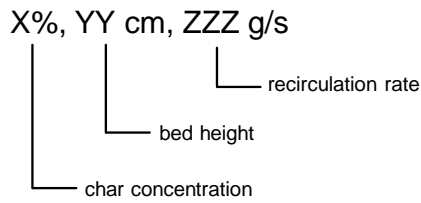
**Figure 5.11:** *Scheme for the conditions in the test runs.*

The investigated parameters in the experiments with gravel are the fluidization rate and the bed height. Its influence on the gravel concentration in the bed material recirculation stream is determined.

## 5.5.1 Influence of the fluidization rate

Bubbles are the main reason for mixing in fluidized beds. If the gas flow is fed into the bed at the bottom bubbles move upwards and erupt at the bed surface. In their wake they can transport jetsam particles also upwards in the bed. Therefore, one would assume that the mixing factor approaches 1 if the fluidization number is increased in the fluidization reactor.

Figure 5.12 shows the influence of the mixing factor of the fluidization number for the operation point of 2% total char concentration in the system, 9 cm bed height in fluidization reactor and a bed material recirculation rate 258 g/s.
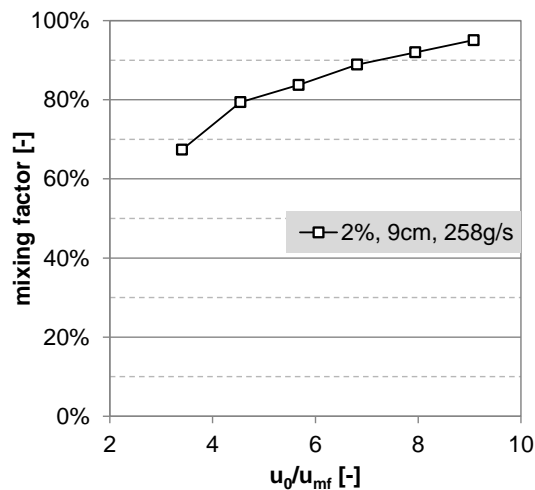


**Figure 5.12:** *Influence of fluidization rate.*

The mixing factor increases from slightly below 70% at the lowest fluidization number to about 95% for the highest fluidization number. This indicates that the char is bet-

ter mixed in the fluidization reactor at higher fluidization numbers which is in perfect agreement with the experimental evidence of previous studies as presented in chapter 3.

## 5.5.2 Influence of the recirculation rate

The influence of a higher recirculation rate is investigated in this section by using three different speeds of the rotary valve which corresponds to the following three mass flows: 173 g/s, 258 g/s, and 344 g/s.

In Figure 5.13 (a)–(c), the influence of the recirculation rate on the mixing factor is depicted for each the three char concentrations for 2%, 4%, and 6% dependent on the fluidization number $FN = u_0/u_{mf}$.

For all three concentrations the mixing factor increases with increasing bed material recirculation rate. This increase is more pronounced for the curve for 2% char. For higher concentrations (4% and 6%) the curves come closer together. This indicates that the influence of the recirculation rate on the mixing behavior is more pronounced at low bed material recirculation rates.

Although the curves come closer together with higher char concentration the absolute amount of char is still increasing since also the absolute amount bed material stream is increased. If the influence of the recirculation rate on the mixing factor is low at 6% char concentration the absolute amount of the char in the recirculation stream would still at least double since the recirculation rate is nearly doubled from 177 to 344 g/s.

Summing up the char concentration in the recirculation stream changes in two ways:

- On the one hand because the mixing factor increases due to higher recirculation rates.

- On the other hand because the absolute amount of bed material moving to the riser is increased and therefore also more char is transported.

## 5.5.3 Influence of char concentration in the system

In this section the influence of the char concentration on the mixing factor is shown, Figure 5.14 (a)–(c). In the experiments three concentrations of char in the system were tested: 2%, 4%, and 6%.
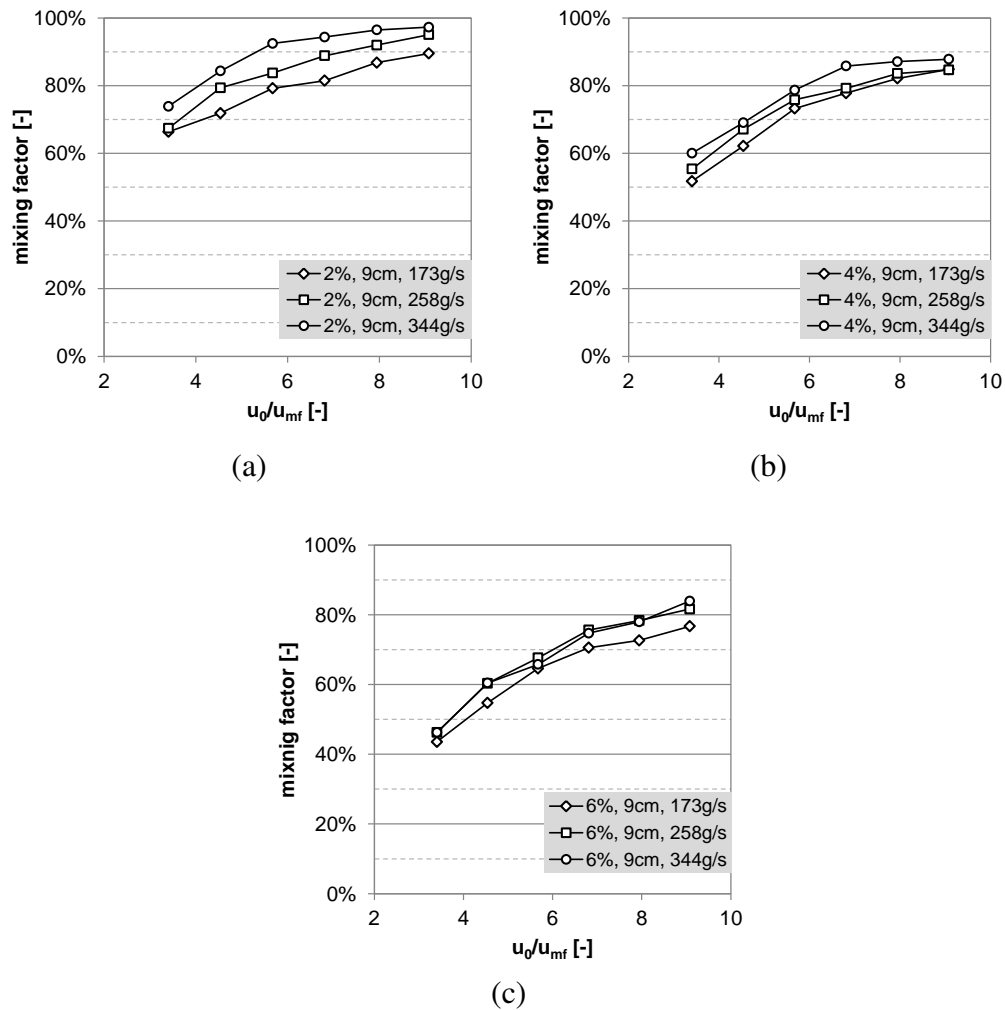
**Figure 5.13:** *Dependence of the mixing factor on the bed material recirculation rate. (a) ...* $c_{char,system} = 2\%$, *(b) ...* $c_{char,system} = 4\%$, *(c) ...* $c_{char,system} = 6\%$.

It should be noted that during these experiments the bed height in the fluidization reactor also increases even if the absolute bronze amount remains the same. Due to its low bulk density more char also causes the bed surface to rise.

It can be seen that the mixing factor decreases with increasing char concentration in the system. For 6% char concentration the mixing factor is mostly below 80% and exceeds that value only for high fluidization numbers or high fluidization rates. Furthermore, at low fluidization numbers the mixing factor sinks below 50%. Mixing factors of 90% and more are only possible for high fluidization numbers and high recirculation rates. The lowest values for the mixing factor are for 6% char concentration at low fluidization numbers and are only slightly above 40%.

The mixing factor decreases if the char concentration is increased in the system.
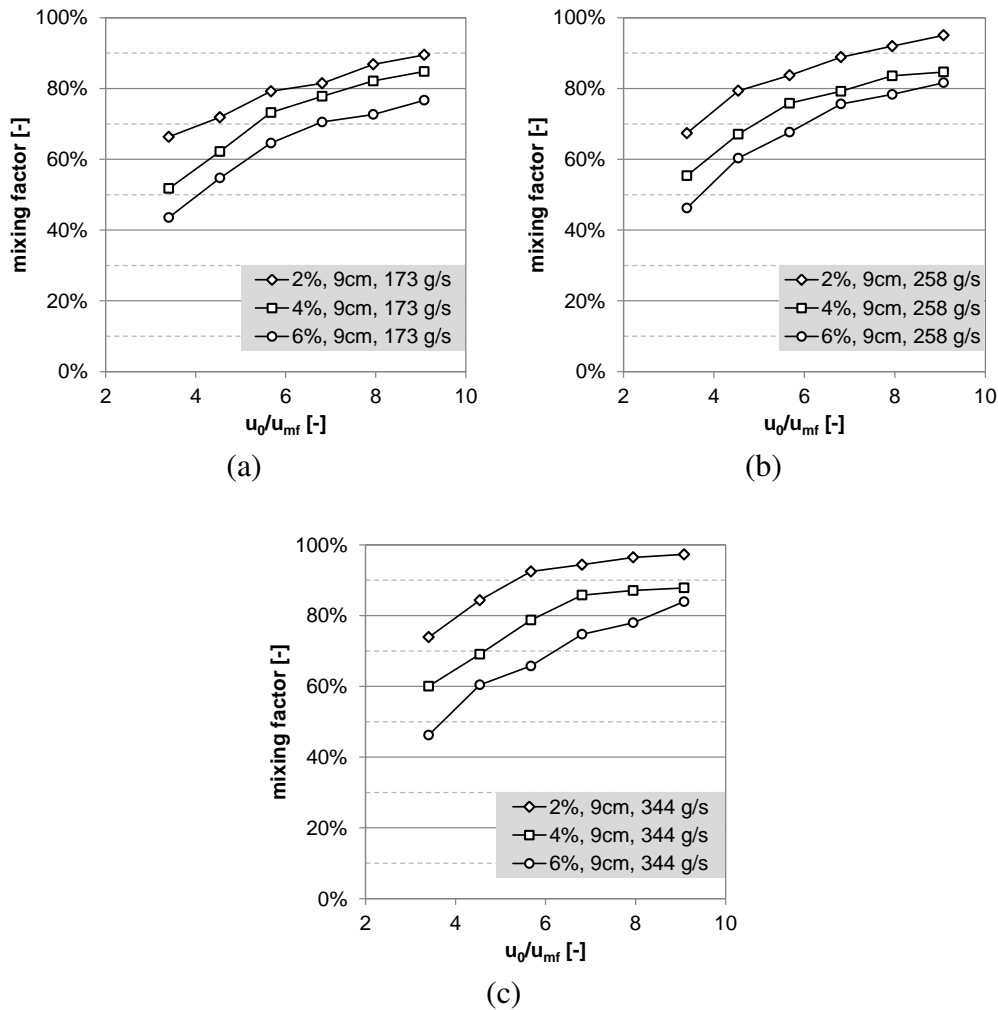
**Figure 5.14:** *Dependence of the mixing factor on the char concentration in the system. (a) ...* $\dot{m}_{rec} = 173$ *g/s, (b) ...* $\dot{m}_{rec} = 258$ *g/s, (c) ...* $\dot{m}_{rec} = 344$ *g/s.*

However, the absolute amount of char transported to the riser still increases. Figure 5.15 (a)–(b) shows that the absolute amount of char moving to the riser is increasing.

Figure 5.15 (a) shows the increase of the absolute amount of char to the riser if the char concentration in the system is increased from 2% to 4%. The dashed line marks the values if the measured 2% values are doubled. The same is shown in Figure 5.15 (b) for the increase of 2% to 6%. The solid line is obtained if the values for the 2% curve are tripled.

In both cases it can be seen that the extrapolated doubled or tripled values are is higher than the actual measured values. This indicates that a doubling or tripling of the char concentration in the system does not lead to a doubling or tripling in the recirculation stream if the amount of bed material is kept constant.

(a)  (b)
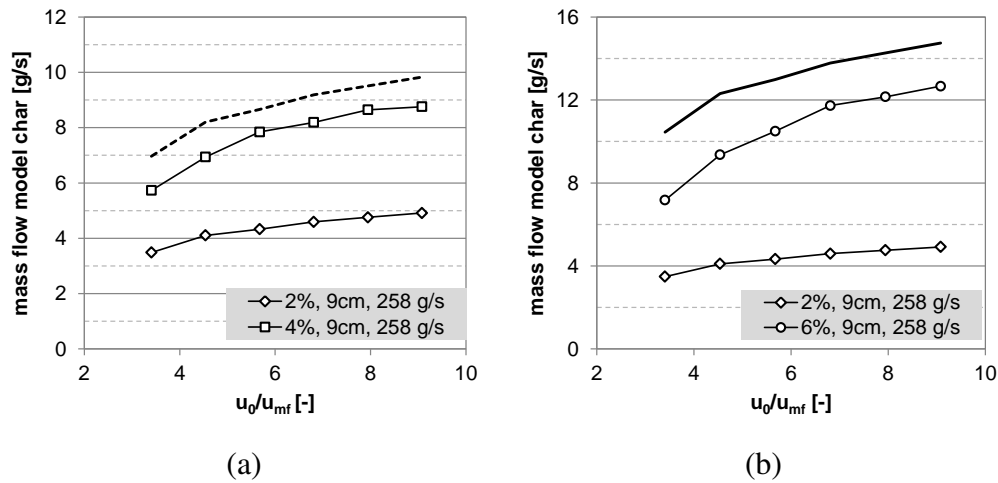
**Figure 5.15:** *Absolute amount of model char moving into the riser.*

## 5.5.4 Influence of bed height in the fluidization reactor

In the commercial plant the bed height in the gasification reactor is determined by how much bed material is used in the whole DFB system. In this section the results from the experiments are shown where the height of the bed in the fluidization reactor was varied. Three heights were investigated: 9, 11, and 13 cm. As mentioned earlier these heights refer to the height of the bronze alone in the fluidization reactor at minimum fluidization conditions

Figure 5.16 (a)–(b) shows the results for 4 and 6% of char in the system. In both cases the mixing factor decreases with increasing bed height.



(a)  (b)
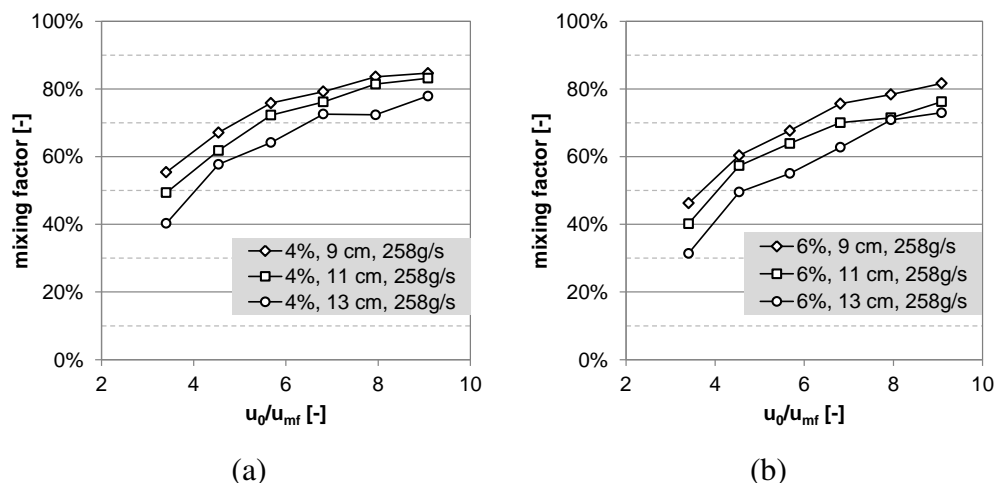
**Figure 5.16:** *Influence of the bed height. (a) ... $c_{char,system} = 4\%$, (b) ... $c_{char,system} = 6\%$.*

## 5.5.5 Experiments with gravel particles

Gravel is of much higher density than the used polyethylene particles which simulate the char. In the experiments the configuration with the slope was used. Figure 5.17 shows the mixing factor for three different fluidization numbers and two bed heights (11 and 13 cm). For the experiments the gravel concentration in the system was $c_{gravel,system} = 4\%$. The bed material recirculation rate was set to 258 g/s.
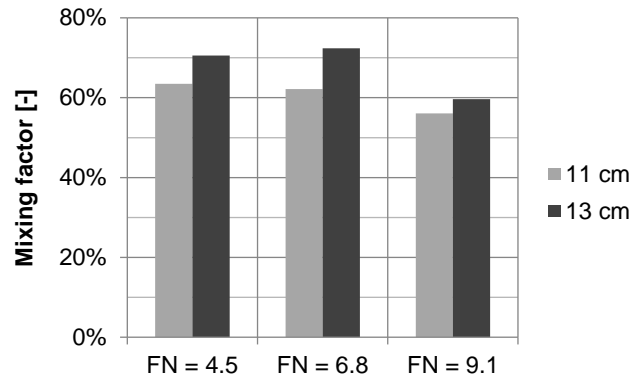


**Figure 5.17:** *Influence of fluidization number and bed height in the fluidization reactor on the gravel concentration in the recirculation stream.*

For the lower bed height of 11 cm the gravel concentration in the bed material recirculation stream remains nearly constant for the first two fluidization numbers but then decreases to a lower value. If the bed height is increased to 13 cm the mixing factor first increases slightly and then decreases again to a lower value.

## 5.6 Discussion

In all conducted experiments the char shows a flotsam behavior. This was to be expected since the char particles are lighter and larger than the jetsam bronze particles. Thus, potential for segregation in the reactor occurs and mixing factors of which are below 1, $M < 1$, occur. These results are also in agreement with the experimental evidence described in section 3 in this work.

As a baseline the mixing factor for all experiments is shown in Table 5.9. The first column is the fluidization number for the conducted experiments. All the other columns define one operating point with different char concentrations in the system, bed heights and bed material recirculation rates, according to Figure 5.11.

From all the Figures in the previous section and from Table 5.9 it can be seen that the mixing factor increases with increasing fluidization number. This is plausible due

to more vigorous bubble movement at higher fluidization rates. Jetsam particles are more often transported upwards in the wake of the bubbles. Therefore, a more even concentration profile along the bed height can be obtained. Char is good mixed at higher fluidization numbers $FN > 7$ and low char concentrations in the system. This evidence is also in agreement with the findings in chapter 3.

**Table 5.9:** *Overview over all experiments and the observed trends.*

| $u\_0/u\_mf$ | 2%, 9 cm, 173 g/s | 2%, 9 cm, 258 g/s | 2%, 9 cm, 344 g/s | 4%, 9 cm, 173 g/s | 4%, 9 cm, 258 g/s | 4%, 9 cm, 344 g/s | 6%, 9 cm, 173 g/s | 6%, 9 cm, 258 g/s | 6%, 9 cm, 344 g/s | 2%, 11 cm, 258 g/s | 4%, 11 cm, 258 g/s | 6%, 11 cm, 258 g/s | 2%, 13 cm, 258 g/s | 4%, 13 cm, 258 g/s | 6%, 13 cm, 258 g/s |
|---|---|---|---|---|---|---|---|---|---|---|---|---|---|---|---|
| 3.4 | 66.35% | 67.40% | 73.89% | 51.76% | 55.41% | 60.04% | 43.56% | 46.24% | 46.25% | 74.99% | 57.13% | 40.19% | 56.97% | 37.72% | 31.40% |
| 4.5 | 71.87% | 79.38% | 84.34% | 62.20% | 67.11% | 69.08% | 54.73% | 60.35% | 60.43% | 82.21% | 64.14% | 57.34% | 61.05% | 53.80% | 49.54% |
| 5.7 | 79.22% | 83.75% | 92.47% | 73.24% | 75.86% | 78.72% | 64.60% | 67.67% | 65.77% | 90.02% | 78.79% | 63.90% | 67.38% | 60.82% | 55.03% |
| 6.8 | 81.49% | 88.87% | 94.37% | 77.79% | 79.22% | 85.80% | 70.55% | 75.65% | 74.72% | 97.42% | 82.48% | 70.04% | 73.36% | 67.89% | 62.77% |
| 7.9 | 86.82% | 91.99% | 96.46% | 82.14% | 83.61% | 87.10% | 72.66% | 78.37% | 77.99% | 91.12% | 84.86% | 71.49% | 79.14% | 72.93% | 70.87% |
| 9.1 | 89.52% | 95.06% | 97.30% | 84.83% | 84.68% | 87.83% | 76.70% | 81.66% | 83.94% | 99.36% | 86.66% | 76.24% | 82.62% | 74.17% | 72.97% |

As it was found, a higher recirculation of the bed material increases the mixing factor. It is assumed that higher recirculation causes more turbulence in the bed and therefore better mixing. However, this effect decreases with increasing char concentration in the system. It should be noted that in the commercial plant the recirculation cannot be varied at will because the temperatures in the system depend strongly on the recirculation rate. The recirculation rate is also dependent on the air flow and the air staging in the combustion reactor. In literature no similar experiments were found, thus a comparison is not possible with results found by other authors.

Since the char concentration is not known in the commercial plant but are supposed to be in a range of around 5% [14] notable segregation could occur. If more char is present in the system it also influences the bed height since the bulk density of the char is very low. If the char concentration in the system is increased the mixing factor decreases. As shown in chapter 3 no general statement can be drawn about the influence of the concentration of the flotsam particles. Bilbao et al. [128] found improved mixing for higher sand mass fraction which would agree with the results in this work.

In this regard also the question could be answered if a doubling of the char concentration in the system also leads to a doubling or tripling of the char concentration in the recirculation stream. From the experiments the answer is clearly "no" in both cases.

The mixing factor also decreases with increasing bed height of bronze at minimum fluidization conditions. This can be explained by the fact that the char shows flotsam tendency. With increasing bed height the distance between bed surface and outlet of the fluidization reactor increases. Therefore less char is entrained and its concentration in the recirculation stream decreases. Cluet et al. [133] investigated the influence of the bed height for wood/sand mixtures. Contrary to the present study they did not find a dependence on the bed height. However, they did not scale their configuration which could also have an influence.

A concentration profile depicted in Figure 5.18 gives a qualitative estimate of the conditions in the fluidization reactor based on the experimental observations.
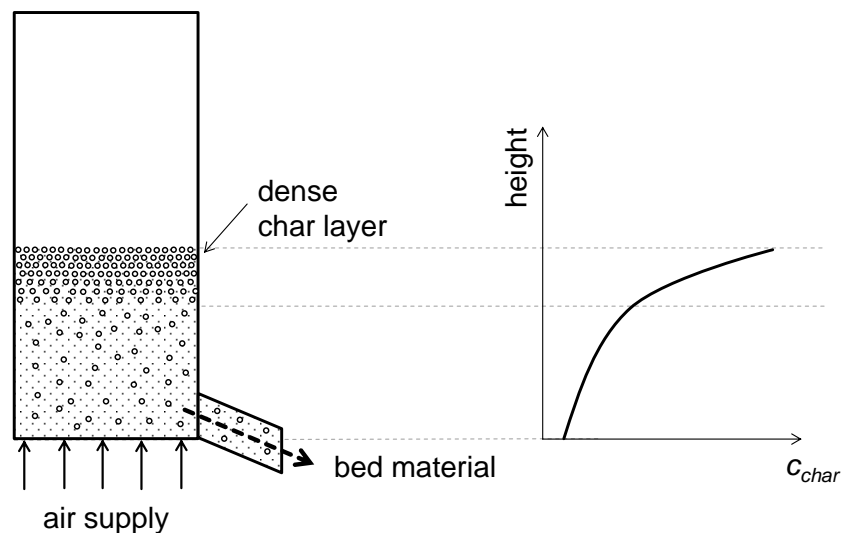


**Figure 5.18:** *Estimated char profile in the fluidization reactor.*

It is assumed that a char rich layer forms at the surface of the bed. This was also observed visually and was more distinct for higher char concentrations. Therefore, a char-rich zone formes where the char concentration in the bed decreases rapidly. then in a low concentration zone the char concentration decreases to its final value at the bottom of the fluidization reactor.

The experiments conducted with gravel showed a contradictory result. Higher fluidization rates did not lead necessarily to higher mixing factors. For the highest fluidization number of $FN = 9.1$ for both investigated bed heights the mixing factor decreased significantly.

A similar result was found by Zhang et al. [106] who investigated the behavior of biomass cylinders in a sand bed fluidized with air under ambient conditions. For

fluidization numbers of $FN = 7$ they found a maximum for the mixing for 3% wt.-% of biomass. If the fluidization number is further increased more segregation occurs. This would also be in the range of the results found in this work where the drop occurs between $FN = 6.8$ and $FN = 9.1$ for $c_{gravel,system} = 4\%$. The results imply that the same fluidization behavior occurs for scaled (this work) and not scaled (Zhang et al.) conditions.

# 6 Design and scale-up considerations

In this chapter the design and ongoing mixing processes inside the commercial plant were investigated. The Barracuda simulation was used to investigate ongoing mixing processes inside the gasification reactor.

Furthermore, effects on the design due to scaling were examined in the cold flow model. Scale-up and design always depend on each other. For smaller plants some effects due to the design do not take place whereas for larger plants this could become an issue. The slope of the gasification reactor is critical in this respect since poorly mixed zones can occur.

## 6.1 Mixing of hot bed material in gasification reactor

As already mentioned, heat-up of the bed material in the combustion reactor is crucial for the operation of the DFB system. Especially the biomass particles need sufficient contact with the hot bed material particles to ensure quick heat-up to avoid tar formation.

Tar can cause massive problems in downstream unit operations since condensed tar can plug pipes or can cause fowling at heat exchanger surfaces [6]. Due to uneven heat distribution in the gasification reactor undesired tar formation could be enhanced and could cause the aforementioned operational problems.

The effect of heat-up is also predicted by the simulation. In Figure 6.1 only bed material particles are shown and colored by the temperature. Note that the scale on the left is in Kelvin. Green colors mean temperatures typical for the gasification reactor in the range of about 840 °C. Through heat-up the temperature of the bed material increases in the combustion reactor to about 900 °C, indicated by more orange particles.

Looking at the particle temperature in the combustion reactor in can be clearly seen
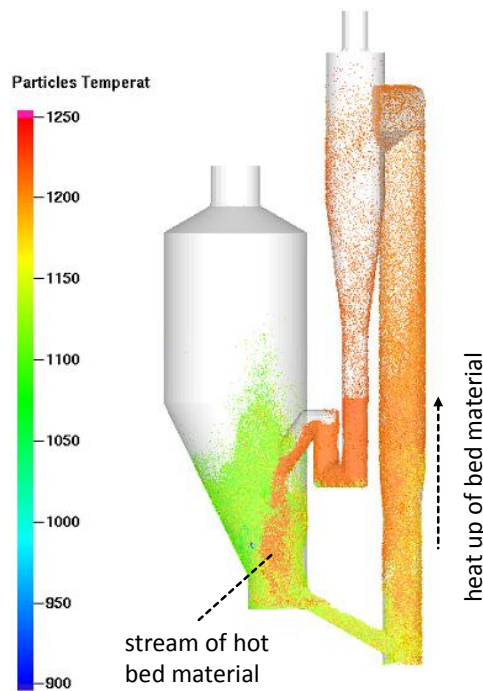
**Figure 6.1:** *Temperature of the circulating bed material.*

that the temperature is increased from the temperature in the gasification reactor to the final temperature after the combustion reactor. This can also be seen through the temperature change from green/yellow at the bottom of the combustion reactor until orange/red at its top.

The bed material should provide the heat for the endothermic drying and devolatilization reactions. To ensure even distribution of the heat a good mixing of the hot bed material into the colder bed of the gasification reactor is crucial.

In Figure 6.1 it can be seen that a hot stream exists which bypasses from the loop seal to the chute. This is also illustrated in Figure 6.2 where the lower part of the gasification reactor is depicted. Three cutplanes are depicted and colored with the averaged fluid temperature. The scale on the left is in Kelvin. It can be seen that there is a hot region at the front side of the reactor where the hot bed material bypasses as shown in Figure 6.1. The back side of the gasification reactor does not see this hot stream.

The results shown in Figure 6.1 and 6.2 indicate that the mixing of the recirculated hot bed material is not optimal in the gasification reactor and a bypass stream occurs.
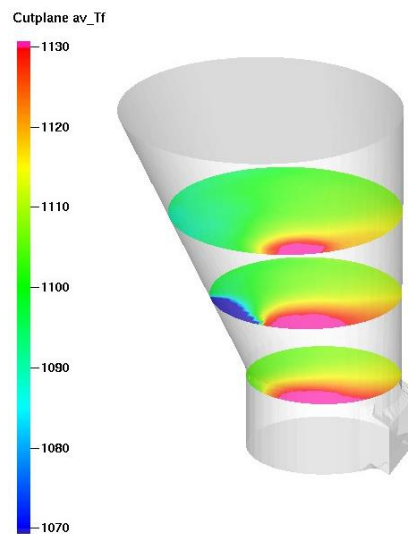
**Figure 6.2:** *Averaged fluid temperatures in the gasification reactor.*

## 6.2 Mixing of biomass particles in the gasification reactor

Mixing of the biomass particles in the gasification reactor in lateral direction is an important issue regarding the size or diameter of the reactor. It takes some time for the biomass to dry and devolatalize. As mentioned earlier these times are in the range of $10^2$ seconds. If the time for the movement to the opposite wall of the reactor is larger than the time for drying and devolatilization parts of the bed do not participate in the reaction or conversion processes.

In Figure 6.3 the mixing of the wood particles into the gasification reactor is depicted. The particles are fed continuously into the gasification reactors. The pictures are shown for 1, 2, 5, and 10 seconds after injection of the biomass particles which are colored blue.

From the top view it can be seen that after 10 seconds the first biomass particles reach the opposite wall of the reactor. This indicates that the time for movement through the reactor is much shorter than the time for devolatilization.

## 6.3 Design of the gasification reactor

The asymmetric conical design of the gasification reactor was based on the assumption that the biomass particle dries and devolatalizes after feeding into the gasification reactor. An additional gas flow is released during drying and devolatilization and to keep
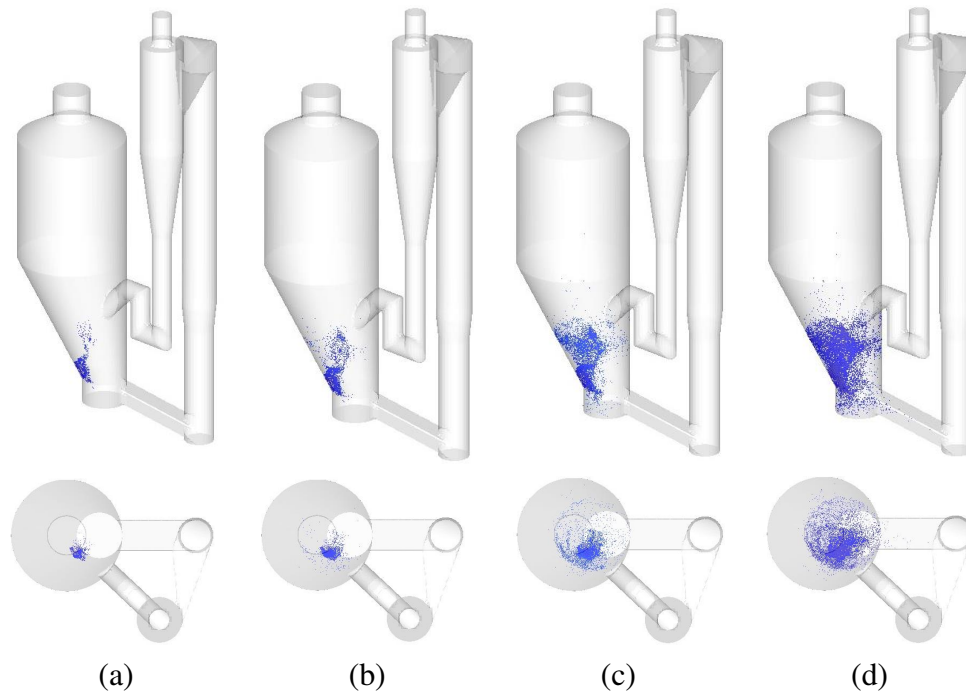
**Figure 6.3:** *Dynamic behavior of mixing of the wood particles in the gasification reactor. (a) ... 1 s after injection, (b) ... 2 s after injection, (c) ... 5 s after injection, (d) ... 10 s after injection.*

the superficial velocity, $u_0$, constant the cross section area has to expand. To construct the reactor as compact as possible an asymmetric cone was used. Otherwise the chute would have to be longer and the distances between gasification and combustion reactor as well as cyclone would have increased.

Figure 6.4 shows the percentage of gas flow in the gasification reactor. It can be seen that only 16% of the whole gas amount come from the fluidization steam. The other 84% are the moisture and the volatiles from the biomass feed stock. If the reactor would be only cylindrical this would increase the superficial velocity which then could lead to more bed material elutriation and thus bed material loss. An extension of the cross-sectional area is therefore necessary to ensure $u_0 = const$.

However, such a design could lead to little or even non-fluidized zones since in the slope no fluidization comes from below. A poorly fluidized region could be the result which could then lead to negative effects regarding tar formation or poor mixing of the hot bed material.

Figure 6.5, (a), shows the lower part of the gasification reactor with three slices colored with the average axial velocity upwards or in z-direction. The scale at the left is in m/s, red to purple colors mean high fluidization velocities. Figure 6.5, (b), shows
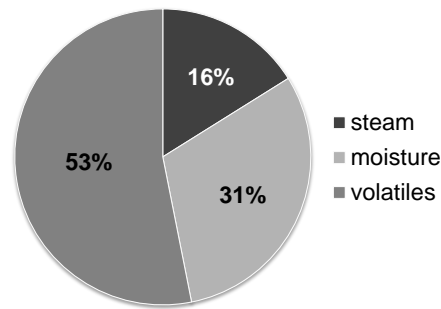
**Figure 6.4:** *Gas amounts released in the gasification reactor.*

the same part but the three slices are colored with the average particle volume fraction. Red colors mean high particle volume fractions which approach the close pack volume fraction.

The purple colored regions above the gas distributor in Figure 6.5, (a), indicate that the fluidization velocity is 1.2 m/s or higher. This produces a well bubbling bed. In the same region in Figure 6.5, (b), it can be seen that the average particle volume fraction is in the range of $\varepsilon_p = 0.35$ which also corresponds to a bubbling bed regime.

Going towards the inclination it can be seen in Figure 6.5, (a), that the axial velocity decreases the closer one approaches the wall. A region occurs with very low axial velocities and as a consequence a poorly fluidized region occurs. The same can also be seen in Figure 6.5, (b). Approaching the wall leads to more red colors which indicates higher particle volume fractions and $\varepsilon_p \rightarrow \varepsilon_{cp}$.



(a)  (b)
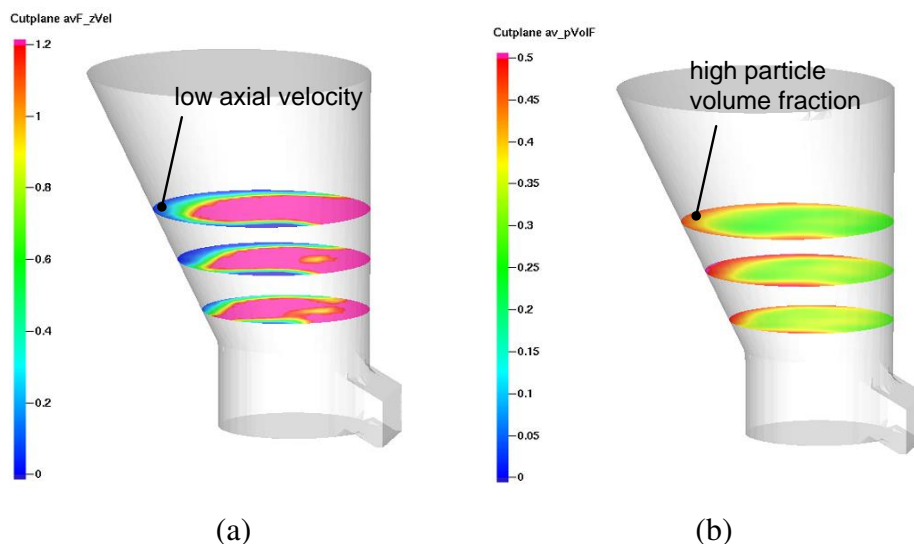
**Figure 6.5:** *Fluidization of the slope in the gasification reactor.*

For the commercial plant in Güssing large poorly fluidized zones below the slope

are not likely to occur. However, for larger DFB plants this could become an issue. This issue is dealt with in the next section.

## 6.4 Improvement of particle mixing in the slope

As already shown no poorly fluidized zones above the slope occur in the gasification reactor of the commercial plant in Güssing. The HGA Senden in Germany is of the same design as the plant in Güssing but is of the double size and has a fuel power of 15 $MW_{th}$ [47]. Furthermore, the HGA Senden suffers from high tar load in the product gas which causes problems in downstream processes. Therefore, the region above the slope could be an issue in larger DFB plants.

To investigate this topic a slope was implemented in the fluidization reactor of the cold flow model, see section 5.2 for more information. Doing so, the influence of the slope on the fluidization behavior could be investigated.

Figure 6.6 (a) shows a side view of the slope in the gasification reactor in large DFB plants like the HGA Senden. Below the slope a poorly fluidized region occurs. Since bubbles cause particle mixing in fluidized beds, chapter 3, in this region particle mixing is limited.



dead volume

Bottom fluidization | Slope

(a) (b)
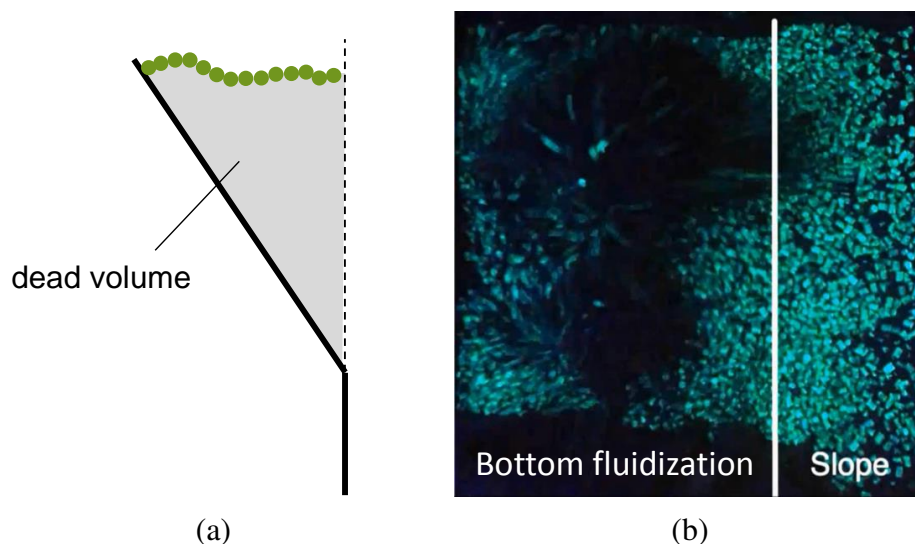
**Figure 6.6:** *Poorly fluidized zone above the slope in large DFB systems. (a) ... schematic drawing (side view), (b) ... picture from the cold flow model experiments (top view).*

As it was observed in cold flow model investigations the fuel particles tend to move to the surface very quickly once inserted to the fluidized bed. This was also observed

in hot devices where a bubble of volatiles forms around a fuel particle and exerts an additional force upwards [18]. Therefore, it is likely that the biomass particles, which are fed into the gasification reactor, move quickly to the surface. Some of them are then deposited at the surface above the slope region and rest there.

This is also confirmed by cold flow model investigations which is shown in Figure 6.6 (b). For these experiments bronze particles and luminous gravel particles (to simulate biomass as fuel) were used. Therefore, only the luminous particles can be seen. Bronze and bubbles appear black. As it can be seen, in the region of the slope the luminous particles are resting on the bed surface whereas in the region of the bottom fluidization the particles are well mixed.

The fuel particles, resting at the bed surface above the slope region, have limited contact with the hot bed material. Therefore, the formation of long tar molecules is more likely. To increase particle mixing in the region above the slope it can be fluidized and was equipped with additional nozzles. More bubbles occur and the wood particles are dragged into the bed, Figure 6.7 (a).

The results are shown in Figure 6.7 (b). As it can be seen the slope region as well as the region above the bottom fluidization are now well fluidized and the luminous particles are also dragged into the bed.



(a)                                        (b)
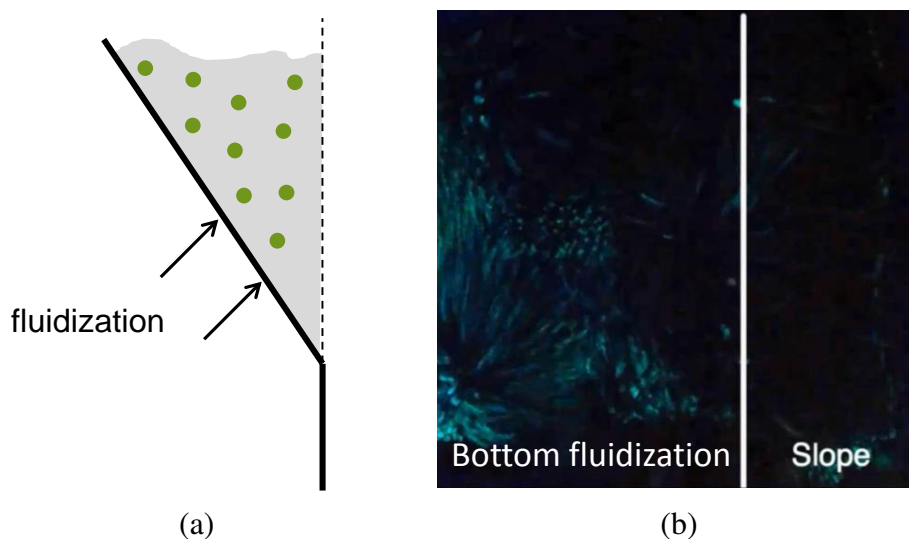
**Figure 6.7:** *Mixing of fuel particles in the slope region if the slope is fluidized. (a) ... schematic drawing (side view), (b) ... picture from the cold flow model experiments (top view).*

These findings were also used in the commercial plant in Senden where nozzles were implemented into the slope to enhance fluidization. First results of conducted tar measurements show a large decrease of tars in the raw product gas. However, by the

time this work was written, research is still ongoing.

## 6.5  Summary and conclusion

Barracuda and the cold flow model were used to investigate ongoing mixing processes inside DFB system as well as design considerations which arise from scale-up.

The Barracuda model was used to investigate the mixing of the hot bed material coming from the loop seal and the movement of the biomass particles in lateral direction. The simulation results showed that a hot stream of bed material bypasses in the gasification reactor. Therefore, the lateral mixing of the bed material is not optimal which results in an uneven temperature distribution within the bed.

The movement of the biomass particles in lateral direction was investigated for commercial plant in Güssing. It showed that the whole cross section area is used for the drying and devolatilization reactions. Therefore, the time scales for mixing is sufficiently small.

Furthermore, the Barracuda model was used to investigate if the slope could have an negative effect on the fluidization behavior in the gasification reactor. Regions of low axial velocities and thus high particle volume fractions could be observed. However, these regions seem to be rather small in plants of the size of the Güssing reactor.

However, this could become an issue for larger DFB plants like the HGA Senden in Germany. Cold flow model investigations showed that above the slope a poorly fluidized zone occurs where the contact between the bed material and the biomass feedstock could be limited and the heat-up of the biomass particles is slowed down. As a consequence, higher tar loads in the product gas could occur.

It was shown by cold flow model experiments that an implementation of nozzles in the slope could significantly enhance the particle mixing in this region above the slope. First tar measurements conducted in the commercial plant in Senden show promising results and a decrease of the tar load if the additional nozzles in the slope are used.

# 7 Summary and conclusion

In this work mixing and segregation processes of the particles in a dual fluidized bed (DFB) systems were investigated. Most of the work was done based on the commercial DFB plan in Güssing, Austria. Two approaches were used and combined: computational particle fluid dynamics simulations and cold flow modeling.

As software package the commercial code Barracuda was used which works which the MP-PIC implementation. MP-PIC stands for multi-phase particle-in-cell and allows calculating also large vessels in an appropriate amount of time.

Furthermore, a cold flow model was constructed to investigate the char concentration in the recirculating bed material stream. It is constructed with a recirculating bed material stream which can be controlled by a rotary valve. Sampling is possible during operation.

The research questions are repeated here:

**Q1** How do the char particles mix in the system and how is this mixing behavior dependent on various operating parameters?

**Q2** How does the hot bed material in the gasification reactor mix?

**Q3** Is there a need for more feed points for the biomass in the commercial plant?

**Q4** Is there any potential for poorly fluidized zones in the hot reactor?

**Q5** In the view of scale-up, is the conical shape of the gasification reactor optimal also for larger DFB systems?

Research question **Q1** can be answered as follows. It was confirmed that the char inside the DFB system shows a flotsam behavior which is mostly relevant in the gasification reactor. It was shown that the concentration of the char in the bed material recirculation stream shows significant dependence on various operation parameters. Therefore, a mixing factor was introduced which can take values from 0 to 1, $0 < M < 1$. $M = 0$ means no char in the recirculation stream and $M = 1$ means a perfect distribution of the char over the height in the gasification reactor.

If the fluidization rate is increased also the mixing factor increases due to more vigorous bubble movement; more bed material is dragged upwards in the wake of the

bubbles char mixing is enhanced. The mixing factor also increases if the bed material recirculation rate is increased. It was shown that a doubling and tripling of the char concentration in the system does not lead to a doubling and tripling of the amount of char in the recirculation stream. If the bed height in the bubbling bed is increased the mixing factor also decreases due to the flotsam behavior of the char and the increasing distance between the bed material drain at the bottom and the char rich bed surface.

Furthermore, experiments with gravel were conducted which represent biomass particles according to the scaling relationships. An opposite trend was found compared to the char particles: The mixing factor decreases with increasing fluidization velocity.

In this work only the movement of char and biomass particles with one distinct particle size was investigated. Future work should include more particle sizes. Furthermore, investigations should be carried out whether larger or smaller char particles are mixed better in the gasification reactor. Furthermore, also mixtures of different densities should be accounted for to investigate the influence of the density on the mixing processes inside the system.

After discussing the findings of the cold flow model experiments, the results from the CPFD simulations are shown.

In this work the cold flow model of the commercial plant in Güssing and the commercial plant itself were simulated. First, the cold flow model was simulated to investigate the influence of the drag law on the prediction of the bed material recirculation rate which is an important quantity for DFB systems. Tested drag models were: EMMS, Ganser, Turton-Levenspiel and Wen-Yu/Ergun.

Measured pressure profiles were compared to the simulation results and it was shown that the EMMS drag model predicts best the pressure drops over the reactor parts: gasification reactor, combustion reactor and loop seal. However, it failed to predict the pressure profile along the combustion reactor.

Neither of the drag laws was able to predict the measured influences of air variation in the combustion reactor on the bed material recirculation rate. In general, the Ganser drag model gives the lowest deviations, however, measured trends are not entirely predicted. Although the EMMS drag model gives the best predictions for the pressures it gives the worse regarding bed material recirculation rate.

From these results no clear recommendation for the use of the drag law for the simulations of the commercial plants could be given. Therefore, for the simulation of the commercial plant also all the 4 aforementioned drag laws were tested regarding their applicability for the prediction of the bed material recirculation rate.

The simulation results showed that the EMMS drag law gives the best results re-

garding pressures and bed material recirculation rate which is contrary to the results obtained for the simulations of the Güssing cold flow model.

Based on the results in this work it cannot be said if this is due to scaling of the bed material in the cold flow model or if it is a coincidence. It has to be noted that the air staging in the cold flow model experiments was not similar to the air staging in the Güssing commercial plant as it can be seen in Figure 7.1. In this figure the percentage of the total air is shown which is fed into the bottom, primary and secondary air inlet. It cannot be concluded which factors determine a valid prediction of the bed material recirculation rate.
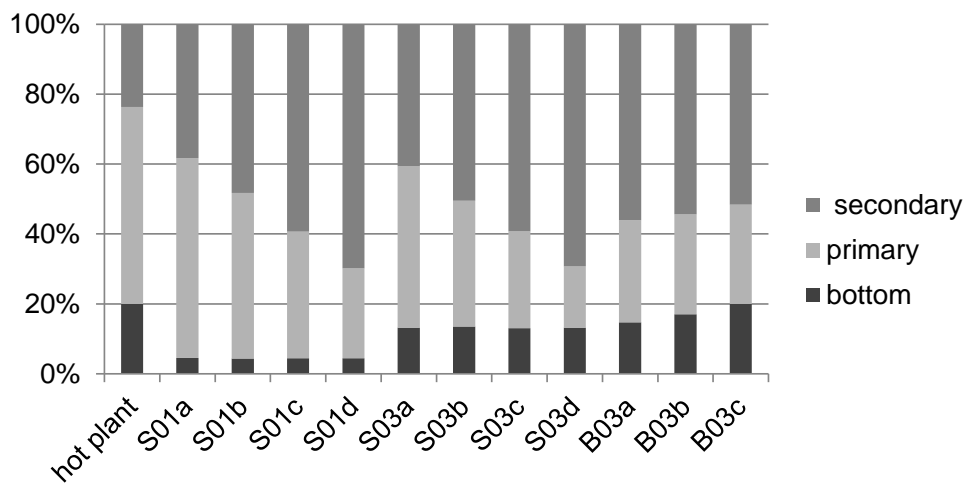
**Figure 7.1:** *Air stagings for the commercial plant and the simulated cold flow model experiments.*

The simulation model for the commercial plant was then validated with experimental values from the real operation. It was able to predict pressures, temperatures as well as product and flue gas compositions.

Based on the validated model the relevant investigations were carried out to answer the research questions **Q2** to **Q4**. It could be shown that the hot bed material somewhat bypasses in the gasification reactor leading to maldistribution of the hot bed material.

For the Güssing reactor there is no need for further feed points since the biomass particles move sufficiently quickly across the bed to the opposite wall. Similar to the possibility of poorly fluidized zones above the slope in the gasification reactor in larger plants additional fuel points might be necessary.

From the simulations it can be seen that the slope of the gasification reactor does not cause poorly fluidized zones. However, this might be a problem in larger plants. More investigation is necessary regarding this aspect also combined with cold flow modeling

to confirm simulation results.

Generally, the Barracuda simulations proved to be a valid tool for investigating cold and commercial DFB plants. However, there is still limiting knowledge about the influences of drag laws and other parameters of the code on the fluid mechanics in a DFB system.

With Barracuda it was possible to simulate a full DFB system which could also be validated properly. However, many assumptions have been made. Especially the choice of the proper kinetics and particle models brings large possibilities for errors. Therefore, they have to be validated and chosen for every other operation point.

It can be recommended to use Barracuda merely for tests of various different configurations and to exclude the least promising. Configurations which seem more promising can then be simulated in greater detail and also by cold flow modeling.

Research question **Q5** can be discussed as follows. It could be shown by cold flow model experiments that there is a potential of poorly fluidized zones above the conical section in large DFB plants. Fuel particles lie at the bed surface above the slope in the gasification reactor and as a result, they have limited contact with the hot bed material. This could favor the formation of large tar molecules which are undesired in the product gas.

By fluidizing the slope with additional nozzles the cold flow model experiments revealed that the particle mixing could be improved significantly in the region above the slope. This also enhances the contact between the hot bed material and the fuel particles which leads to lower tar values in the product gas.

In the HGA Senden, which is of the double size as the plant in Güssing, additional nozzles were implemented in the slope. First tar measurements show decreasing tar load if the nozzles are used which is very promising and should be considered for further scale-up considerations of DFB systems.

# Appendix A: Implementation of drag laws

In the following the implementation of the drag laws in Barracuda is presented.

### Ganser drag law

$$C_{d,GA} = \varepsilon_g^{-2.65} K_2 \left[ \frac{24}{Re_p K_1 K_2} \left( 1 + 0.1118(Re_p K_1 K_2)^{0.6567} \right) + \frac{0.4305}{1 + \frac{3305}{Re_p K_1 K_2}} \right], \quad (7.1)$$

with

$$K_1 = \frac{3}{1 + 2\varphi_p^{-0.5}} \quad \text{and} \quad K_2 = 10^{1.8148(-\log \varphi_p)^{0.5743}} \tag{7.2}$$

### EMMS drag law

The EMMS drag law in Barracuda is implemented with $f_e = \frac{Re_p}{24} C_d$:

$$f_e = \begin{cases} \frac{1}{18\varepsilon_g} \left( 150\frac{\varepsilon_p}{\varepsilon_g} + 1.75 Re_p \right) & \varepsilon_g < 0.74 \\ \left( 1.0 + 0.15 Re_p^{0.687} \right) \omega & \varepsilon_g \geq 0.74 \text{ and } Re_p < 1000 \\ 0.44 \frac{Re_p}{24} \omega & \varepsilon_g \geq 0.74 \text{ and } Re_p \geq 1000 \end{cases} \tag{7.3}$$

For the function $\omega$ the following equations are implemented:

$$\omega = \begin{cases} -0.5760 + \frac{0.0214}{4\left(\varepsilon_g - 0.7463\right)^2 + 0.0044} & 0.74 \leq \varepsilon_g \leq 0.82 \\ -0.0101 + \frac{0.0038}{4\left(\varepsilon_g - 0.7789\right)^2 + 0.0040} & 0.82 < \varepsilon_g \leq 0.97 \\ -31.8295 + 32.8295\varepsilon_g & 0.97 < \varepsilon_g \leq 1 \end{cases} \tag{7.4}$$

### Turton–Levenspiel drag law

$$C_{d,\text{TL}} = \frac{24}{Re_p}\left(1 + 0.173 Re_p^{0.657}\right)\varepsilon_g^{-2.65} + \frac{0.413}{1 + 16300 Re_p^{-1.09}}\varepsilon_g^{-2.65}. \qquad (7.5)$$

### Wen–Yu/Ergun drag law

$$C_{d,WY} = \begin{cases} \frac{24}{Re_p}\varepsilon_g^{-2.65} & Re_p < 0.5 \\ \frac{24}{Re_p}\varepsilon_g^{-2.65}\left(1 + 0.15 Re_p^{0.687}\right) & 0.5 \le Re_p \le 1000 \\ 0.44\varepsilon_g^{-2.65} & Re_p > 1000 \end{cases} \qquad (7.6)$$

In Barracuda a blended function is as follows:

$$D_{p,WE} = \begin{cases} D_{WY} & \varepsilon_p < 0.75\varepsilon_{cp} \\ (D_{ER} - D_{WY})\left(\dfrac{\varepsilon_p - 0.75\varepsilon_{cp}}{0.85\varepsilon_{cp} - 0.75\varepsilon_{cp}}\right) + D_{WY} & 0.75\varepsilon_{cp} \ge \varepsilon_p \ge 0.85\varepsilon_{cp} \\ D_{ER} & \varepsilon_p > 0.85\varepsilon_{cp} \end{cases}$$

$$(7.7)$$

where $D_{ER}$ and $D_{WY}$ are the drag functions of the Ergun and Wen–Yu drag law, respectively. $D_{WY}$ is calculated according to Eq. (2.53) and (7.6). For $D_{ER}$ the following equation is used in Barracuda:

$$D_{ER} = \left(\frac{180}{Re_p}\frac{\varepsilon_p}{\varepsilon_g} + 2\right)\frac{\rho_g |\mathbf{u}_g - \mathbf{u}_p|}{d_p \rho_p} \qquad (7.8)$$

# Nomenclature

| symbol | meaning | SI units |
|---|---|---|
| $a, b, c, d, e$ | coefficients in Eq. (2.57) | – |
| $\mathbf{a}_p$ | particle acceleration | m/s$^2$ |
| $A_{bed}$ | bed cross section area | m$^2$ |
| $A_{ls}$ | cross section area of loop seal | m$^2$ |
| $A_p$ | cross sectional area of the particle | m$^2$ |
| $c$ | concentration | mol/m$^3$ |
| $c_{char}$ | char concentration | kg/kg |
| $\bar{c}_{char}$ | mean char concentration | kg/kg |
| $c_{gravel}$ | gravel concentration | kg/kg |
| $c_{p,g}$ | specific heat capacity of the gas | J/(kg K) |
| $C_1, C_2$ | coefficients in Eq. (2.16) | – |
| $C_d$ | drag coefficient | – |
| $d_{bed}$ | bed diameter | m |
| $d_F$ | particle diameter of the FLUID component | m |
| $d_i$ | inner diameter | m |
| $d_M$ | mixture particle diameter | m |
| $d_p$ | particle diameter | m |
| $d_P$ | particle diameter of the PACKED component | m |
| $d_{sv}$ | Sauter diameter | m |
| $D$ | characteristic diameter | m |
| $d_F$ | particle diameter of the FLUID component | m |
| $d_M$ | mixture particle diameter | m |
| $D_p$ | drag function | 1/s |
| $DR$ | density ratio | – |
| $e_b$ | emissivity of the bed particles | – |
| $e_w$ | emissivity of the wall | – |
| $E_a$ | activation energy | J/mol |

| symbol | meaning | SI units |
|---|---|---|
| $f$ | probability density function | – |
| $\mathbf{F}$ | momentum exchange rate | N/m$^3$ |
| $\mathbf{F}_b$ | buoyancy force | N |
| $\mathbf{F}_d$ | drag force | N |
| $\mathbf{F}_g$ | weight | N |
| $\mathbf{F}_{g,g}$ | weight of gas | N |
| $\mathbf{F}_{g,p}$ | weight of particles | N |
| $FN$ | fluidization number | – |
| $g$ | gravity | m/s$^2$ |
| $G_s$ | bed material recirculation flux | kg/(m$^2$s) |
| $h_\infty$ | bed height at steady state | m |
| $\Delta h_{bed}$ | bed height interval | m |
| $\Delta h_{evap}$ | evaporation enthalpy | J/mol |
| $\Delta h_R^0$ | standard enthalpy of reaction | J/mol |
| $k$ | reaction rate constant | dependent |
| $k_0$ | pre-exponential factor | dependent |
| $K_{WGS}$ | equilibrium constant of the water-gas-shift reaction | – |
| $L$ | characteristic length | m |
| $L_1, L_2$ | characteristic lengths in Eq. (2.42) | m |
| $m$ | mass | kg |
| $M$ | mixing factor | – |
| $m_{bed}$ | bed material mass | kg |
| $m_p$ | particle mass | kg |
| $\delta \dot{m}_p$ | production rate from chemistry | kg/(m$^3$ s) |
| $\dot{m}_{bottom}$ | mass flow of bottom air | m$^3$/s |
| $\dot{m}_{prim}$ | mass flow of primary air | m$^3$/s |
| $\dot{m}_{rec}$ | bed material recirculation rate | kg/s |
| $\dot{m}_{sec}$ | mass flow of secondary air | m$^3$/s |
| $\dot{m}_{tot}$ | total volume flow | m$^3$/s |
| $p$ | pressure | Pa |
| $\Delta p_{bed}$ | pressure drop over the bed | Pa |
| $P_s$ | solids pressure | Pa |
| $\dot{q}$ | heat flux | W/m$^2$ |
| $\dot{r}$ | reaction rate | dependent |

| symbol | meaning | SI units |
|--------|---------|----------|
| $rd$ | relative deviation | – |
| $R_m$ | universal gas constant | J/(mol K) |
| $S_p$ | particle surface | m$^2$ |
| $SR$ | size ratio | – |
| $\Delta t$ | time interval | s |
| $t$ | time | s |
| $t_\infty$ | time until equilibrium is reached | s |
| $\Delta T$ | temperature difference | K |
| $T_b$ | temperature of the bed particles | K |
| $T_p$ | particle temperature | K |
| $T_w$ | temperature of the wall particles | K |
| $T_{evap}$ | evaporation temperature | K |
| $u_0$ | superficial velocity | m/s |
| $u_{0,req}$ | required superficial velocity | m/s |
| $\mathbf{u}_g$ | gas velocity | m/s |
| $u_{bf}$ | velocity of beginning fluidization | m/s |
| $u_{cf}$ | velocity of complete fluidization | m/s |
| $u_d$ | displacement velocity | m/s |
| $u_F$ | minimum fluidization velocity of the FLUID component | m/s |
| $u_{ib}$ | initial bubbling velocity | m/s |
| $u_M$ | minimum fluidization velocity of a complete mixed bed | m/s |
| $u_{mf}$ | minimum fluidization velocity in general | m/s |
| $u_{MS}$ | minimum fluidization velocity for partially segregating systems | m/s |
| $\mathbf{u}_p$ | particle velocity | m/s |
| $u_P$ | minimum fluidization velocity of the PACKED component | m/s |
| $u_S$ | minimum fluidization velocity for complete segregating systems | m/s |
| $\bar{\mathbf{u}}_p$ | local mass averaged particle velocity | m/s |
| $u_t$ | terminal velocity | m/s |
| $V_g$ | gas volume | m$^3$ |
| $V_p$ | particle volume | m$^3$ |
| $V_{p,i}$ | particle volume of i-th particle size interval | m$^3$ |
| $V_{p,tot}$ | volume of all particles | m$^3$ |
| $\dot{V}$ | volume flow | m$^3$/s |
| $\dot{V}_{req}$ | required volume flow | m$^3$/s |

| symbol | meaning | SI units |
|--------|---------|----------|
| $x$ | mass fraction | kg/kg |
| **x** | location in space | m |
| $y$ | molar fraction | mol/mol |

# Greek letters

| symbol | meaning | SI units |
|---|---|---|
| $\alpha$ | heat transfer coefficient | W/(m$^2$ K) |
| $\alpha, \beta$ | constants in Eq. (2.54) | – |
| $\alpha_{cond}$ | conductive heat transfer coefficient | W/(m$^2$ K) |
| $\alpha_{conv}$ | convective heat transfer coefficient | W/(m$^2$ K) |
| $\alpha_o$ | overall heat transfer coefficient | W/(m$^2$ K) |
| $\alpha_{rad}$ | radiative heat transfer coefficient | W/(m$^2$ K) |
| $\beta_d$ | drag coefficient in continuity equation | N/m$^3$ |
| $\varepsilon_{cp}$ | close pack volume fraction | – |
| $\varepsilon_g$ | gas voidage | – |
| $\varepsilon_{mf}$ | gas voidage at minimum fluidization conditions | – |
| $\varepsilon_p$ | particle voidage | – |
| $\delta\dot{m}_p$ | mass production rate per volume | kg/(s m$^3$) |
| $\lambda_g$ | heat conductivity of the gas | W/(m K) |
| $\mu_g$ | dynamic viscosity of the gas | kg/(m s) |
| $\nu$ | stoichiometric coefficient | – |
| $\Pi$ | Pi group | – |
| $\zeta_h$ | coefficient | – |
| $\Delta\rho$ | density difference | kg/m$^3$ |
| $\rho_{bed}$ | bed density | kg/m$^3$ |
| $\rho_g$ | gas density | kg/m$^3$ |
| $\rho_p$ | particle density | kg/m$^3$ |
| $\rho_{p,bulk}$ | bulk density | kg/m$^3$ |
| $\sigma$ | Stefan-Boltzmann constant | W/(m$^2$K$^4$) |
| $\tau_D$ | particle collision damping time | s |
| $\tau_g$ | stress tensor of the gas phase | N/m$^2$ |
| $\tau_p$ | solids contact stress | N/m$^2$ |
| $\phi_p$ | sphericity | – |
| $\chi$ | physical variable | – |

# Abbreviations

| Abbreviation | meaning |
| --- | --- |
| BB | bubbling bed |
| CFB | circulating fluidized bed |
| CFD | computational fluid dynamics |
| CFL | Courant–Friedrichs–Lewy number |
| CLC | chemical looping combustion |
| CPFD | computational particle fluid dynamics |
| CHP | combined heat and power |
| DEM | discrete element method |
| DFB | dual fluidized bed |
| DNS | direct numerical simulation |
| el | electric |
| FCC | fluid catalytic cracking |
| HBP | HEAVY, BIG, PACKED |
| LSF | LIGHT, SMALL, FLUID |
| HSP | HEAVY, SMALL, PACKED |
| LBF | LIGHT, BIG, FLUID |
| HSF | HEAVY, SMALL, FLUID |
| LBP | LIGHT, BIG, PACKED |
| HS | HEAVY, SMALL |
| LB | LIGHT, BIG |
| MP-PIC | multi-phase particle-in-cell |
| MSW | municipal solid waste |
| PSD | particle size distribution |
| RME | rapeseed methyl ester |
| TFM | two fluid model |
| th | thermal |
| WGS | water-gas-shift |

# General indices

| index | meaning |
|---|---|
| *biomass* | biomass particle |
| *bed* | fluidized bed |
| *c* | commercial |
| *crit* | critical |
| *drying* | drying process |
| *F* | FLUID |
| *g* | gas |
| *ls* | loop seal |
| *m* | cold flow model |
| *mf* | minimum fluidization condition |
| *moisture* | moisture of particle |
| *p* | particle |
| *P* | PACKED |
| *pyrolysis* | pyrolysis process |
| *rec* | recirculated |
| *t* | terminal |

# Dimensionless numbers

| | |
|---|---|
| $Ar = \frac{\rho_g d_{sv}^3 (\rho_p - \rho_g) g}{\mu_g^2}$ | Archimedes number |
| $d*_p = Ar^{1/3}$ | dimensionless particle diameter |
| $Fr_p^2 = \frac{u_0^2}{d_p g}$ | Froude number |
| $Nu_p = \frac{\alpha d_p}{\lambda_g}$ | Nußelt number |
| $Pr = \frac{\mu_g c_{p,g}}{\lambda_g}$ | Prandtl number |
| $Re_p = \frac{d_p u_0 \rho_g}{\mu_g}$ | Particle Reynolds number |
| $Re_{p,mf} = \frac{d_p u_{mf} \rho_g}{\mu_g}$ | Particle Reynolds number at minimum fluidization conditions |
| $U^* = \frac{Re_p}{Ar^{1/3}}$ | dimensionless velocity |

# Bibliography

[1] J.C. Schmid, T. Pröll, H. Kitzler, C. Pfeifer, and H. Hofbauer. Cold flow model investigations of the countercurrent flow of a dual circulating fluidized bed gasifier. *Biomass Conversion and Biorefinery*, 2:229–244, 2012.

[2] H. Hofbauer, R. Rauch, R. Koch, and C. Aichernig. Biomass CHP Plant Güssing - A Success Story. In A.V. Bridgewater, editor, *Pyrolysis and Gasification of Biomass and Waste*. CPL Press, 2003.

[3] H. Hofbauer, R. Rauch, G. Löffler, S. Kaiser, E. Fercher, and H. Tremmel. Six years experience with the FICFB-gasification process. In *12th European Conference on Biomass and Bioenergy*, 2002.

[4] M. Bolhar-Nordenkampf, R. Rauch, C. Aichernig, and H. Hofbauer. Biomass CHP Plant Güssing - Using Gasification for Power Generation. In *Proceedings of the 2nd Regional Conference on Energy Technology Towards a Clean Environment*, 2003.

[5] F. Kirnbauer and H. Hofbauer. Investigations on Bed Material Changes in a Dual Fluidized Bed Steam Gasification Plant in Güssing, Austria. *Energy & Fuels*, 25:3793–3798, 2011.

[6] F. Kirnbauer, V. Wilk, H. Kitzler, S. Kern, and H. Hofbauer. The positive effects of bed material coating on tar reduction in a dual fluidized bed gasifier. *Fuel*, 95:553–562, 2012.

[7] F. Kirnbauer and H. Hofbauer. The mechanism of bed material coating in dual fluidized bed biomass steam gasification plants and its impact on plant optimization. *Powder Technology*, 245:94–104, 2013.

[8] S. Fail, N. Diaz, F. Benedikt, M. Kraussler, J. Hinteregger, K. Bosch, M. Hackel, R. Rauch, and H. Hofbauer. Wood gas processing to generate pure hydrogen suitable for PEM fuel cells. *ACS Sustainable Chemistry & Engineering*, 2:2690–2698, 2014.

[9] S. Müller, M. Stidl, T. Pröll, R. Rauch, and H. Hofbauer. Hydrogen from biomass: Large-scale hydrogen production based on a dual fluidized bed steam gasification system. *Biomass Conversion and Biorefinery*, 1:55–61, 2011.

[10] B. Rehling, H. Hofbauer, R. Rauch, and C. Aichernig. BioSNG - process simulation and comparison with first results from a 1 MW demonstration plant. *Biomass Conversion and Biorefinery*, 1:111–119, 2011.

[11] G. Weber, A. Di Giuliano, R. Rauch, and H. Hofbauer. Developing a simulation model for a mixed alcohol synthesis reactor and validation of experimental data in IPSEpro. *Fuel Processing Technology*, 141:167–176, 2016.

[12] A. Sauciuc, Z Abosteif, G. Weber, A. Potetz, R. Rauch, H. Hofbauer, G. Schaub, and L. Dumitrescu. Influence of operating conditions on the performance of biomass-based Fischer-Tropsch synthesis. *Biomass Conversion and Biorefinery*, 2:253–263, 2012.

[13] P.N. Rowe, A.W. Nienow, and A.J. Agbim. The mechanisms by which particles segregate in gas fluidised beds - binary systems of near-spherical particles. *Transactions of the Institution of Chemical Engineers*, 50:310–323, 1972.

[14] R.I. Singh, A. Brink, and M. Hupa. CFD modeling to study fluidized bed combustion and gasification. *Applied Thermal Engineering*, 52:585–614, 2013.

[15] J. Werther and T. Ogada. Sewage sludge combustion. *Progress in Energy and Combustion Science*, 25:55–116, 1999.

[16] A. Gomez-Barea and B. Leckner. Modeling of biomass gasification in fluidized bed. *Progress in Energy and Combustion Science*, 36(4):444 – 509, 2010.

[17] V. Wilk and H. Hofbauer. Analysis of optimization potential in commercial biomass gasification plants using process simulation. *Fuel Processing Technology*, 141:138–147, 2016.

[18] M. Fiorentino, A Marzocchella, and P. Salatino. Segregation of fuel particles and volatile matter during devolatilization in a fluidized bed reactor - II. Experimental. *Chemical Engineering Science*, 52:1909–1922, 1997.

[19] G. Bruni, R. Solimene, A. Marzocchella, P. Salatino, J.G. Yates, P. Lettieri, and M. Fiorentino. Self-segregation of high-volatile fuel particles during devolatilization in a fluidized bed reactor. *Powder Technology*, 128:11–21, 2001.

[20] K. Bosch. *Scale UP der Dampf-Wirbelschicht-Biomassevergasung vom Technikumsmastab in den industriellen Maßstab*. PhD thesis, TU Wien, 2007.

[21] A. Kreuzeder, C. Pfeifer, and H. Hofbauer. Fluid-dynamic investigations in a scaled cold model for a dual fluidized bed biomass steam gasification process: Solid flux measurements and optimization of the cyclone. *International Journal of Chemical Reactor Engineering*, 5, 2007.

[22] S. Shrestha, B.S. Ali, and M.D.B. Hamid. Cold flow model of dual fluidized bed: A review. *Renewable and Sustainable Energy Reviews*, 53:1529–1548, 2016.

[23] B.G.M. van Wachem, J.C. Schouten, C. M. van den Bleek, R. Krishna, and J:L: Sinclair. Comparative analysis of CFD models of dense gas-solid systems. *AIChE Journal*, 47:1035–1051, 2001.

[24] S. Kraft and H. Hofbauer. Fluidization of binary mixtures of dissimilar solids: A review. *Powder Technology*, submitted, 2017.

[25] S. Kraft, F. Kirnbauer, and H. Hofbauer. Influence of drag laws on pressure and bed material recirculation rate in a cold flow model of an 8 MW dual fluidized bed system by means of CPFD. *Particuology*, accepted for publication, 2017.

[26] S. Kraft, F. Kirnbauer, and H. Hofbauer. CPFD simulations of an industrial-sized dual fluidized bed steam gasification system of biomass with 8 MW fuel input. *Applied Energy*, 190:408–420, 2017.

[27] S. Kraft, F. Kirnbauer, and H. Hofbauer. Investigations using a cold flow model of char mixing in the gasification reactor of a dual fluidized bed gasification plant. *Powder Technology*, in press, 2016.

[28] Daizo Kunii and Octave Levenspiel. *Fluidization Engineering*. Butterworth-Heinemann, Boston, second edition edition, 1991.

[29] VDI-Gesellschaft. *VDI-Wärmeatlas*. Springer-Verlag, 2006.

[30] D. Geldart. Types of gas fluidization. *Powder Technology*, 7:285–292, 1973.

[31] S. Ergun. Fluid flow through packed columns. *Chemical Engineering Progress*, 48:89–94, 1952.

[32] C.Y. Wen and Y.H. Yu. Mechanics of fluidization. *Chemical engineering progress Symposium*, 62:100–111, 1966.

[33] J.R. Grace. *Fluidized Bed Hydrodynamics*. Hemisphere, Washington, 1982.

[34] H.D. Baehr and K. Stephan. *Heat and mass transfer*. Springer Vieweg, 2013.

[35] W.E. Ranz and W.R. Marshall. Evaporation from drops, part I. *Chemical Engineering Progress*, 48:141–146, 1952.

[36] W.E. Ranz and W.R. Marshall. Evaporation from drops, part II. *Chemical Engineering Progress*, 48:173–180, 1952.

[37] L. Fan and C. Zhu. *Principles of Gas–Solid Flows*. Cambridge University Press, 1998.

[38] J. Chen. *Handbook of Fluidization and Fluid–Particle Systems*, chapter Heat Transfer. CRC Press, 2003.

[39] N. Yang, W. Wang, W. Ge, L. Wang, and J. Li. Simulation of heterogeneous structure in a circulating fluidized-bed riser by combining the two-fluid model with the EMMS approach. *Industrial & Engineering Chemistry Research*, 43:5548–5561, 2004.

[40] P. Basu. *Combustion and Gasification in Fluidized Beds*. CRC Press, 2006.

[41] M. Leva and M. Grummer. A correlation of solids turnover in fluidized systems - its relation to heat transfer. *Chemical Engineering Progress*, 48:307–313, 1952.

[42] A.P. Baskakov, O.K. Vitt, V.A. Kirakosyan, V.K. Maskaev, and N.F. Filippovsky. Investigation of heat transfer coefficient pulsations and of the mechanism of heat transfer from a surface immersed into a fluidized bed. In *La Fluidisation et Ses ApplicationsCongress International*, volume 1, pages 1–5, 1973.

[43] M.G. Gronli. *A Theoretical and Experimental Study of the Thermal Degradation of Biomass*. PhD thesis, Norwegian University of Science and Technology, 1996.

[44] Martin Kaltschmitt, Hans Hartmann, and Hermann Hofbauer, editors. *Energie aus Biomasse. Grundlagen, Techniken und Verfahren*. Springer-Verlag Berlin Heidelberg, 3 edition, 2016.

[45] J. Rath and G. Staudinger. Cracking reactions of tar from pyrolysis of spruce wood. *Fuel*, 80:1379–1389, 2001.

[46] W. Klose and M. Wölki. On the intrinsic reaction rate of biomass char gasification with carbon dioxide and steam. *Fuel*, 84:885–892, 2005.

[47] M. Kuba, F. Havlik, F. Kirnbauer, and H. Hofbauer. Influence of bed material coatings on the water-gas-shift reaction and steam reforming of toluene as tar model compound of biomass gasification. *Biomass and Bioenergy*, in press, 2015.

[48] C. Di Blasi. Combustion and gasification rates of lignocellulosic chars. *Progress in Energy and Combustion Science*, 35:121–140, 2009.

[49] B. Peters and C. Bruch. Drying and pyrolysis of wood particles: experiments and simulation. *Journal of Analytical and Applied Pyrolysis*, 70:233–250, 2003.

[50] S. Gerber and M. Oevermann. A two dimensional Euler-Lagrangian model of wood gasification in a charcoal bed - Part I: model description and base scenario. *Fuel*, 115:385–400, 2014.

[51] H. Liu, R. J. Cattolica, R. Seiser, and C. Liao. Three-dimensional full-loop simulation of a dual fluidized-bed biomass gasifier. *Applied Energy*, 160:489–501, 2015.

[52] A. Anca-Couce and N. Zobel. Numerical analysis of a biomass pyrolysis particle model: Solution method optimized for the coupling to reactor models. *Fuel*, 97:80–88, 2012.

[53] Y. Haseli, J.A. van Oijen, and L.P.H. de Goey. A detailed one-dimensional model of combustion of a woody biomass particle. *Bioresour. Technol.*, 102(20):9772 – 9782, 2011.

[54] Y. Haseli, J.A. van Oijen, and L.P.H. de Goey. Numerical study of the conversion time of single pyrolyzing biomass particles at high heating conditions. *Chemical Engineering Journal*, 169:299 – 312, 2011.

[55] Y. Haseli, J.A. van Oijen, and L.P.H. de Goey. Modeling biomass particle pyrolysis with temperature-dependent heat of reactions. *J. Anal. Appl. Pyrolysis*, 90(2):140 – 154, 2011.

[56] S. Gerber, F. Behrendt, and M. Oevermann. An Eulerian modeling approach of wood gasification in a bubbling fluidized bed reactor using char as bed material. *Fuel*, 89:2903–2917, 2010.

[57] M. Sreekanth, D. Ruben Sudhakar, B.V.S.S.S. Prasad, Ajit Kumar Kolar, and B. Leckner. Modelling and experimental investigation of devolatilizing wood in a fluidized bed combustor. *Fuel*, 87(12):2698 – 2712, 2008.

[58] M. Oevermann, S. Gerber, and F. Behrendt. Euler-Lagrange/DEM simulation of wood gasification in a bubbling fluidized bed reactor. *Particuology*, 7:307–316, 2009.

[59] K.M. Bryden, K.W. Ragland, and C.J. Rutland. Modeling thermally thick pyrolysis of wood. *Biomass & Bioenergy*, 22:41–53, 2002.

[60] K.M. Bryden and M.J. Hagge. Modeling the combined impact of moisture and char shrinkage on the pyrolysis of a biomass particle. *Fuel*, 82:1633–1644, 2003.

[61] M.G. Gronli and M.C. Melaaen. Mathematical model for wood pyrolysiscomparison of experimental measurements with model predictions. *Energy & Fuels*, 14(4):791–800, 2000.

[62] A.M.C. Janse, R.W.J. Westerhout, and W. Prins. Modelling of flash pyrolysis of a single wood particle. *Chemical Engineering and Processing*, 39:239–252, 2000.

[63] E. Ranzi, A. Cuoci, T. Faravelli, A. Frassoldati, G. Migliavacca, S. Pierucci, and S. Sommariva. Chemical kinetics of biomass pyrolysis. *Energy & Fuels*, 22:4292–4300, 2008.

[64] J.C. Gibbings. *Dimensional Analysis*. Springer, 2011.

[65] L.R. Glicksman. Scaling relationships for fluidized beds. *Chemical Engineering Science*, 39:1373–1379, 1984.

[66] L.R. Glicksman, M. Hyre, and K. Woloshun. Simplified scaling relationships for fluidized beds. *Powder Technology*, 77:177–199, 1993.

[67] L. Reh. *Das Wirbeln von körnigem Gut im schlanken Diffusor als Grenzzustand zwischen Wirbelschicht und pneumatischer Förderung*. PhD thesis, University of Applied Sciences Karlsruhe, 1961.

[68] J.R. Grace. Contacting modes and behaviour classification of gas-solid and other two-phase suspensions. *The Canadian Journal of Chemical Engineering*, 64:353–363, 1986.

[69] M.A. van der Hoef, R. Beetstra, and J.A.M. Kuipers. Lattice-boltzmann simulations of low-reynolds-number flow past mono- and bidisperse arrays of spheres: results for the permeability and drag force. *Journal of Fluid Mechanics*, 528:233–254, 2005.

[70] B.G.M. can Wachem and A.E. Almstedt. Methods for multiphase computational fluid dynamics. *Chemical Engineering Journal*, 96:81–98, 2003.

[71] P.A. Cundall and O.D.L. Strack. A discrete numerical model for granular assemblies. *Géotechnique*, 29:47–65, 1979.

[72] N.G. Deen, M. van Sint Annaland, M.A. van der Hoef, and J.A.M. Kuipers. Reviewof discrete particle modeling of fluidized beds. *Chemical Engineering Science*, 62:28–44, 2007.

[73] T.B. Anderson and R. Jackson. A fluid mechanical description of fluidized beds. *Industrial & Engineering Chemistry Fundamentals*, 6:527–539, 1967.

[74] José Leboreiro Hernández. *Influence of drag laws on segregation and bubbling behavior in gas-fluidized beds*. PhD thesis, University of Colorado, 2008.

[75] B.H. Hjertager, T. Solberg, C.H. Ibsen, and K.G.Hansen. Multi-fluid CFD modelling of fluidized bed reactors. *International Journal of Chemical Reactor Engineering*, 2:Presentation P3, 2004.

[76] M.J. Andrews and P.J. O'Rourke. The Multiphase Particle-in-Cell (MP-PIC) method for dense particulate flows. *International Journal of Multiphase Flow*, 22:379–402, 1996.

[77] D.M. Snider. An incompressible three-dimensional multiphase particle-in-cell model for dense particle flows. *J. Comput. Phys.*, 170(2):523 – 549, 2001.

[78] D.M. Snider, S.M. Clark, and P.J. O'Rourke. Eulerian-Lagrangian method for three-dimensional thermal reacting flow with application to coal gasifiers. *Chemical Engineering Science*, 66:1285–1295, 2011.

[79] Peter J. O'Rourke and Dale M. Snider. A new blended acceleration model for the particle contact forces induced by an interstitial fluid in dense particle/fluid flows. *Powder Technology*, 256(0):39 – 51, 2014.

[80] R.P. Chabra, L. Agarwal, and N.K. Sinha. Drag on non-spherical particles: an evaluation of available methods. *Powder Technology*, 101:288–295, 1999.

[81] R. Turton and O. Levenspiel. A short note on the drag correlation for spheres. *Powder Technology*, 47:83–86, 1986.

[82] Dimitri Gidaspow. *Multiphase Flow and Fluidization*. Academic Press, 1 edition, 1994.

[83] A. Haider and O. Levenspiel. Drag coefficient and terminal velocity of spherical and nonspherical particles. *Powder Technology*, 58:63–70, 1989.

[84] P.N. Rowe and A.W. Nienow. Particle mixing and segregation in gas fluidised beds. a review. *Powder Technology*, 15:141–147, 1976.

[85] S. Chiba, A.W. Nienow, T. Chiba, and H. Kobayashi. Fluidised binary mixtures in which the denser component may be flotsam. *Powder Technology*, 26:1–10, 1980.

[86] R. Bilbao, J. Lezaun, and J.C. Abanades. Fluidization velocities of sand/straw binary mixtures. *Powder Technology*, 52:1–6, 1987.

[87] A. Di Renzo, F. P. Di Maio, R. Girimonte, and V. Vivacqua. Segregation direction reversal of gas-fluidized biomass/inert mixtures - Experiments based on particle segregation model predictions. *Chemical Engineering Journal*, 262:727–736, 2015.

[88] S. Chiba, T. Chiba, A.W. Nienow, and H. Kobayashi. The minimum fluidisation velocity, bed expansion and pressure-drop profiie of binary particle mixtures. *Powder Technology*, 22:255–269, 1979.

[89] M. Leva, M. Weintraub, M. Grummer, M. Pollchik, and H.H. Storch. *Fulid Flow through packed and fluidized systems*, volume 504, chapter Fluidization of Solids, pages 57–91. Bureau of Mines, 1951.

[90] B. Formisani, R. Girimonte, and T. Longo. The fluidization process of binary mixtures of solids: Development of the approach based on the fluidization velocity interval. *Powder Technology*, 185:97–108, 2008.

[91] W.-C. Yang and D.L. Keairns. Rate of particle separation in a gas fluidized bed. *Industrial & Engineering Chemistry Fundamentals*, 21:228–235, 1982.

[92] N.I. Gel'perin, V.G. Ainshtein, G.A. Nozov, V.V. Mamoshkina, and A.K. Rebrova. Some aspects of the fluidization of binary mixtures. *Teoreticheskie Osnovy Khimicheskoi Technology*, 1:383–391, 1967.

[93] J. L.-P. Chen and D.L. Keairns. Particle Segregation in a Fluidized bed. *The Canadian Journal of Chemical Engineering*, 53:395–402, 1975.

[94] B. Formisani, R. Girimonte, and V. Vivacqua. Extended validation of a model of segregating fluidization of homogeneous two-solid beds. *International Journal of Chemical Reactor Engineering*, 10:A41:1–A41:13, 2012.

[95] B. Formisani, R. Girimonte, and V. Vivacqua. Fluidization of mixtures of two solids: A unified model of the transition to the fluidized state. *AIChE Journal*, 59:729–735, 2013.

[96] M. Carsky, J. Pata, V. Vesely, and M. Hartman. Binary system fluidized bed equilibrium. *Powder Technology*, 51:237–242, 1987.

[97] G. Olivieri, A. Marzocchella, and P. Salatino. Segregation of fluidized binary mixtures of granular solids. *AIChE Journal*, 50:3095–3106, 2004.

[98] P. Pei, K. Zhang, B. Yu, J. Gao, G. Wu, and D. Wen. Dynamic characteristics of binary mixtures in a two-jet fluidized bed. *Chemical Engineering Science*, 66:1702–1714, 2011.

[99] Y. Zhang, B. S. Jin, and W. Q. Zhong. Fluidization characteristics of stalk-shaped biomass in binary particle system. In G. Yue, H. Zhang, C. Zhao, and Z. Luo, editors, *20th International Conference on Fluidized Bed Combustion*, 2009.

[100] F. Fotovat, J. Chaouki, and J. Bergthorson. The effect of biomass particles on the gas distribution and dilute phase characteristics of sand-biomass mixtures fluidized in the bubbling regime. *Chemical Engineering Science*, 102:129–138, 2013.

[101] B. Bai, S. Gheorghiu, J.R. van Ommen, J. Nijenhuis, and M.-O. Coppens. Characterization of the void size distribution in fluidized beds using statistics of pressure fluctuations. *Powder Technology*, 160:81–92, 2005.

[102] W.H. Park, W.K. Kang, C.E. Capes, and G.L. Osberg. The properties of bubbles in fluidized beds of conducting particles as measure by an elecroresistivity probe. *Chemical Engineering Science*, 24:851–865, 1969.

[103] R.D. Toomey and H.F. Johnstone. Gaseous fluidization of solid particles. *Chemical Engineering Progress*, 48:220–226, 1953.

[104] A.W. Nienow, P.N. Rowe, and L.Y.-L. Cheung. A quantitative analysis of the mixing of two segregating powders of different density in a gas-fluidised bed. *Powder Technology*, 20:89–97, 1978.

[105] Y. Zhang, B. Jin, and W. Zhong. Fluidization, mixing and segregation of a biomass-sand mixture in a fluidized bed. *International Journal of Chemical Reactor Engineering*, 6, 2008.

[106] Y. Zhang, B. Jin, and W. Zhong. Experimental investigation on mixing and segregation behavior of biomass particle in fluidized bed. *Chemical Engineering and Processing: Process Intensification*, 48:745–754, 2009.

[107] Y. Zhang, B. Jin, W. Zhong, B. Ren, and R. Xiao. Characterization of fluidization and segregation of biomass particles by combining image processing and pressure fluctuations analysis. *International Journal of Chemical Reactor Engineering*, 7, 2009.

[108] Y. Zhang, W. Zhong, and B. Jin. Experimental and theoretical study on fluidization of stalk-shaped biomass particle in a fluidized bed. *International Journal of Chemical Reactor Engineering*, 9:A54:1–A54:23, 2011.

[109] F. Fotovat, J. Shabanian, J. Chaouki, and J. Bergthorson. Characterization of fluidization and mixing of binary mixtures containing biomass at low velocities through analyzing. In *10th International Conference on Circulating Fluidized Beds and Fluidization Technology*, 2011.

[110] F. Fotovat, J. Chaouki, and J. Bergthorson. Distribution of large biomass particles in a sand-biomass fluidized bed: Experiments and modeling. *AIChE Journal*, 60:869–880, 2014.

[111] F. Fotovat, R. Ansart, M. Hemati, O. Simonin, and J. Chaouki. Sand-assisted fluidization of large cylindrical and spherical biomass particles: Experiments and simulation. *Chemical Engineering Science*, 126:543–559, 2015.

[112] J.M. Beeckmans, L. Bergström, and J.F. Large. Segregation mechanisms in gas fluidized beds. *The Chemical Engineering Journal*, 28:1–11, 1984.

[113] H.T. Bi. Acritical reviewof the complex pressure fluctuation phenomenon in gas-solids fluidized beds. *Chemical Engineering Science*, 62:3473–3493, 2007.

[114] H. Chen, D. Yang, and J. Cheng. Hydrodynamics of gas solids in a bubbling fluidized bed with binary particles. *Procedia Engineering, The 7th World Congress on Particle Technology (WCPT7)*, 102:799–803, 2015.

[115] D. Pallares and F. Johnsson. A novel technique for particle tracking in cold 2-dimensional fluidized beds – simulating fuel dispersion. *Chemical Engineering Science*, 61:2710–2720, 2006.

[116] H. Angelino, J.P. Couderc, R. Motyczynski, and M.N. Lacombe. Mélange des particules solides en couche fluidisée. *Chimie et Industrie - Géenie Chimique*, 102:1290–1299, 1969.

[117] J. M. Beeckmans, J. Nilsson, and J.-F. Large. Observations on the mechanisms of segregation in flotsam-rich, fully fluidized beds. *Industrial & Engineering Chemistry Fundamentals*, 24:90–95, 1985.

[118] T. Chiba, S. Chiba, and A.W. Nienow. Prediction of the steady state segregation pattern in gas fluidised beds with particles in throughflow. In *Fluidization V: Proceedings of the fifth Engineering Foundation Conference on Fluidization, Elsinore, Denmark*, 1986.

[119] M. Carsky, V. Vesely, and J. Pata. Particles segregation in fluidized bed binary systems. *Collection of Czechoslovak Chemical Communications*, 51, 1986.

[120] J.M Beeckmans and B. Stahl. Mixing and segragation kinetics in a strongly segregated gas-fluidized bed. *Powder Technology*, 53:31–38, 1987.

[121] M. Hemati, K. Spieker, C. Lagu'erie, R. Alvarez, and F.A. Riera. Experimental study of sawdust and coal particle mixing in sand or catalyst fluidized beds. *The Canadian Journal of Chemical Engineering*, 68:768, 1990. 772.

[122] Y.C. Seo, M.H. Ko, and Y. Kang. Axial mixing of resin beads in a gas-solid fluidized bed. *Korean Journal of Chemical Engineering*, 9:212–217, 1992.

[123] Y.H. Yu, J.H. Oh, J.Y. Lee, and H.W. Choi. Mixing characteristics of large cylindrical particles (RDF) in a gas-solid fluidized bed. *Journal of Industrial and Engineering Chemistry*, 9:798–803, 2003.

[124] M.C. Leaper, J.P.K. Seville, N. Hilal, S.W. Kingman, and A.S. Burbidge. Investigating the dynamics of segregation of high jetsam binary batch fluidised bed systems. *Chemical Engineering and Processing*, 43:187–192, 2004.

[125] Y. Shao, W. Zhong, and A. Yu. Mixing behavior of binary and multi-component mixtures of particles in waste fluidized beds. *Powder Technology*, page in press, 2016.

[126] L.-S. Fan, L.S. Han, and R.S. Brodkey. Comments on the buoyancy force on a particle in a fluidized suspension. *Chemical Engineering Science*, 42:1269–1271, 1987.

[127] G.G. Joseph, J. Leboreiro, C.M. Hrenya, and A.R. Stevens. Experimental segregation profiles in bubbling gas-fluidized beds. *AIChE Journal*, 53:2804–2813, 2007.

[128] R. Bilbao, J. Lezaun, M. Menéndez, and J.C. Abanades. Model of mixing-segregation for straw/sand mixtures in fluidized beds. *Powder Technology*, 56:149–155, 1988.

[129] M. Fang, L.Yang, G. Chen, Z. Shi, Z. Luo, and K. Cen. Experimental study on rice husk combustion in a circulating fluidized bed. *Fuel Processing Technology*, 85:1273–1282, 2004.

[130] S. Qiaoqun, L. Huilin, L. Wentie, H. Yurong, Y. Lidan, and D. Gidaspow. Simulation and experiment of segregating/mixing of rice husk-sand mixture in a bubbling fluidized bed. *Fuel*, 84:1739–1748, 2005.

[131] Z. Sun, J. Shen, B. Jin, and L. Wei. Combustion characteristics of cotton stalk in FBC. *Biomass and Bioenergy*, 34:761–770, 2010.

[132] L. Xiaodong, Y. Jianhua, N. Mingjiang, and C. Kefa. Study on mixing performance of municipal solid waste (MSW) in differential density fluidized beds (FBs). *Chemical Engineering Journal*, 84:161–166, 2001.

[133] B. Cluet, G. Mauviel, Y. Rogaume, O. Authier, and A. Delebarre. Segregation of wood particles in a bubbling fluidized bed. *Fuel Processing Technology*, 133:80–88, 2015.

[134] Q. Wang, H. Yang, P. Wang, J. Lu, Q. Liu, H. Zhang, L. Wei, and M. Zhang. Application of CPFD method in the simulation of a circulating fluidized bed with a loop seal part II - investigation of solids circulation. *Powder Technology*, 253:822–828, 2014.

[135] A.W. Nienow, P.N. Rowe, and T. Chiba. Mixing and segregation of a small proportion of large particles in gas fluidized beds of considerably smaller ones. *AIChE Symposium Series*, 74:45–53, 1978.

[136] A.W. Nienow and D.J. Cheesman. The effect of shape on the mixing and segregation of large particles in a gas-fluidised bed of small ones. In J.R. Grace and J.M. Matsen, editors, *Fluidization*, pages 373–380. Plenum Press, 1980.

[137] N.S. Naimer, T. Chiba, and A.W. Nienow. Parameter estimation for a solids mixing/segregation model for gas fluidised beds. *Chemical Engineering Science*, 37:1047–1057, 1982.

[138] A.C. Hoffmann, L.P.B.M. Janssen, and J. Prins. Particle segregation in fluisied binary mixtures. *Chemical Engineering Science*, 48:1583–1592, 1993.

[139] M. Mourad, M. Hemati, and C. Laguerie. Hydrodynamique d'un séchoir à lit fluidisé a flottation: Détermination des vitesses caractéristiques de fluidisation de mélanges de maïs et de sable. *Powder Technology*, 80:45–54, 1994.

[140] H. Park and H.S. Choi. The segregation characteristics of char in a fluidized bed with varying column shapes. *Powder Technology*, 246:561–571, 2013.

[141] Y. Shao, B. Ren, B. Jin, W. Zhong, H. Hu, X. Chen, and C. Sha. Experimental flow behaviors of irregular particles with silica sand in solid waste fluidized bed. *Powder Technology*, 234:67–75, 2013.

[142] N. Nakagawa, D. Bai, E. Shibuya, H. Kinoshita, T. Takarada, and K. Kato. Segregation of particles in binary solids circulating fluidized beds. *Journal of Chemical Engineering of Japan*, 27:194–198, 1994.

[143] M.T. Lim. *Hydrodynamics of a Cold Model of a Dual Fluidized Bed Gasification Plant*. PhD thesis, University of Canterbury, 2012.

[144] Y.A. Alghamdi, E. Doroodchi, and B. Moghtaderi. Mixing and segregation of binary oxygen carrier mixtures in a cold flow model of a chemical looping combustor. *Chemical Engineering Journal*, 223:772–784, 2013.

[145] A.R. Bidwe, C. Hawthorne, Y. Xizhi, H. Dieter, and G. Scheffknecht. Cold model study of a dual fluidized bed system for the gasification of solid fuels. *Fuel*, 127:151–160, 2014.

[146] S. Kraft, M. Kuba, F. Kirnbauer, K. Bosch, and H. Hofbauer. Optimization of a 50 MW bubbling fluidized bed biomass combustion chamber by means of computational particle fluid dynamics. *Biomass and Bioenergy*, Special issue of the 23rd European Biomass Conference and Exhibition held in Vienna, June 2015:31–39, 2016.

[147] J. Lim, K. Bae, J. Shin, J. Kim, D. Lee, J. Hand, and D Lee. Effect of particleparticle interaction on the bed pressure drop and bubble flow by computational particle-fluid dynamics simulation of bubbling fluidized beds with shroud nozzle. *Powder Technology*, 288:315–323, 2016.

[148] F. Fotovat, A. Abbasi, R. Spiteri, H. de Lasa, and J. Chaouki. A CPFD model for a bubbly biomass-sand fluidized bed. *Powder Technology*, 275:39–50, 2015.

[149] Y. Liang, Y. Zhang, T. Li, and C. Lu. A critical validation study on CPFD model in simulating gas-solid bubbling fluidized beds. *Powder Technology*, 263:121–134, 2014.

[150] J.M. Weber, K.J. Layfield, D.T. van Essendelft, and J.S.Mei. Fluid bed characterization using electrical capacitance volume tomography (ECVT), compared to CPFD software's Barracuda. *Powder Technology*, 250:138–146, 2013.

[151] L. Zhang, J. Wang, Q. Wang, H. Qin, and X. Xu. Simulation of oil shale semi-coke particle cold transportation in a spouted bed using CPFD method. *Powder Technology*, 301:360–368, 2016.

[152] C.B. Solnordal, V. Kenche, T.D. Hadley, Y. Feng, P.J. Witt, and K. Lim. Simulation of an internally circulating fluidized bed using a multiphase particle-in-cell method. *Powder Technology*, 274:123–134, 2015.

[153] X. Shi, R. Sun, X. Land, F. Liu Y. Zhang, and J. Gao. CPFD simulation of solids residence time and back-mixing in CFB risers. *Powder Technology*, 271:16–25, 2015.

[154] X. Shi, Y. Wu, X. Land, F. Liu, and J. Gao. Effects of the riser exit geometries on the hydrodynamics and solids back-mixing in CFB risers: 3D simulation using CPFD approach. *Powder Technology*, 284:130–142, 2015.

[155] S.S. Rodrigues, A. Forret, F. Montjovet, M. Lance, and T. Gauthier. CFD modeling of riser with group B particles. *Powder Technology*, 283:519–529, 2015.

[156] Q. Wang, T. Niemi, J. Peltola, S. Kallio, H. Yang, J. Lu, and L. Wei. Particle size distribution in CPFD modeling of gas-solid flowsin a CFB riser. *Particuology*, 21:107–117, 2015.

[157] X. Shi, X. Lan, F. Liu, Y. Zhang, and J. Gao. Effect of particle size distribution on hydrodynamics and solids back-mixing in CFB risers using CPFD simulation. *Powder Technology*, 266:135–143, 2014.

[158] C. Chen, J. Werther, S. Heinrich, H. Qi, and E. Hartge. CPFD simulation of circulating fluidized bed risers. *Powder Technology*, 235:238–247, 2013.

[159] G. Qiu, J. Ye, and H. Wang. Investigation of gas-solids flow characteristics in a circulating fluidized bed with annular combustion chamber by pressure measurements and CPFD simulation. *Chemical Engineering Science*, 134:433–447, 2015.

[160] S. Clark, D. Snider, and J. Spenik. CO2 Adsorption loop experiment with Eulerian-Lagrangian simulation. *Powder Technology*, 242:100–107, 2013.

[161] Q. Wang, H. Yang, P. Wang, J. Lu, Q. Liu, H. Zhang, L. Wei, and M. Zhang. Application of CPFD method in the simulation of a circulating fluidized bed with a loop seal, part I – Determination of modeling parameters. *Powder Technology*, 253:814–821, 2014.

[162] Q. Wang, W. Yin, B. Zhao, H. Yang, J. Lu, and L. Wei. The segregation behaviors of fine coal particles in a coal beneficiation fluidized bed. *Fuel Processing Technology*, 124:28–34, 2014.

[163] M.A. Hamilton, K.J. Whitty, and J.S. Lighty. Numerical simulation comparison of two reactor configurations for chemical looping combustion and chemical looping with oxygen uncoupling. *Journal of Energy Resources Technology*, 138, 2016.

[164] S. Clark. Particle-fluid flow simulation of an FCC regenerator. In *10th International Conference on Circulating Fluidized Beds and Fluidization Technology*, 2011.

[165] A. Kokourine and K. Adham. Three dimensional computational modeling of particulate solids segregation and elutriation in a commercial scale fluidized bed classifier. In *The 14th International Conference on Fluidization - From Fundamentals to Products*, 2013.

[166] M. Su, H. Zhao, and J. Ma. Computational fluid dynamics simulation for chemical looping combustion of coal in a dual circulation fluidized bed. *Energy Conversion and Management*, 105:1–12, 2015.

[167] S. Hu, W. Wang, R. Wessel, T. Flynn, and D. Kraft. Effect of in-bed heat exchanger on bed inventory imbalance in a pantleg CFB design a CFD study. In *11th International Conference on Fluidized Bed Technology*, 2014.

[168] P.J. Blaser and G. Corina. Validation and application of computational modeling to reduce erosion in a circulating fluidized bed boiler. *International Journal of Chemical Reactor Engineering*, 10:A51, 2012.

[169] M. Weng. Comparison between measurements and numerical simulation of particle flow and combustion a the CFBC plant Duisburg. In *10th International Conference on Circulating Fluidized Beds and Fluidization Technology - CFB-10*, 2011.

[170] M. Weng and A. Omer. CFBC fuel flexibility: Added value of advanced process optimization. *South African Journal of Chemical Engineering*, 19:48–61, 2014.

[171] R. K. Thapa, C. Pfeifer, and B. M. Halvorsen. Modeling of reaction kinetics in bubbling fluidized bed biomass gasification reactor. *International Journal of Energy and Environment*, 5:35–44, 2014.

[172] R.K. Thapa and B.M. Halvorsen. Heat transfer optimization in a fluidized bed biomass gasification reactor. *WIT Transactions on Engineering Sciences*, 83:169–178, 2014.

[173] C. Loha, H. Chattopadhyay, and P.K. Chatterjee. Three dimensional kinetic modeling of fluidized bed biomass gasification. *Chemical EngineeringScience*, 109:53–64, 2014.

[174] H. Liu, R.J. Cattolica, and R. Seiser. Operating parameter effects on the solids circulation rate in the cfd simulation of a dual fluidized-bed gasification system. *Chemical Engineering Science*, zin press, 2016.

[175] H. Liu, R.J. Cattolica, and R. Seiser. CFD studies on biomass gasification in a pilot-scale dual fluidized-bed system. *International Journal of Hydrogen Energy*, 41:11974–11989, 2016.

[176] L. de Diego, F. Garca-Labiano, A. Abad, P. Gayn, and J. Adnez. Modeling of the devolatilization of nonspherical wet pine wood particles in fluidized beds. *Industrial & Engineering Chemistry Research*, 41:3642–3650, 2002.

[177] Kenneth M. Bryden and Kenneth W. Ragland. Numerical modeling of a deep, fixed bed combustor. *Energy & Fuels*, 10(2):269–275, 1996.

[178] Michael L. Boroson, Jack B. Howard, John P. Longwell, and William A. Peters. Product yields and kinetics from the vapor phase cracking of wood pyrolysis tars. *AIChE J.*, 35(1):120–128, 1989.

[179] Wai-Chun R. Chan, Marcia Kelbon, and Barbara B. Krieger. Modelling and experimental verification of physical and chemical processes during pyrolysis of a large biomass particle. *Fuel*, 64(11):1505 – 1513, 1985.

[180] C. di Blasi. Modeling wood gasification in a countercurrent fixed-bed reactor. *Environmental and Energy Engineering*, 50:2306–2319, 2004.

[181] J. Macak and J. Malecha. Mathematical model for the gasification of coal under pressure. *Industrial & Engineering Chemistry Process Design and Development*, 17(1):92–98, 1978.

[182] R.A. Yetter and F.L. Dryer. Complications of one-step kinetics for moist co oxidation. In *Twenty-first Symposium (International) on Combustion*, 1986.

[183] G. Groppi, E. Tronconi, P. Forzatti, and M. Berg. Mathematical modelling of catalytic combustors fuelled by gasified biomasses. *Catal. Today*, 59:151 – 162, 2000.

[184] C.K. Westbrook and F.L. Dryer. Chemical kinetic modeling of hydrocarbon combustion. *Progress in Energy and Combustion Science*, 10:1–57, 1984.

[185] P. Kaushal, J. Abedi, and N. Mahinpey. A comprehensive mathematical model for biomass gasification in a bubbling fluidized bed reactor. *Fuel*, 89:3650–3661, 2010.

[186] Christian Wartha. *An Experimental Study on Fuel-nitrogen Conversion to NO and N2O and on Carbon Conversion under Fluidized Bed Conditions*. PhD thesis, Vienna University of Technology, 1998.

[187] S. Sazhin. Modelling of heating, evaporation and ignition of fuel droplets: combined analytical, asymptotic and numerical analysis. *Journal of Physics: Conference Series*, 22:174–193, 2005.

[188] T. Pröll. *Potenziale der Wirbelschichtdampfvergasung fester Biomasse - Modellierung und Simulation auf Basis der Betriebserfahrungen am Biomassekraftwerk Güssing*. PhD thesis, TU Wien, 2004.

[189] C. Jünger. *Grundlagenuntersuchungen zur Biomassetrocknung und Entwicklung eines Verfahrens zur Niedertemperaturtrocknung von Hackschnitzel*. PhD thesis, Institute of Chemical Engineering, Vienna University of Technology, 2008.

[190] *Prüfung von Holz. Bestimmung der Rohdichte*. DIN 52182, 1976.

[191] R. Mehrabian, R. Scharler, and I. Obernberger. Effects of pyrolysis conditions on the heating rate in biomass particles and applicability of TGA kinetic parameters in particle thermal conversion modelling. *Fuel*, 93:567–575, 2012.

[192] D. Bergström, S. Israelsson, M. Öhman, S. Dahlqvist, R. Gref, C. Boman, and I. Wästerlund. Effects of raw material particle size distribution on the characteristics of scots pine sawdust fuel pellets. *Fuel Processing Technology*, 89:1324–1329, 2008.

[193] P. Kaushal, T. Pröll, and H. Hofbauer. Model for biomass char combustion in the riser of a dual fluidized bed gasification unit: Part 1 - Model development and sensitivity analysis. *Fuel Processing Technology*, 89:651–659, 2008.

[194] F. Scala, R. Chirone, and P. Salatino. Combustion and attrition of biomass chars in a fluidized bed. *Energy & Fuels*, 20:91–102, 2006.

[195] F. Kirnbauer, M. Koch, R. Koch, C. Aichernig, and H. Hofbauer. Behavior of Inorganic Matter in a Dual Fluidized Steam Gasification Plant. *Energy & Fuels*, 27:3316–3331, 2013.

[196] J. Barata. Modelling of biofuel droplets dispersion and evaporation. *Renewable Energy*, 33:769–779, 2008.

[197] F. Berruti, J. Chaouki, L. Godfroy, T.S. Pugsley, and G.S. Patience. Hydrodynamics of circulating fluidized bed risers: A review. *The Canadian Journal of Chemical Engineering*, 73:579–602, 1995.

[198] T. Pröll, K. Rupanovits, P. Kolbitsch, J. Bolhar-Nordenkampf, and H. Hofbauer. Cold flow model study on a dual circulating fluidized bed system for chemical looping processes. *Chemical Engineering & Technology*, 32:418–424, 2009.

[199] W.-C. Yang, editor. *Handbook of Fluidization and Fluid-Particle Systems*. CRC Press, 2003.

[200] M. Zogg. *Einführung in die Mechanische Verfahrenstechnik*. B.G. Teuber, 3 edition, 1993.

[201] W. Peining, X.G. Wenchong, L. Qing, Y. Hairui, L. Junfu, Z. Yonggang, and Baiyang. Impact of passage structure on loop seal operating characteristic. In *11th International Conference on Fluidized Bed Technology*, 2011.